Cross-Flow Instability Control through Base-Flow Modification using AC-DBD Plasma Actuators

An Experimental Investigation

J.P.W. Arkesteijn

Technische Universiteit Delft

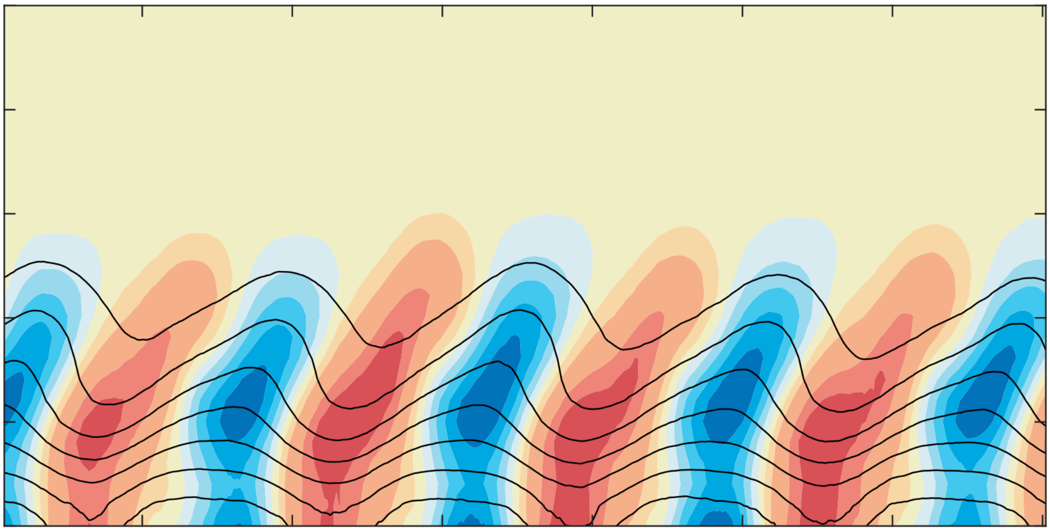

TU Delft Delft University of Technology

Challenge the future

Cross-Flow Instability Control through Base-Flow Modification using AC-DBD Plasma Actuators

An Experimental Investigation

by

J.P.W. Arkesteijn

to obtain the degree of Master of Science
at the Delft University of Technology,
to be defended publicly on Monday the 9th of August 2021.

Student number:	4371089	
Project duration:	November, 2020 – August, 2021	
Thesis committee:	Dr. M. Kotsonis,	TU Delft, Associate Professor
	Dr. F. Avallone,	TU Delft, Assistant Professor
	Dr. W. J. Baars,	TU Delft, Assistant Professor
	Ir. K. Peng,	TU Delft, PhD Candidate

An electronic version of this thesis is available at http://repository.tudelft.nl/.

TU Delft

Preface

This thesis is my final piece of work before my life as a student at the Delft University of Technology comes to an end. Even though some adaptation was required to work effectively in the midst of a global pandemic, I am glad to present the following thesis. Here, I would briefly like to express my gratitude to the people that helped me over the past nine months that I have been working on the topic of the cross-flow instability and AC-DBD plasma actuators.

First of all, I would like to thank Marios for his advice and guidance during my thesis. I highly appreciate the fact that Marios always made time in case I had any doubts and I thoroughly enjoyed having Marios as my supervisor. Special thanks to my daily supervisor Kaisheng, who was always available to help out with any questions I had, no matter how silly. I would also like to thank the other members and staff at the Low Speed Laboratory for their help with any other questions I had as well as with the experimental campaigns.

Over the past nine months I have learned a great amount, although there still remains a lot that is unknown to me. I can only assume that this is the cycle of research and hope to at least provide an answer to some of the questions with the presented work.

J.P.W. Arkesteijn,
Delft, August 2021

Abstract

With the aviation industry being one of the fastest growing sources of greenhouse gas emissions, there is an urgency for a more sustainable aviation sector. Delaying laminar-to-turbulent boundary layer transition could act as part of the solution, as laminar boundary layers induce lower levels of skin friction, consequently decreasing the fuel consumption and cost. Nevertheless, the limiting mechanism that is present on swept wings, which are prevalent on modern aircraft, is the cross-flow instability, which has proven to be difficult to control due to its significant receptivity to surface roughness and external disturbances. The cross-flow instability manifests itself as travelling waves and co-rotating vortices that are approximately aligned with the free-stream.

Although various flow control devices and techniques have shown to be able to limit the growth of the cross-flow instability, a flow control device that has seen a rise of interest over the past decades due to, amongst others, its operating range, its ability of directional control and its ease of manufacturing, is the AC-DBD plasma actuator. Following recent proof of laminar-to-turbulent transition delay using AC-DBD plasma actuators by directly reducing the cross-flow component, a flow control method known as base-flow modification (BFM), an experimental study is performed that focuses on investigating the physical mechanism that is responsible for this transition delay.

Initially, 2D2C-PIV is employed in order to characterise the performance of the AC-DBD plasma actuator in quiescent conditions. Following the electrical and mechanical characterisation of the various AC-DBD plasma actuator configurations, a wind tunnel experiment featuring a 45° swept wing, which was purposefully designed for receptivity and cross-flow studies, is performed in the anechoic wind tunnel (A-tunnel) at the Delft University of Technology. Stereoscopiv PIV is employed in order to extract the influence of the actuator on the boundary layer velocity components. It is found that the AC-DBD plasma actuator is capable of directly decreasing the cross-flow component for a variety of operating conditions. Decreasing the Reynolds number results in a larger decrease of the cross-flow component, highlighting the robustness of the base-flow modification flow control technique with respect to techniques that aim to induce specific stationary modes or influence the cross-flow vortices.

A second wind tunnel experiment is performed to assess the influence of the AC-DBD plasma actuator on the growth and development of the primary cross-flow instability. Discrete roughness elements (DRE) of various heights are placed near the leading edge to force the several instability modes in order to ensure steady experimental conditions. 2D2C-PIV is employed and consecutive span-wise planes are recorded in the stream-wise direction to monitor the growth and location of the stationary cross-flow vortices. Additionally, infrared thermography is used to qualitatively assess whether transition occurs. In case the AC-DBD plasma actuator is operated at lower carrier frequencies (up to 4 kHz), turbulent wedges are observed. These seem to be a direct consequence of strong localised plasma arcs as a result of the unsteady behaviour of the actuator at these lower frequencies. Additionally, it is believed the aging of the actuator plays a significant role here. Nevertheless, when the actuator is operated at a frequency of 5 kHz and various voltages, the cross-flow vortices shift away from the actuator location and a slight reduction in the cross-flow vortex amplitude is found at each chord location. A similar result is obtained for the configuration featuring three consecutive actuators, although operating these at a high applied voltage results in early transition due to the induced traveling waves and blockage effect.

It is shown that the cross-flow component can be directly reduced through base-flow modification using AC-DBD plasma actuators. As a result, the cross-flow vortices shift location accordingly and feature lower amplitudes, indicating the potential for a cross-flow induced transition delay. Nevertheless, it is found that the success of base-flow modification using AC-DBD plasma actuators highly depends on the chosen carrier frequency and voltage, as well as the actuator lifetime and configuration.

Contents

Preface iii

Abstract v

List of Figures ix

List of Tables xv

List of Symbols and Abbreviations xvii

1 Introduction 1

2 State of the Art 3
- 2.1 Boundary Layer Fundamentals . . . 3
- 2.2 Swept Wing Instability Mechanisms . . . 6
- 2.3 Cross-flow Instability . . . 6
  - 2.3.1 Receptivity of Three-Dimensional Boundary Layers . . . 8
  - 2.3.2 Primary and Secondary Cross-flow Instabilities . . . 10
- 2.4 Control of the Cross-flow Instability . . . 14
  - 2.4.1 Discrete Roughness Elements . . . 14
  - 2.4.2 Suction and Blowing Systems . . . 15
- 2.5 AC-DBD Plasma Actuators . . . 17
  - 2.5.1 Working Principle of AC-DBD Plasma Actuators . . . 18
  - 2.5.2 Flow Control by AC-DBD Plasma Actuators . . . 19
- 2.6 Research Objective . . . 22

3 Methodology 25
- 3.1 Linear Stability Theory . . . 25
- 3.2 Particle Image Velocimetry . . . 27
  - 3.2.1 Working Principle . . . 27
  - 3.2.2 Stereo Particle Image Velocimetry . . . 28
  - 3.2.3 Uncertainty Quantification & Error Propagation . . . 29
- 3.3 Data Analysis Techniques . . . 30
  - 3.3.1 Electrical Characterisation . . . 31
  - 3.3.2 Mechanical Characterisation . . . 31
  - 3.3.3 Cross-Flow Instability Metrics . . . 34
  - 3.3.4 Power Spectral Density . . . 34

4 Experimental Setup 37
- 4.1 Plasma Actuator Design . . . 37
- 4.2 Electrical Characterisation . . . 38
- 4.3 Mechanical Characterisation . . . 39
- 4.4 Base-Flow Modification Wind Tunnel Experiment . . . 40
  - 4.4.1 Wind Tunnel Facility and Wing Model . . . 41
  - 4.4.2 Experimental Set-up . . . 41
  - 4.4.3 Test Matrix . . . 43
- 4.5 Cross-Flow Instability Wind Tunnel Experiment . . . 44
  - 4.5.1 Linear Stability Analysis . . . 44
  - 4.5.2 Experimental Setup . . . 46
  - 4.5.3 Test Matrix . . . 47

5 Results **49**
- 5.1 Electrical Characterisation Results . . . 49
- 5.2 Mechanical Characterisation Results . . . 51
  - 5.2.1 Raw Data Processing & Uncertainty Quantification . . . 51
  - 5.2.2 Induced Velocity Field . . . 51
  - 5.2.3 AC-DBD Plasma Actuator Thrust and Body Force . . . 55
  - 5.2.4 Spectral Analysis . . . 58
- 5.3 Base-Flow Wind Tunnel Experiment Results . . . 60
  - 5.3.1 Raw Data Processing & Uncertainty Quantification. . . . 60
  - 5.3.2 Results . . . 61
- 5.4 Cross-Flow Instability Wind Tunnel Experiment Results . . . 68
  - 5.4.1 Infra-red Thermography . . . 68
  - 5.4.2 Planar PIV . . . 71

6 Conclusion & Recommendations **85**

Bibliography **89**

List of Figures

2.1 Schematic representation of the evolution of a boundary layer over a flat plate. As from Michelis [53]. 4

2.2 Boundary layer separation. The wall-normal velocity distribution features an inflection ($\partial u/\partial y = 0$) and the streamlines move away from the surface. Boundary layer thickness indicated by δ. As from Michelis [53]. 4

2.3 Paths towards breakdown and turbulence, as adapted from Morkovin et al. [55] 5

2.4 Illustration of a swept wing boundary layer featuring the cross-flow component. The cross-flow component is not to scale; in reality its amplitude and vertical extent is a small percentage of the stream-wise component. As from White & Saric [93]. 7

2.5 Swept wing covered in fluorescent oil, showing the trace of the cross-flow vortices and the jagged transition front. The flow is coming from the right. As from Serpieri [80]. 7

2.6 Spatial growth rates and saturation amplitude for the stationary CFVs ($\overline{u}_s$) and travelling waves (u_{rms}) for wind tunnels featuring a turbulence level of 0.15% (a) and 0.08% (b). As from Deyhle & Bippes [12]. 8

2.7 Power spectra obtained from hot-wire measurements taken at x/c = 0.45, Re_c = 2.4 $\cdot 10^6$ and y = 0.9 mm. DREs are located at x/c = 0.023 with a spacing of 12 mm (a) and 36 mm (b). As from Reibert et al. [64]. 10

2.8 Time-averaged velocity (black lines) and velocity fluctuations (grey scale) for various frequency bands pertaining to the type-III instability (left), the type-I mode (middle) and the type-II mode (right). As from Serpieri & Kotsonis [82]. 11

2.9 λ_2-Isosurfaces showing a cross-flow-vortex-mode packet and the convective nature of the secondary instability once background pulses are turned off. As from Wassermann & Kloker [90]. 13

2.10 Wall-normal plane showing the instantaneous velocity (black lines) and real parts of the Fourier amplitude (contour) for a high-frequency mode of 3622 Hz, taken at x/c = 0.4, for the natural case (a) and sub-critical case (b). As in Hosseini et al. [29]. 15

2.11 Stream-wise velocity fluctuation contours for the case of no control (a) and sub-critically forced suction (b). The reduction in stream-wise velocity fluctuations is clearly visible. As from Lohse et al. [46]. 15

2.12 Schematic representation of the pinpoint suction set-up for a cross-flow vortex. The solid lines represent the streamline-oriented velocity component, whereas the dashed lines correspond to λ_2-isocontours. The high-frequency secondary instability is visualised by grey scale and the arrows indicate the suction distribution along the hole. As from Friederich & Kloker [22]. 16

2.13 Span-wise averaged mean flow profiles of the stream-wise (left) and span-wise (right) velocity component along a streamline with and without suction. As from Bippes [8]. . . . 17

2.14 Illustration of a typical AC-DBD plasma actuator configuration. As from Erfani et al. [20]. 18

2.15 AC input and corresponding discharge currents (left) with the corresponding intensified Charged-Coupled Device (iCCD) camera images for each section of the cycle, clearly showing a strong asymmetry. As from Benard & Moreau [67]. 18

2.16 Experimental set-up where the CFVs pass over the plasma jets (a) and in between the plasma jets (b). Furthermore, the discrete roughness elements, the DBD actuator with its exposed electrode (grey) and encapsulated electrode (orange) and three inviscid streamlines are shown. As from Yadala et al. [96]. 20

2.17 Experimental set-up of forcing against the cross-flow (a) and in the direction of the cross-flow (b). The discrete roughness elements (black dots), the exposed electrode (grey bar) and an inviscid streamline (thin line) along with the local streamwise and spanwise velocity components are also visualised. As from Yadala et al. [95]. 21

3.1 An example of a planar PIV arrangement for a wind tunnel experiment, as presented by Raffel et al. [62]. . . . 27
3.2 Example of an optical arrangement for stereoscopic PIV, showing the necessity of the Scheimpflug mount in order to ensure a fully focused image. As from Liu et al. [45]. . . 29
3.3 Lissajous curve, clearly showing the high-frequency discharges in the lower-right quadrant, which corresponds to the positive half-cycle of the respective input signal. As from Pons et al. [59]. . . . 32
3.4 Example of a time-averaged velocity field induced by an AC-DBD plasma actuator. The control volume used for the thrust calculation is shown by the dashed line. As from Kotsonis et al. [40]. . . . 33

4.1 Printer that is used to print the silver electrodes on the designated sheets, with an example sheet visible featuring the ground electrode on top of the printer (a) and an example of a complete AC-DBD plasma actuator sheet featuring three consecutive electrode pairs (b). Two paths exit the page on the right, with the high-voltage connection being the upper electrode and the ground connection being the lower electrode. The purple arrow indicates the direction in which the plasma is formed. . . . 38
4.2 Sketch of three consecutive actuators and their method of operation; the flow is continuously accelerated over the electrodes. . . . 39
4.3 Experimental set-up for the mechanical characterisation experiment, as conducted in a Plexiglas box. . . . 39
4.4 Airfoil of the wing used throughout this research (red) and the M3J (black). . . . 41
4.5 (a) Schematic of the test set-up and (b) sketch of the wing leading-edge region, as seen when rotated clock-wise by 90° (not to scale). Although not used in this experiment, DREs (•) are included in relation to the subsequent wind tunnel experiment. . . . 42
4.6 Close-up of the experimental set-up for investigating the effect of the AC-DBD plasma actuator on the base flow near the leading edge of the wing. . . . 43
4.7 Close-up of the wing leading edge, featuring the silver electrodes that make up the plasma actuator and the discrete roughness elements spaced 8 mm apart. . . . 44
4.8 Pressure coefficient distribution for the wing used in the wind tunnel experiments in comparison to the M3J wing. The upper and lower C_p values are obtained from the outboard and inboard pressure taps respectively. . . . 45
4.9 (a) N-factor as a function of the wavelength for a frequency of 0 Hz and (b) N-factor as a function of the considered frequency for a wavelength of λ = 8 mm. . . . 45
4.10 N-factor as a function of the wavelength λ and the stream-wise chord location for various frequencies (0, 200, 400 and 600 Hz). . . . 46
4.11 Experimental set-up for investigating the effect of the AC-DBD actuator on the cross-flow instability (a) and a corresponding schematic indicating the position of the various instruments (b). . . . 47

5.1 (a) Lissajous diagram showing 10000 cycles, equal to a measurement time of 0.1 seconds, for the case of 3 consecutive actuators with a spacing of 5 mm (12 kV_{pp}, 5 kHz) and (b) the effect of the number of consecutive actuators on the average power consumption. 49
5.2 (a) Effect of the spacing between three consecutive actuators operated at 5 kHz on the average power consumption and (b) the effect of the dielectric thickness on the average power consumption for the case of 3 consecutive actuators with a 5 mm spacing operated at 5 kHz. . . . 50
5.3 Time-averaged uncertainty field of the u velocity component (left) and the v velocity component (right), obtained from 9701 double-frame images for a single actuator (15 kV_{pp}, 5 kHz). The vectors indicate the direction and magnitude of the total velocity U. . 51
5.4 Time-averaged velocity field of the u velocity component (left) and the v velocity component (right) obtained from 9701 double-frame images for a single actuator (14 kV_{pp}, 5 kHz). The vectors indicate the direction and magnitude of the total velocity U. . . . 52
5.5 Mean (left) and standard deviation (right) of the total velocity field (U) of 9701 double-frame images for a single actuator (14 kV_{pp}, 5 kHz). The vectors indicate the direction and magnitude of the total velocity U. . . . 52

5.6 Time-averaged total velocity field U of 9701 double-frame images for a single actuator operated at 15 kV_{pp} and 1 kHz (top left), 15 kV_{pp} and 2 kHz (top right), 13 kV_{pp} and 5 kHz (bottom left) and 14 kV_{pp} and 5 kHz (bottom right). 52
5.7 Time-averaged total velocity field U of 19403 single-frame images for three consecutive actuators operated at an applied voltage of 12 kV and a carrier frequency of 5 kHz. . . 53
5.8 (a) The influence of the spacing between three consecutive actuators in series, operated at 12 kV_{pp} and 5 kHz and (b) The influence of the applied voltage on the induced velocity for the configuration featuring three actuators in series with a spacing of 5 mm, operated at a carrier frequency of 5 kHz. Curves shown for y = 0.73 mm. 54
5.9 Time-averaged vorticity field (ω) of 19403 single-frame images for three actuators in series with various spacings, operated at an applied voltage of 12 kV and a carrier frequency of 5 kHz. 55
5.10 Time-averaged total velocity field (U) for a single actuator operated at an applied voltage of 14 kV and a carrier frequency of 5 kHz. The control volume (dotted line) ranges from approximately x = -8 mm to 1.5 mm and from y = 0 mm to 2 mm. 56
5.11 Spatial distribution of the body force calculated according to the gradient method for a single actuator operated at 15 kV_{pp} and 1 kHz (top-left) and 2 kHz (top-right) as well as at 13 kV_{pp} (bottom-left) and 14 kV_{pp} (bottom-right) and 5 kHz. 57
5.12 Computed thrust and body force according to the momentum balance method and gradient method respectively, for a single actuator operated at various applied voltages (5 kHz) (a) and carrier frequencies (15 kV_{pp}) (b). 57
5.13 PSD of u' at (-3, 0.3) for a single AC-DBD plasma actuator operating at an applied voltage of 15 kV_{pp} and a carrier frequency of 1 kHz (a) and 2 kHz (b). 58
5.14 PSD of u' at (-3, 0.3) for a single AC-DBD plasma actuator operating at an applied voltage of 15 kV_{pp} and a carrier frequency of 3 kHz (a) and a corresponding PSD contour for y = 0.3 mm (b). 59
5.15 Contours of the PSD of u' at y = 0.3 mm for a single AC-DBD plasma actuator operating at an applied voltage of 15 kV_{pp} and a carrier frequency of 1 kHz (a) and 2 kHz (b). . . 59
5.16 Bottom section of a minimum intensity image. The background is black and the reflections at the wall are white. Identified intensities beyond a threshold value are shown as dots in green (top) and the resulting wall polynomial is shown as a green line (bottom). 61
5.17 Example of a velocity field obtained from DaVis 10.1 (blue colorscale) featuring the approximated wall location (green line) and the introduced wall-normal and -parallel grid (+). 61
5.18 Mean total velocity U_s contours displaying the difference between the respective carrier frequency (15 kV_{pp}) and the clean configuration. Visualised on the curvilinear (ξ, η) grid. 62
5.19 Tangential velocity component u_s (left) and perpendicular velocity component w_s (right) contours displaying the difference between the respective carrier frequency (5 kHz) and the clean configuration. Visualised on the curvilinear (ξ, η) grid. 63
5.20 u_s (a) and w_s (b) velocity profiles along an inviscid streamline at x = -2.5 as a function of the carrier frequency (15 kV_{pp}). 63
5.21 Difference with respect to the clean configuration of u_s (a) and w_s (b) along an inviscid streamline at x = -2.5 as a function of the carrier frequency (15 kV_{pp}). 64
5.22 Difference with respect to the clean configuration of u_s (a) and w_s (b) along an inviscid streamline at x = -5.0 as a function of the carrier frequency (15 kV_{pp}). 64
5.23 Difference with respect to the clean configuration of u_s (a) and w_s (b) along an inviscid streamline at x = -10.0 as a function of the carrier frequency (15 kV_{pp}). 65
5.24 u_s (a) and w_s (b) velocity profiles along an inviscid streamline at x = -2.5 as a function of the applied voltage (5 kHz). 65
5.25 Difference with respect to the clean configuration of u_s (a) and w_s (b) along an inviscid streamline at x = -2.5 as a function of the applied voltage (5 kHz). 66
5.26 Tangential velocity component u_s (left) and perpendicular velocity component w_s (right) contours displaying the difference between the respective carrier frequency (5 kHz) and the clean configuration. Visualised on the curvilinear (ξ, η) grid. 66
5.27 u_s (a) and w_s (b) velocity profiles along an inviscid streamline at x = -2.5 as a function of the applied voltage (5 kHz, Re $\approx$ 5.52 $\cdot 10^5$). 67

5.28 Difference with respect to the clean configuration of u_s (a) and w_s (b) along an inviscid streamline at x = -2.5 as a function of the applied voltage (5 kHz, Re ≈ 5.52 $\cdot 10^5$). . . . 67

5.29 Infra-red image of the clean configuration (plasma inactive), clearly showing the stationary cross-flow vortices as a result of the forcing of the 8 mm mode by the 200 μm tall DREs. Temperature ranging from 24.5°C (black) to 29°C (white). 68

5.30 Infra-red images corresponding to various AC-DBD plasma actuator carrier frequencies (15 kV_{pp}), obtained by subtracting the clean configuration. Temperature ranging from 0°C (black) to 5°C (white). 69

5.31 Instantaneous infra-red image including the location of the maximum temperature (left, 15 kV_{pp}) and the instantaneous temperature field in the case of three electrode pairs (right, 5 kHz). Temperature ranging from 25°C (black) to 33°C (white). 70

5.32 Infra-red images corresponding to various AC-DBD plasma actuator applied voltages (5 kHz), obtained by subtracting the clean configuration. Temperature ranging from 0°C (black) to 5°C (white). 71

5.33 Uncertainty field for the clean configuration (8 mm spacing, L2 DRE) at a chord location of X/c_X = 0.20, of which the values are representative for the complete experiment. . . 72

5.34 Mean total velocity U contours for the clean configuration (plasma inactive, DRE spacing 8 mm, 200 μm tall) at various chord locations. The velocity fields are presented from downstream. 73

5.35 Dominant wavelengths as obtained from a domain spanning three cross-flow vortices at a chord location of x/c = 0.35 for the clean configuration, where the PSD is calculated by FFT(w_{rms}^2). Each line corresponds to a single y-location. 73

5.36 Mean span-wise standard deviation w_{rms} contours for the clean configuration (plasma inactive, DRE spacing 8 mm, 200 μm tall) at various chord locations. The velocity fields are presented from downstream. 74

5.37 Span-wise averaged velocity w_{mean} (a) and standard deviation w_{rms} (b), non-dimensionalised with the local external velocity U_e for several chord locations (plasma inactive). 74

5.38 Non-dimensional amplitudes computed from the maximum metric (a) and the integral metric (b) for both the w velocity component (upper values) and the v velocity component (lower values). 75

5.39 Span-wise averaged velocity w_{mean} (a) and standard deviation w_{rms} (b), non-dimensionalised with the local external velocity U_e for several chord locations (14 kV_{pp}, 5 kHz). 76

5.40 Total velocity U contours normalised with the mean local external velocity U_e (14 kV_{pp}, 5 kHz). The clean configuration is subtracted to show the difference. The mean velocity is visualised by the black iso-lines (5 levels from 0 to 1). The contours are presented from downstream. 77

5.41 Total velocity U contours normalised with the mean local external velocity U_e (14 kV_{pp}, 5 kHz). The clean configuration is subtracted to show the difference. The mean velocity is visualised by the black iso-lines (5 levels from 0 to 1). The presented colorbar is associated with the clean configuration; the colorbar relevant to the other flow fields features the same colours and instead ranges from -1.0 to +1.0. 78

5.42 Non-dimensional amplitudes computed from the integral metric for both the w (upper values) and the v velocity component (lower values) as a function of the carrier frequency (a) and the applied voltage (b), including the clean configuration at x/c = 0.15 (–) and x/c = 0.275 (- -). 78

5.43 Span-wise averaged standard deviation w_{rms} for various carrier frequencies (15 kV_{pp}) (a) and voltages (5 kHz) (b) normalised with the local external velocity U_e for a chord location of x/c = 0.275. 79

5.44 Mean total velocity U contours for the clean configuration (plasma inactive, DRE spacing 8 mm, 100 μm tall) at various chord locations. The velocity fields are presented from downstream. 80

5.45 Span-wise averaged velocity w_{mean} (a) and standard deviation w_{rms} (b) normalised with the local external velocity U_e for several chord locations in case of the clean configuration. 80

5.46 Mean total velocity U contours for the clean configuration (plasma inactive, DRE spacing 8 mm, 200 μm tall) at various chord locations. The velocity fields are presented from downstream. 81

5.47 Total velocity U contours normalised with the mean local external velocity U_e (12 kV_{pp}, 5 kHz). The clean configuration is subtracted to show the difference. The mean velocity is visualised by the black iso-lines (5 levels from 0 to 1). The contours are presented from downstream. 82
5.48 Mean span-wise standard deviation w_{rms} contours in the case of plasma active (3 actuators, 12 kV_{pp}, 5 kHz) at various chord locations. The velocity fields are presented from downstream. 82
5.49 Span-wise averaged standard deviation w_{rms} for the clean configuration (a) and for the case where the three AC-DBD plasma actuators are active (12 kV_{pp}, 5 kHz), non-dimensionalised with the local external velocity U_e for several chord locations. 83

List of Tables

4.1 AC-DBD plasma actuator configuration for the electrical characterisation experiment. . . . 37
4.2 Camera settings for the AC-DBD plasma actuator mechanical characterisation PIV experiment. 40
4.3 Test matrix for the AC-DBD plasma actuator mechanical characterisation PIV experiment. 40
4.4 Optical settings for the wind tunnel experiment focused on the influence of the plasma actuator on the base flow. 43
4.5 Test matrix for the base-flow wind tunnel experiment. 44
4.6 Camera settings for the wind tunnel experiment concerning the effect of the AC-DBD plasma actuator on the cross-flow instability. 47
4.7 DRE configurations for the cross-flow instability wind tunnel experiment. 48
4.8 Test matrix for the cross-flow instability wind tunnel experiment. 48

List of Symbols and Abbreviations

Greek Letters

α	Stream-wise wavenumber or angle of attack
β	Span-wise wavenumber
δ	Boundary layer thickness
λ	Fundamental span-wise wavelength
μ	Dynamic viscosity
ν	Kinematic viscosity
ω	Frequency or vorticity
ψ	Stream function
ρ	Density
τ	Wall shear stress

Latin Letters

A	Amplitude
C	Capacitance
c	Chord
c_p	Pressure coefficient
F	Force
f	Frequency
I	Current
k	Total wavenumber magnitude
M	Mach Number
N	Amplification Factor
P	Power
p	Pressure
Q	Charge
Re	Reynolds Number
T	Turbulence level
t	Time
T_x	Thrust in the x-direction

T_y	Thrust in the y-direction
Tu	Turbulence intensity
U	Total velocity magnitude
U	Uncertainty
U, V, W	Velocity components in wind tunnel coordinate system
u, v, w	Velocity components in swept-wing coordinate system
u_s, v_s, w_s	Velocity components along inviscid streamline
V	Voltage
X, Y, Z	Axes in wind tunnel coordinate system
x, y, z	Axes in swept-wing coordinate system
x_s, y_s, z_s	Axes in inviscid streamline coordinate system

Abbreviations

2D	Two-dimensional
3D	Three-dimensional
AC	Alternating Current
ASU	Arizona State University
BFM	Base-Flow Modification
CFI	Cross-Flow Instability
CFV	Cross-Flow Vortex
DBD	Dielectric Barrier Discharge
DC	Direct Current
DLR	Deutsches Zentrum für Luft- und Raumfahrt
DNS	Direct Numerical Simulation
DRE	Discrete Roughness Elements
EMI	Electromagnetic Interference
FFT	Fast Fourier Transform
FOV	Field of view
FSD	Free-Stream Disturbances
IR	Infrared
KSWT	Klebanoff-Saric Wind Tunnel
L1	Single layer of DREs
L2	Double layer of DREs
LDV	Laser Doppler Velocimetry

LES	Large-Eddy Simulation
LFC	Laminar Flow Control
LST	Linear Stability Theory
LTT	Low Turbulence Tunnel
MEMS	Micro-Electrical Mechanical System
NPSE	Non-Linear Parabolised Stability Equations
PET(-G)	Polyethylene terephthalate (glycol)
PIV	Particle Image Velocimetry
POD	Proper Orthogonal Decomposition
PSD	Power Spectral Density
PTU	Programmable Timing Unit
RMS	Root Mean Square
SSA	Segmented Swept Actuator
TS	Tollmien-Schlichting
UFD	Upstream Flow Deformation

1

Introduction

As air traffic is predicted to grow steadily in the next decades and sustainability attains an ever increasing importance in today's society [2], the pressure is on the scientific community and the commercial sector to find solutions as to how to decrease the impact of aviation on the environment. A research topic that has been of particular interest is that of boundary layer transition, as a delay in transition yields a reduction in skin friction drag and consequently fuel consumption and cost.

In order to reduce the excessive drag rise that occurs when shock waves form over the wing beyond a threshold Mach number, modern aircraft feature swept wing geometries. Although these swept wings yield a great advantage in flight, they introduce several complications and modify the most dominant boundary layer transition mechanism. Whereas in non-swept scenarios Tollmien-Schlichting waves are responsible for the transition process, in swept wing flows the cross-flow instability (CFI) is the main contributor. The additional cross-flow component, which would otherwise not be present in an unswept scenario, ultimately leads to an inflection point in the velocity profile, known as the cross-flow instability. The instability displays itself in the form of unsteady travelling waves as well as stationary co-rotating vortices with their axes in the direction of the flow. The vortices strongly modify the boundary layer and its velocity distribution. Once the vortices reach their saturation amplitude, secondary instabilities arise and their explosive growth leads to the initiation of laminar-to-turbulent transition and ultimately flow breakdown.

Over the years a significant amount of research has been conducted on the mechanisms and intricacies of cross-flow induced transition as well as how the cross-flow instability can potentially be controlled or suppressed. These methods related to delaying laminar-to-turbulent transition are often described as laminar flow control (LFC) techniques, which can be categorised as either active or passive depending on their method of operation.

One type of laminar flow control that has the potential to delay laminar-to-turbulent transition is that of micron-sized discrete roughness elements (DRE), as presented by Saric et al. [70]. When the elements are placed near the leading-edge and are uniformly spaced with a distance that is smaller than the most unstable wavelength associated with the cross-flow vortices, the growth of this unstable mode is suppressed and the formation of secondary instabilities is postponed, resulting in a delay in boundary layer transition, as shown by Saric & Reed [69]. It must be noted that this working principle differs from other conventional cross-flow laminar flow control techniques, which aim to reduce the mean cross-flow velocity and are known as base-flow modification (BFM) techniques. A drawback of this method of upstream flow deformation (UFD), which covers all the flow control techniques that aim to excite beneficial cross-flow vortex modes, is that the elements have a fixed height and spacing and are therefore optimised for only one operating condition. In an effort to extend the operating range, the ideology of DRE and BFM has been expanded to alternating current (AC) dielectric barrier discharge (DBD) plasma actuators [16].

AC-DBD plasma actuators offer several benefits over previously mentioned flow control concepts. First of all, the frequency and amplitude of the supplied voltage signal can be adjusted to allow for a dynamic range of forcing frequencies and amplitudes. The actuators can be manufactured and positioned as to exert flow control in a designated direction and do not feature any moving parts, simplifying their operation and maintenance. Furthermore, the manufacturing process and application of AC-DBD plasma actuators allows for minimal interference with the cross-flow instability, which is very sensitive to surface roughness.

The actuators can be designed and configured with the objective to, amongst others, modify the base-flow or act as discrete roughness elements. Studies by Yadala et al. [95, 96] have shown that cross-flow instability control through base-flow modification using AC-DBD plasma actuators is a valid flow control technique, as a delay in laminar-to-turbulent transition for a swept wing was observed for various Reynolds numbers in an experimental framework. On the other hand, Serpieri et al. [84] successfully conditioned stationary cross-flow vortices at selected wavelengths using novel AC-DBD plasma actuators. Although plasma actuators based on the DRE approach require less energy in their actuation, as discussed by Dörr & Kloker [18], their method of operation is, similarly to DREs, extremely sensitive to free-stream disturbances and surface roughness, as shown by Deyhle & Bippes [12]. Furthermore, as the Reynolds number increases, the most unstable wavelength decreases, indicating a potential issue with respect to actuator size and operating frequency, as discussed by Yadala et al. [95]. In contrast, AC-DBD plasma actuators employed to weaken the cross-flow component through base-flow modification are much less sensitive to changes in the flow condition, as the span-wise uniform actuator is not dependent on the critical wavelength, making them a more robust option despite the larger energy requirement.

Following the success of Yadala et al. [95] regarding the delay in laminar-to-turbulent transition through base-flow modification using AC-DBD plasma actuators, this research is aimed at investigating the influence of the operation of the AC-DBD plasma actuator, based on base-flow modification, on the cross-flow instability in a three-dimensional boundary layer over a swept wing. Initially, the reader is introduced to the physical mechanisms of the cross-flow instability as well as various state-of-the-art flow control techniques. The research objective is then established, after which a study is performed to characterise the plasma actuator and its unsteady characteristics during operation. Succeedingly, the effect of the AC-DBD plasma actuator on the three-dimensional boundary layer and the primary cross-flow instability over a swept wing will be analysed through two experimental campaigns.

If successful, the research will contribute to the body of knowledge related to plasma actuators and their operation and influence on the base-flow and cross-flow instability present on swept wings. Once the interaction between the induced velocity by the plasma actuator and the base-flow and cross-flow instability is better understood, actuators can be designed and controlled in such a way to guarantee a beneficial effect in terms of laminar-to-turbulent transition. Such a finding would be another step in paving the way for more efficient and sustainable flight.

2

State of the Art

This chapter provides the reader with the fundamentals of boundary layers and an overview of the relevant literature associated with the physical mechanisms and control of the cross-flow instability. The boundary layer fundamentals are discussed in section 2.1, whereas the physical mechanism and manifestation of the cross-flow instability are covered in section 2.3. Techniques to control or suppress the instability are briefly discussed in section 2.4. This is followed up by the working principle of plasma actuators and their relation to flow control, which is elaborated in section 2.5. Finally, the research question and objective are introduced in section 2.6.

2.1. Boundary Layer Fundamentals

Following Prandtl's observations [60] regarding the influence of viscosity for high Reynolds number flows, he simplified the Navier-Stokes equations to obtain approximate boundary layer solutions. Due to the influence of viscosity, there is a thin layer of flow where the velocity transitions from zero at the wall to a finite value further away from the wall; the so-called boundary layer, as discussed by Schlichting & Gersten [74]. The thickness of the boundary layer is often expressed as the wall-normal location where the velocity reaches 99% of the free-stream velocity and guides as a barrier between the inviscid free-stream flow and the boundary layer flow, where the viscosity has a non-negligible influence. For a two-dimensional flow, the Navier-Stokes equations can be simplified to equations 2.1 and 2.2, also known as Prandtl's boundary layer equations.

$$\frac{\partial u}{\partial x} + \frac{\partial v}{\partial y} = 0 \tag{2.1}$$

$$\frac{\partial u}{\partial t} + u\frac{\partial u}{\partial x} + v\frac{\partial u}{\partial y} = -\frac{1}{\rho}\frac{dp}{dx} + \nu\frac{\partial^2 u}{\partial y^2} + \frac{F_x}{\rho} \tag{2.2}$$

These equations represent the continuity and momentum equation in x-direction respectively, and are rather powerful in understanding and predicting the behaviour of the boundary layer under certain conditions, such as adverse pressure gradients or external body forces.

Boundary layer transition refers to process during which the boundary layer is changing from a laminar state to a turbulent state. Whereas laminar boundary layers feature coherent fluid layers and momentum is exchanged via diffusion, turbulent boundary layers are characterised by the chaotic motion of the fluid particles and the increased amount of momentum exchange. These characteristics are visualised in figure 2.1. Due to the turbulent mixing, strong velocity gradients appear close to the wall, resulting in a 'fuller' velocity profile compared to that of the laminar boundary layer. Strongly related to these boundary layer velocity profiles is the associated skin friction (τ), which is proportional to the viscosity and the velocity gradient in wall-normal direction ($\partial u/\partial y$), according to equation 2.3:

$$\tau = \mu\frac{\partial u}{\partial y}\Big|_{wall} \tag{2.3}$$

From this relationship it can be deduced that the turbulent boundary layer, with its fuller profile and thus higher velocity gradients, is responsible for larger levels of skin friction when compared to the laminar boundary layer. This crucial difference is the foundation for many research campaigns aimed towards further understanding the phenomenon of boundary layer transition. Reducing the shear stress and skin friction drag by delaying laminar-to-turbulent transition can be a straight forward method to increase the aerodynamic efficiency, which is consequently accompanied by a reduction in fuel consumption.

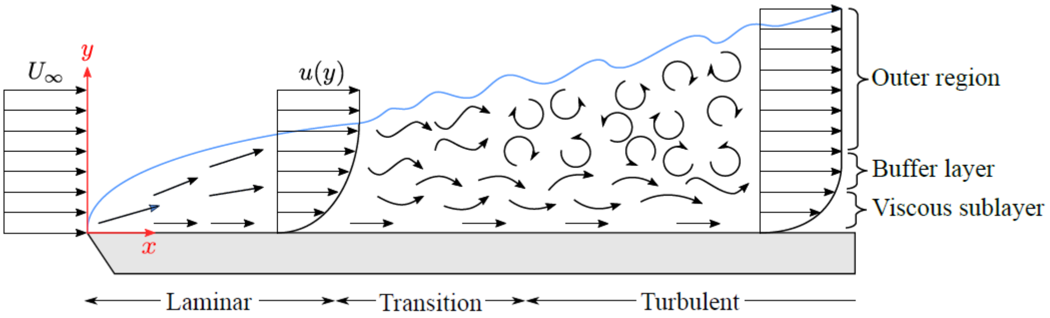

Figure 2.1: Schematic representation of the evolution of a boundary layer over a flat plate. As from Michelis [53].

As previously mentioned, the simplified Navier-Stokes equations are helpful in describing boundary layer phenomena. Besides their velocity profiles, another aspect that distinguishes the laminar and turbulent boundary layer is their respective resistance to boundary layer separation. From the boundary layer equations, it can be shown that when there exists a region with an adverse pressure gradient ($\partial p/\partial x > 0$) near the wall, the situation can occur where at some location the low kinetic energy fluid particles cannot penetrate the region of increased pressure and therefore start to deflect from the wall, as described by Schlichting & Gersten [74]. This phenomenon is referred to as boundary layer separation and visualised in figure 2.2.

As the mixing of particles in the turbulent boundary layer leads to higher levels of kinetic energy close to the surface in comparison with the laminar boundary layer, the turbulent boundary layer is considerably more resistant to separation. It is for this reason that in many industrial applications it is favourable to promote early laminar-to-turbulent transition. For these cases the higher levels of skin friction due to the turbulent boundary layer are often greatly outweighed by the reduction in wake drag. As an example, vortex generators on aircraft wings or high-lift devices aim to delay separation by creating vortices that exchange low-momentum flow with high-momentum flow near the wall. As the higher momentum flow near the wall is more resistant to larger adverse pressure gradients, separation is postponed to higher angles of attack.

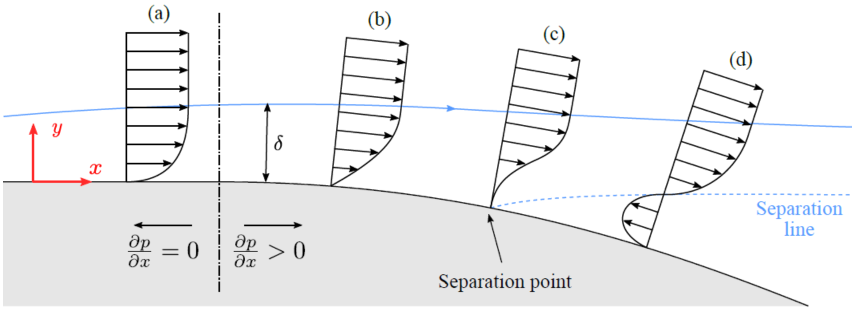
(a)
(b)
(c)
(d)
y
x
δ
$\frac{\partial p}{\partial x} = 0$
$\frac{\partial p}{\partial x} > 0$
Separation point
Separation line

Figure 2.2: Boundary layer separation. The wall-normal velocity distribution features an inflection ($\partial u/\partial y = 0$) and the streamlines move away from the surface. Boundary layer thickness indicated by δ. As from Michelis [53].

Because of the strong influence of the boundary layer on the external flow, the mechanisms leading up to laminar-to-turbulent boundary layer transition have been and currently are studied extensively. Morkovin et al. [55] summarised these mechanisms into five different paths, which can be found in figure 2.3, where they are denoted by the letters A, B, C, D and E. The process in which external disturbances, such as surface roughness or free-stream fluctuations, enter the boundary layer as steady or unsteady fluctuations is referred to as receptivity, as elaborately studied by Saric et al. [71].

When the amplitude of these disturbances is small, the growth is weak and can be regulated and controlled in various ways, such as through mass fluxes or imposed pressure gradients. Although the flow structures considered for ’Primary Modes’ (’A’) can be very diverse, when undergoing further temporal or spatial amplitude amplification, the boundary layer is modified in such a way that it gives rise to ’Secondary Mechanisms’. These instabilities often have a much higher growth rate and are the cause for the initiation of flow breakdown and turbulence. When provided with the proper initial conditions, the boundary layer fluctuations can undergo significant growth due to the interaction of multiple non-orthogonal stable modes. This transient growth can then lead to primary instabilities (’B’), secondary instabilities (’C’) or immediate breakdown (’D’). Finally, when magnitude of the free-stream fluctuations is so large that disturbances no longer undergo (transient) growth, the transition process is bypassed and as such turbulent spots will appear as the flow rapidly becomes turbulent (’E’).

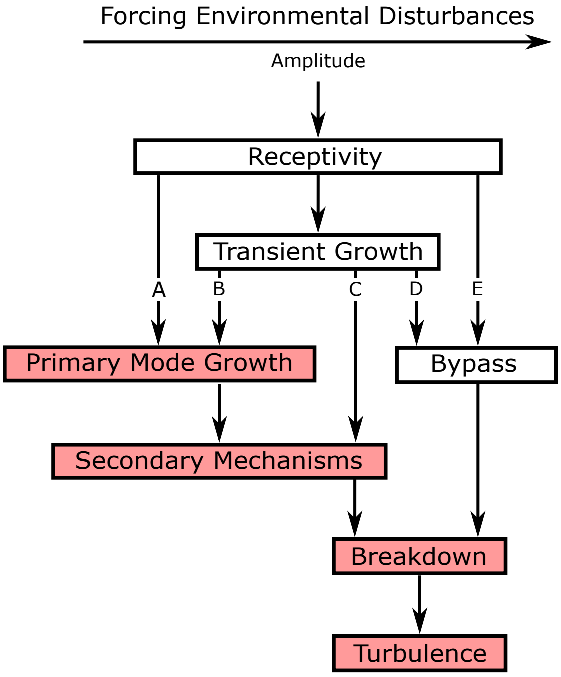

Figure 2.3: Paths towards breakdown and turbulence, as adapted from Morkovin et al. [55]

This research focuses on the transition path (shown in red) and denoted by the letter ’A’ in figure 2.3, which features small external disturbances that lead to, initially, primary and secondary instabilities and ultimately breakdown and turbulence. In two-dimensional flows, when external disturbances enter the boundary layer, stream-wise unstable waves arise through the process of receptivity, as investigated by Baines et al. [4]. These waves are known as Tollmien-Schlichting (TS) waves. TS waves are very receptive to free-stream disturbances and are strongly amplified under adverse pressure gradients. It is for this reason that the TS instability is the main cause for transition in most two-dimensional boundary layers and a lot of research focuses on techniques capable of suppressing the amplification of these Tollmien-Schlichting waves. In order to predict the location of boundary layer transition, Van Ingen [88] presented the e^N-method, which is adequate for two-dimensional incompressible flows.

The TS waves grow in amplitude when traversing in stream-wise direction. Although initially the TS waves can be considered uniform in span-wise direction, three-dimensional disturbances rapidly arise due to the secondary instabilities generated by the primary modes. These three-dimensional disturbances take the form of vortices and other structures and subsequently develop into turbulent spots. These turbulent spots complete the transition process, as breakdown into fully turbulent flow is followed shortly after, as presented by Schlichting and Gersten [74].

2.2. Swept Wing Instability Mechanisms

The previous section provided a brief review of the fundamentals of two-dimensional boundary layers and the paths towards transition and turbulence. Although Tollmien-Schlichting waves are the dominant mechanism initiating transition in two-dimensional boundary layers, different scenarios arise in the case of swept wing flows and three-dimensional boundary layers. It has been observed that for swept wing flows, four transition mechanisms are present. Bippes [7] investigated each instability mechanism with a separate physical model with the aim to provide a more detailed understanding of swept wing transition. Here, a brief summary of the various subsonic boundary layer transition mechanisms is presented.

First of all, the stream-wise or Tollmien-Schlichting instability is present in swept wing boundary layers. As mentioned in the previous section, TS waves are very susceptible to adverse pressure gradients and as such, to limit the influence of the TS instability on the transition process in three-dimensional boundary layers, laminar flow airfoils are often employed. These airfoils boast a rather aft-positioned transition point due to the considerable length of favourable pressure gradient.

In the presence of concave surfaces, the flow starts to roll over as it forms counter-rotating vortices aligned in the stream-wise direction. These Görtler vortices distort the boundary layer velocity distribution and give rise to secondary instabilities, which are responsible for the initiation of the transition process, as described by amongst others, Saric et al. and Schrader et al. [24, 43, 68, 76]. As airfoils generally only feature concave regions in the vicinity of the trailing edge of the pressure surface, the Görtler instability is of limited influence on the transition process that occurs downstream of the leading edge.

The third instability mechanism that is briefly discussed is the attachment-line instability. The (imaginary) attachment line is formed when the points of maximum pressure are connected, as described by Hall et al. [25]. For an unswept wing or in a two-dimensional scenario, the attachment line therefore lies exactly on the leading-edge stagnation points. For a swept wing however, the flow does not fully stagnate and instead moves outboard along the wing leading-edge. The instability of this three-dimensional attachment line boundary layer can cause early laminar-to-turbulent transition and should therefore be mitigated by selecting an adequate sweep angle and leading edge radius, as discussed by Poll [58] and Hall & Malik [23]. It is for this reason that the attachment-line instability is of limited importance when the aerodynamic body is carefully designed.

The last transition mechanism described by Bippes [7] that is responsible for boundary layer transition over swept bodies is the cross-flow instability (CFI). Due to its relevance with respect to boundary layer transition in swept-wing flows as well as in this research the cross-flow instability is discussed more elaborately in the next section.

2.3. Cross-flow Instability

For swept wings, according to simple sweep theory, the free-stream velocity can be decomposed into an effective velocity, which is in the direction perpendicular to the sweep angle, and a cross-flow velocity, which is aligned parallel to the sweep angle. The streamlines over a swept wing are highly curved due to the influence of the sweep angle and the pressure gradients perpendicular to the swept leading edge, as shown by Reed & Saric [63]. The force equilibrium of an air particle travelling along a streamline near the wing consists of pressure forces, which are induced by the curvature of the wing, and centrifugal forces, which are instead induced by wing sweep. Although this equilibrium exists in the inviscid flow, in the viscous boundary layer where the velocity and momentum are much lower, this equilibrium breaks down. This imbalance results in an additional velocity component perpendicular to the tangential velocity. This additional velocity component is referred to as the cross-flow component and can be seen in figure 2.4.

As the cross-flow velocity attains the value zero at the wall (i.e. no-slip condition) and the cross-flow component reduces to zero in the inviscid flow field, an inflection point must exist when the cross-flow component has a finite value in between these two regions. This indicates that the cross-flow component inherently causes an instability in the three-dimensional boundary layer. With its maximum velocity

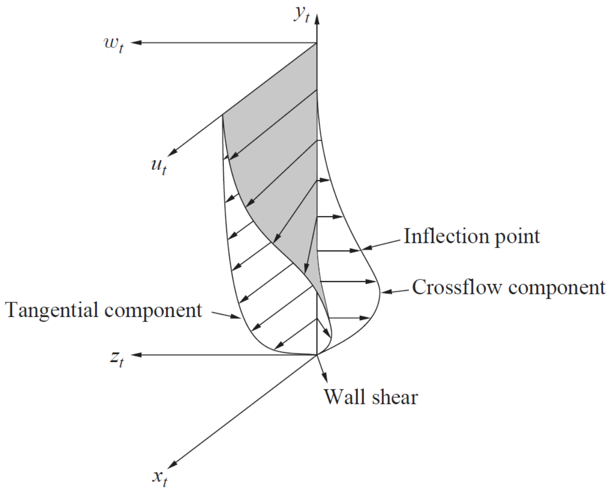

Figure 2.4: Illustration of a swept wing boundary layer featuring the cross-flow component. The cross-flow component is not to scale; in reality its amplitude and vertical extent is a small percentage of the stream-wise component. As from White & Saric [93].

magnitude at some location in wall-normal direction, the cross-flow component results in the formation of co-rotating vortices, which are slightly angled with respect to the mean flow direction. These cross-flow vortices (CFV) can be of the stationary or travelling kind [8], depending on the receptivity process and the magnitude of the external disturbances.

Although initially relatively weak, the cross-flow vortices modulate the boundary layer, as they displace high-momentum flow from higher regions in the boundary layer down to regions of lower momentum and vice versa. This modulation of the boundary layer yields alternating stream-wise streaks of low and high momentum and therefore reduced and increased levels of skin friction. These streaks can be seen in figure 2.5, which shows the cross-flow instability pattern on a 45° swept wing that has been tested in the TU Delft Low Turbulence Tunnel (LTT) at a Reynolds number of $1.3 \cdot 10^6$ by Serpieri [80]. As the CFVs displace momentum in the boundary layer, instabilities appear in the regions of large velocity gradients, reminiscent of the Kelvin-Helmholtz instability. These secondary instabilities are rather localised and characterised by explosive growth rates, resulting in a jagged transition front as seen in figure 2.5.

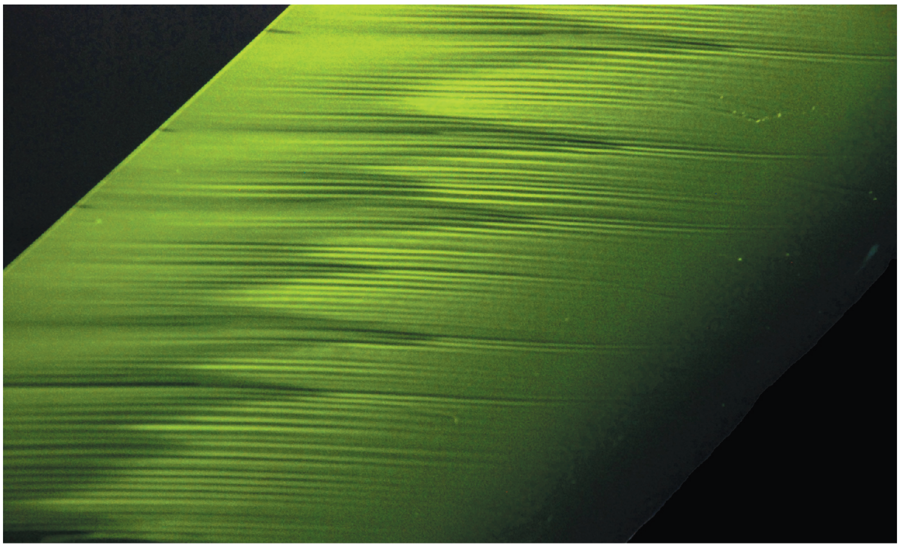

Figure 2.5: Swept wing covered in fluorescent oil, showing the trace of the cross-flow vortices and the jagged transition front. The flow is coming from the right. As from Serpieri [80].

To conclude, the boundary layer over a swept wing becomes primarily unstable due to the cross-flow instability, which is characterised by stationary and travelling instability modes. It is for this reason that various theoretical, numerical and experimental studies have been performed on the three-dimensional receptivity process and the physical mechanisms responsible for cross-flow induced transition. Experimental investigations regarding the cross-flow instability have been mainly carried out in the United States by Saric and colleagues [72, 93] at the Arizona State University (ASU) and Texas A&M University, by Bippes and colleagues [8, 12] at DLR (Deutsches Zentrum für Luft- und Raumfahrt) in Germany and in Russia by Kachanov and co-workers [34, 35]. The following sections provide an overview of numerous relevant investigations and conclusions regarding the cross-flow instability.

2.3.1. Receptivity of Three-Dimensional Boundary Layers

Previous experiments and simulations were found to support the hypothesis that early non-linear interaction and environmental conditions play a significant role in the growth of the two cross-flow instability modes. Müller & Bippes [56] note that for their experiment featuring a swept plate in a 0.15% turbulence environment, both instability modes undergo approximately equal growth. Here, the turbulence level is expressed as the root-mean square of the velocity fluctuations divided by the free-stream velocity, or $Tu = 1/Q_\infty[1/3(u'^2 + v'^2 + w'^2)]^{1/2}$. When this test was repeated at a lower free-stream turbulence level of $Tu = 0.08\%$, the stationary mode was found to be significantly more amplified and have a higher saturation amplitude in comparison with the travelling mode, as seen in figure 2.6. These observations indicate a relationship between the two different modes their growth rates and the presence of external disturbances.

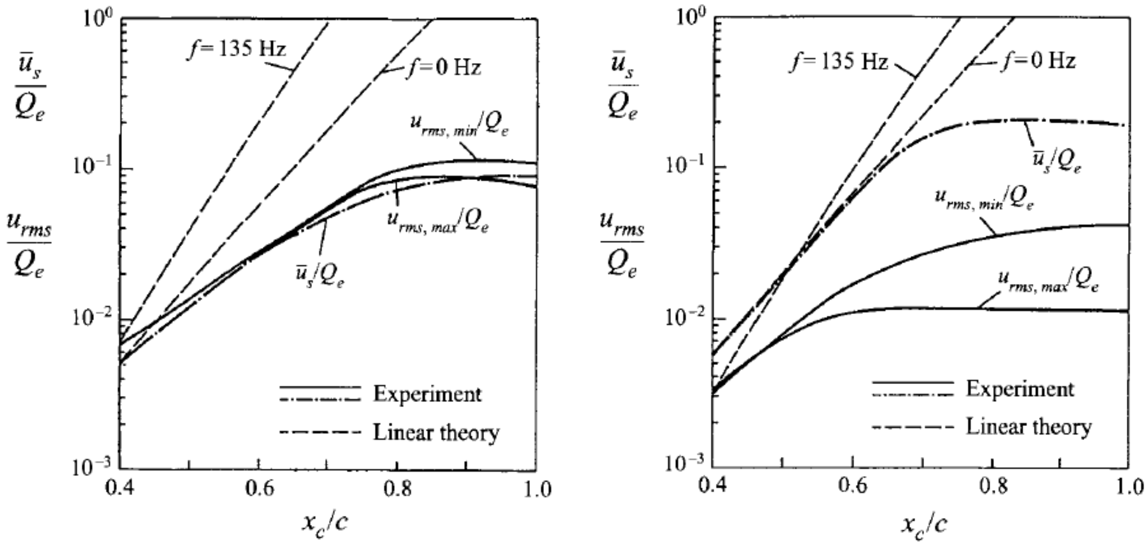

(a) (b)

Figure 2.6: Spatial growth rates and saturation amplitude for the stationary CFVs ($\bar{u}_s$) and travelling waves (u_{rms}) for wind tunnels featuring a turbulence level of 0.15% (a) and 0.08% (b). As from Deyhle & Bippes [12].

According to linear stability theory, as elaborated and discussed by amongst others, Mack [49], the amplification rates of these steady and unsteady disturbances are not equal, with the travelling mode having a greater growth rate than the stationary mode. In a significant amount of experimental investigations however, it is found that the stationary vortices are more amplified, as mentioned by Saric & Reed [63] and as observed by Müller & Bippes [56]. This discrepancy motivated the further work performed by Deyhle & Bippes [12], as they investigated the effects of four environmental conditions on the growth and saturation of the steady and unsteady instabilities, which are the surface roughness, free-stream turbulence, sound and mean flow inhomogeneities. Consequently, it was found that sound and flow non-uniformities have little effect on the instability development in the boundary layer.

To assess the effect of surface roughness on the growth rate of the two instabilities, Deyhle & Bippes [12] studied three levels of surface roughness. Transition occurred upstream and an increase in the saturation amplitude of the cross-flow vortices was observed with increasing surface roughness, whereas the growth rate remained similar. The travelling mode its amplitude and growth rate did not respond as strong and seemed to be only affected by secondary effects.

Increasing the free-stream turbulence from 0.15% to 0.27% led to insignificant changes in the initial amplitude of the cross-flow vortices, but a reduction in saturation amplitude further downstream. Clearly the free-stream turbulence reduced the growth rate of the stationary mode. Although the growth rate of the travelling mode was also less amplified, the initial amplitudes were found to be significantly higher, indicating the ability of free-stream turbulence to initiate the non-stationary cross-flow waves. Increasing the turbulence level further to 0.57% showed the same trend, as the growth rate of the stationary vortices was further suppressed, with their amplitude now even decreasing, whereas the non-stationary modes saw an increase in initial amplitude and a reduction in growth rate. Depending on the roughness height, Deyhle & Bippes [12] mention a cut-off value for the turbulence intensity of 0.2% beyond which the travelling modes will dominate. Laminar-to-turbulent transition is then accelerated for increasing free-stream turbulence levels.

In a later review article, Bippes [8] reiterated the influence of surface roughness on the initialisation of stationary cross-flow vortices and the effect of the free-stream turbulence on the initialisation of travelling waves. Considering the difference of each factor with respect to the receptivity process, stationary cross-flow vortices are primarily observed in lower turbulence environments, whereas the travelling waves dominate in higher free-stream turbulence flows.

This statement was further supported by the experiments performed by Downs & White [14]. They performed experiments in the TAMU Klebanoff-Saric wind tunnel (KSWT) and used turbulence screens to allow for tests at turbulence intensities between 0.02% and 0.20%. The results were in agreement with the hypothesis that the surface roughness is responsible for initiating the steady disturbances and has a large impact on their amplitudes, whereas the free-stream turbulence affects the growth of both the steady and unsteady disturbances. Both surface roughness and an increase in free-stream turbulence influenced the initial amplitude of the non-stationary modes and an increase in free-stream velocity fluctuations always led to an increase in initial amplitude for the travelling mode.

Clearly the discussed experiments show a strong influence of surface roughness on the initiation of cross-flow vortices with a fixed wavelength. To assess the effect of surface roughness and the spacing of discrete roughness elements on the growth of the cross-flow instability modes, Reibert et al. [64] conducted stability experiments at the Arizona State University Unsteady Wind Tunnel on a 45° swept laminar airfoil. Even though the surface was polished to 0.25 μm roughness (rms, root mean square), the stationary mode remained to be dominant mechanism in the transition process. Reibert et al. [64] placed a full-span array of circular roughness elements with a diameter of 3.7 mm and a height of 6 μm close to the leading-edge ($x/c = 0.023$) to generate the desired span-wise uniform distribution of the stationary mode. Through LST, the most unstable and amplified wavelength of the stationary mode was found to be 12 mm and as such, the roughness elements were positioned 12 mm apart to force this mode. From the power spectral density (PSD) plot, the dominance of the most amplified wavelength and its harmonics is clearly visible, as seen in figure 2.7a. The spectral content is even more obvious when the spacing is increased threefold, to 36 mm, as the wavelengths of λ_s/n with n = 1, 2, 3, ..., n feature strong peaks, as seen in figure 2.7b. Reibert et al. [64] concluded that the nature of the cross-flow instability is extremely sensitive to the leading-edge roughness.

Saric et al. [70] followed up on these results, as they investigated the possibility of achieving a laminar-to-turbulent transition delay by forcing a stationary mode that is sub-critical (i.e. has a smaller wavelength) with respect to the natural, most amplified stationary mode. This method of flow control will be discussed in the next section.

Radeztsky et al. [61] continued on the previous efforts by Saric et al. [70] and Reibert et al. [64] and investigated the effect of discrete roughness elements on the transition location by varying the geometry of the respective elements on a 45° swept airfoil. From hot-wire measurements, it was found that the roughness elements promoted transition for larger diameters and moved the transition point

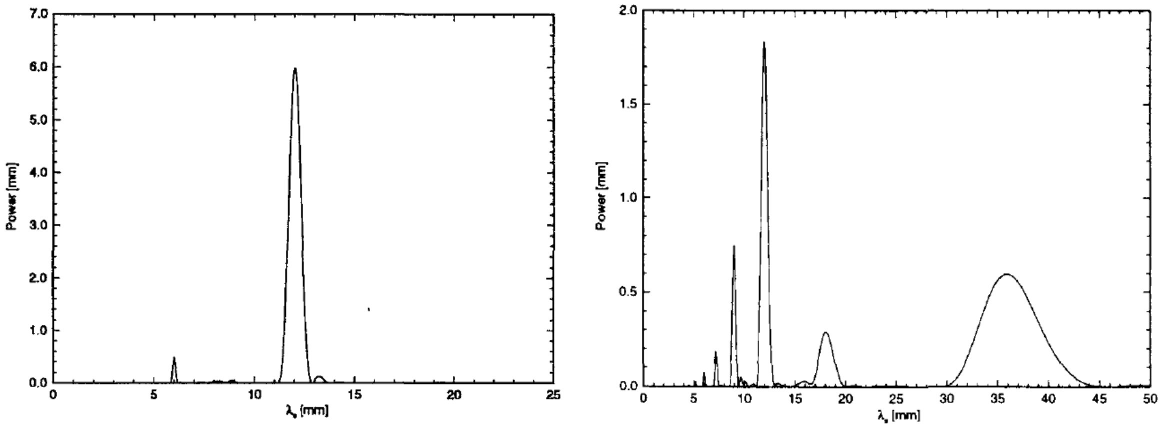

(a) (b)

Figure 2.7: Power spectra obtained from hot-wire measurements taken at x/c = 0.45, Re_c = 2.4 $\cdot 10^6$ and y = 0.9 mm. DREs are located at x/c = 0.023 with a spacing of 12 mm (a) and 36 mm (b). As from Reibert et al. [64].

downstream as the roughness height or diameter were reduced. When the roughness diameter was increased beyond 0.08 times the most dominant mode wavelength, the transition location changed regardless of the chosen roughness height. An increase in roughness diameter increased N and an increase in roughness height decreased N, with N being the disturbance amplitude amplification factor. Furthermore, Radeztsky et al. [61] observed that artificially introduced sound had insignificant effects on the transition location, even when the acoustic waves were introduced at all important and relevant frequencies, in agreement with the results obtained by Müller & Bippes [56].

For additional numerical and experimental studies on the receptivity process of a swept wing boundary layer and the effect of external disturbances, such as free-stream turbulence and surface roughness, on the growth rate of the cross-flow instability modes, the reader is referred to, amongst others, Haynes & Reed [26], Tempelmann et al. [86], Schrader et al. [75], Mistry et al. [54] and Kurz & Kloker [41].

2.3.2. Primary and Secondary Cross-flow Instabilities

As presented in the previous sections, a significant amount of effort has been devoted to understand the influence of external disturbances on the receptivity process with respect to the three-dimensional boundary layer. Although it has been discussed how external disturbances influence the amplitude and growth rate of the two cross-flow instability modes, the physical mechanism that follows and ultimately leads to transition is equally relevant and complex. In 1985, Poll [58] performed an experiment to determine the effect of the yaw angle on the transition process of a long cylinder. Surface flow visualisation techniques were used to study the development of the stationary cross-flow instability and hot-wire probes were employed to monitor local velocity fluctuations and disturbances near the leading-edge and at a location downstream. The hot-wire measurements showed high-frequency fluctuations on top of the primary instability mode prior to breakdown to turbulence, which Poll referred to as high-frequency riders. Some years later, Kohama et al. [38] also reported evidence of these high-frequency fluctuations in their swept wing experiment and classified them as a secondary instability. Since then, further efforts have been made by research groups to understand the formation and evolution of these secondary instabilities, how they affect the transition process and whether they can be predicted and modelled.

Following up on their initial numerical investigation regarding the non-linear development of the cross-flow disturbances in three-dimensional boundary layers [50], Malik et al. [51] aimed to further investigate the evolution of the primary and secondary instability by using linear and non-linear parabolised stability equations (NPSE and PSE) and a two-dimensional eigenvalue approach, respectively. Although the research was successful, perhaps more important is the introduced categorisation of the secondary instability into two dominant modes based on the production mechanism. As presented by Malik et al. [51], the type-I, or z, mode, is identified by large span-wise gradients of the stream-wise flow (i.e. $\partial U/\partial z$). In stationary cross-flow vortices, the type-I mode appears in the updraught region, where the low-momentum flow moves upwards. The type-I mode is further characterised by higher disturbance amplitudes and lower frequencies. The type-II, or y, mode originates from large wall-normal gradients (i.e. $\partial U/\partial y$) and is located on top of the primary cross-flow vortex. The y-modes generally feature lower amplitudes and higher frequencies compared to the z-mode. The locations of the various secondary instabilities can be found in figure 2.8.

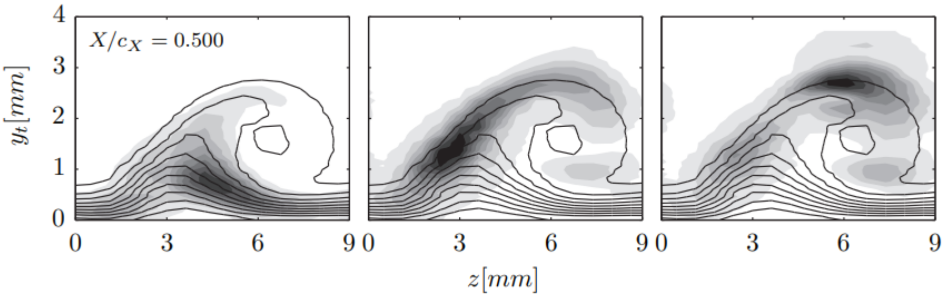

Figure 2.8: Time-averaged velocity (black lines) and velocity fluctuations (grey scale) for various frequency bands pertaining to the type-III instability (left), the type-I mode (middle) and the type-II mode (right). As from Serpieri & Kotsonis [82].

Following the research on the secondary instability by Malik et al. [50] and Fischer & Dallmann [21], Janke & Balakumar [31] performed a theoretical investigation on the saturation of stationary cross-flow vortices and the rise of secondary instability modes using PSE calculations and Floquet theory. Besides the aforementioned type-I and type-II mode, they further identified a type-III mode. This type-III mode has a lower frequency in comparison with the other two secondary instability modes and exists through the interaction of stationary cross-flow vortices and travelling waves, indicating a dependence on free-stream turbulence levels.

As breakdown to turbulence is caused by the high-frequency secondary instability appearing after primary instability saturation, rather than the primary instability itself, White & Saric [93] performed a detailed experimental study on the secondary instability mode and its relationship towards transition. Following the experiments by, amongst others, Reibert et al. [64] and Radeztsky et al. [61], White & Saric performed wind tunnel experiments at ASU on a 45° swept wing featuring the ASU(67)-0315 airfoil. The zero-lift angle of attack of the wing was set at -3.4° and hot-wire measurements were conducted at a Reynolds number of $2.4 \cdot 10^6$. This baseline case featured a span-wise array of micron-sized roughness elements of 18 μm tall that were spaced 12 mm apart, equal to the most amplified stationary cross-flow wavelength. By traversing the hot-wire system in the stream-wise direction and capturing the mean flow velocity and velocity fluctuations at each station, the stream-wise development and growth of the various secondary modes could be tracked. Both the type-I and type-II secondary instability were identified and their explosive growth rates were documented. Consequently, various additional experiments were performed to assess the sensitivity of the secondary instability. When the height of the roughness elements was increased to 54 μm, the amplitude of the low-frequency mode increased accordingly. The low-frequency mode was not found to trigger breakdown independently, as breakdown did not occur until the the primary instability reached its saturation amplitude and the secondary instability was destabilised, indicating that the secondary instability is always critical for transition. When the secondary instability was destabilised, breakdown always occurred within a few percent of the chord. Lowering the Reynolds number to $2.0 \cdot 10^6$ and maintaining the increased roughness amplitude of 54 μm led to an increase in critical wavelength (13.5 mm), whereas increasing the Reynolds number to $2.8 \cdot 10^6$ led to a reduction in critical wavelength (10.2 mm). Finally, it was concluded that the type-I mode dominates when the primary wavelength is sub-critical and the type-II mode dominates when the wavelength is supercritical.

Koch [37] performed an investigation on the spatio-temporal stability of the primary and secondary cross-flow instability modes in the DLR swept plate boundary layer, as studied by amongst others Müller & Bippes [56]. The results showed that breakdown is initiated, but not instantly caused, by the high-frequency riders. These secondary instabilities feature a high growth rate over a short percentage of the chord and reach a non-linear state before breakdown. The findings by Koch not only showed convective instability for the primary cross-flow vortices, but also for the secondary instabilities, implying that the non-linear state of the secondary instabilities can be computed by space-marching methods, such as by PSE or DNS.

As such, Högberg & Henningson [30] performed linear eigenvalue calculations and employed spatial DNS to investigate the growth of the secondary instability modes in Falkner-Skan-Cooke boundary layers. A comparison between the results of the DNS and linear theory showed that non-parallel effects on the growth rates were present and were larger for travelling waves than for the stationary cross-flow vortices. Small random disturbances were superimposed on the cross-flow vortices in the DNS to study the secondary instability. They found a low-frequency (or type-III) mode near the bottom of the cross-flow vortex and a high-frequency (or type-I) mode near the upwelling region of the cross-flow vortex, as was also observed by the likes of Fischer & Dallmann [21], Kohama et al. [38], Malik et al. [50] and Deyhle & Bippes [12]. This was the first time that the secondary instabilities were observed in direct numerical simulations. Interestingly, both the low- and high-frequency instability modes were observed as a result of random forcing, indicating that both modes will invariably appear together, although only one will be dominant due to its growth rate.

As described by White & Saric [93], once the primary instability reaches its saturation amplitude, the secondary instabilities are destabilised and attain significant growth rates that ultimately initiate laminar-to-turbulent transition and breakdown. Following Högberg & Henningson [30], Wassermann & Kloker [90] employed spatial DNS to study nonlinear interactions, the secondary instability and its mechanism leading to transition as well as to laminar-to-turbulent breakdown. They found that the initiation of the secondary instability was related to the maximum localised mean flow deceleration caused by the stationary cross-flow vortices. The UFD technique was investigated by forcing the flow with a wavelength that was two-thirds that of the most unstable wavelength. The more narrowly-spaced co-rotating vortices reached a lower saturation amplitude as their growth was limited by the stronger shear layer. As the maximum flow deformation was lower, the vortices were more resistant to secondary instability modes and a significant delay in transition was obtained. Lastly, Wassermann & Kloker also corroborated the convective nature of the secondary instability mechanism, as they switched off the periodic pulsing at some point in time and tracked the flow field disturbances. Figure 2.9 clearly shows how the turbulent region convects downstream, after which a steady-state is obtained.

Attempts have been made to experimentally validate the results obtained from theoretical and DNS studies. The hot-wire method has an excellent spatial resolution and frequency response, but, considering it is a point measurement technique, is limited in its ability to capture both the spatial and temporal evolution of flow structures simultaneously. Kawakami et al. [36] made an effort to overcome this limitation with a designated experimental set-up. They forced the primary instability mode by discrete roughness elements and initiated the secondary instability by alternating blowing and suction. Similarly to the DNS results obtained by Högberg & Henningson [30], the growth rates of the low- and high-frequency secondary instability were much higher than those of the primary instability. The low-frequency mode was of less importance in the transition process, as the high-frequency instability featured growth rates three times as large. Kawakami et al. [36] concluded that the spatial structures were in accordance with the DNS studies and the convection velocities of the secondary instability modes were 47% and 78% of the free-stream velocity for the low-frequency and high-frequency mode respectively.

Chernoray et al. [10] later followed with an experimental study to build on the results obtained by Wassermann & Kloker [90]. Cross-flow vortex packets were generated in a controlled manner using surface-roughness elements and localised suction. It could be observed that the secondary instabilities developed within the vortex packets featuring the highest amplitudes, independent of the surrounding vortices. The results showed excellent correlation between the location of the type-I and type-II secondary instabilities and the inflection of the cross-flow velocity component. Furthermore, the type-I modes were found to grow faster than the type-II modes. Lastly, Chernoray et al. [10] conjectured a possible relationship between the occurrence of the type-II or type-II secondary instability and the respective vortex geometry. The y-mode appeared for a vortex packet with approximately a 50% larger width-to-height ratio in comparison with the packet of the z-mode.

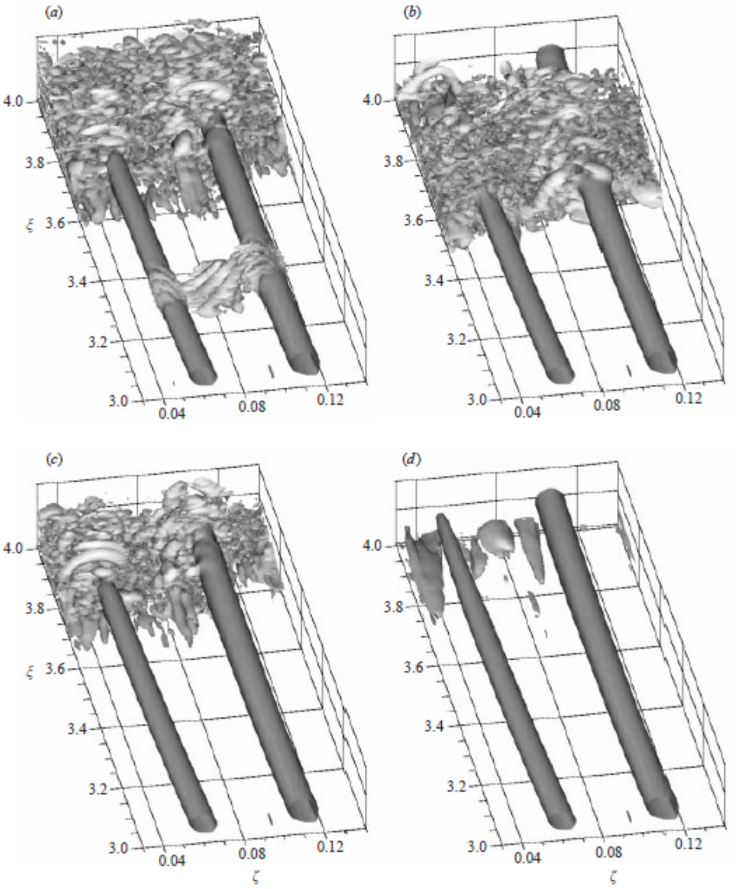

Figure 2.9: λ_2-Isosurfaces showing a cross-flow-vortex-mode packet and the convective nature of the secondary instability once background pulses are turned off. As from Wassermann & Kloker [90].

Serpieri & Kotsonis [82] performed an experimental study on the primary and secondary CFI over a 45° swept wing. The experiment was performed at a chord Reynolds number of $2.17 \cdot 10^6$, a Mach number of 0.075 and an angle of attack of 3°. Through LST, a wavelength of λ_z = 9 mm was found to be the most amplified instability mode, which was experimentally confirmed through earlier studies. The wavelength of the stationary vortices was fixed at 9 mm, as discrete roughness elements were placed near the leading-edge, following the work from, amongst others, Reibert et al. [64] and Radeztsky et al. [61]. The stationary vortices were observed through fluorescent oil flow visualisation, as was the jagged transition pattern typical for the cross-flow instability [72]. Hot-wire measurements were performed to analyse the organisation of the CFVs as well as to inspect the spectral content of the flow. The primary instability grew until a saturation amplitude, after which the primary instability decayed and unsteady fluctuations underwent rapid growth as the secondary high-frequency instability was destabilised. From the spectral content, two high-frequency modes were detected and quantified; the type-I secondary instability (or z-mode) and the type-II mode (or y-mode). For the first time, tomographic particle image velocimetry (PIV) measurements were conducted to study the chord-wise evolution of the primary instability in the region of saturation. The obtained time-averaged tomographic PIV results showed a good agreement with the hot-wire measurements. Proper orthogonal decomposition (POD) was employed and as a result two modes could be identified, with the higher energy mode corresponding to the type-III secondary instability and the lower energy mode corresponding to the type-I instability. The tomographic PIV measurements allowed for a very detailed study of the spatial configuration and development of the stationary and non-stationary modes.

2.4. Control of the Cross-flow Instability

As shown, diverse experimental, theoretical and numerical studies have been conducted regarding the cross-flow instability and the evolution of the related primary and secondary instability modes. In swept-wing flows, the transition process is governed by the cross-flow instability rather than Tollmien-Schlichting waves, as would be the case for two-dimensional boundary layers. With the current pressure and demand for a more sustainable aviation sector, efforts have been made to suppress or control this cross-flow instability. In his review paper, Joslin [32] elaborates on the objective of laminar flow control (LFC) and presents various active and passive flow control techniques as to how to delay boundary layer transition. This section presents several relevant flow control techniques that have shown promising results in relation to the cross-flow instability.

2.4.1. Discrete Roughness Elements

As described in previous sections, the cross-flow instability is rather susceptible to surface roughness and free-stream fluctuations through the process of receptivity. As the turbulence levels during flight are generally very low, the cross-flow instability manifests itself as steady stationary vortices with a fixed wavelength. It is for this reason that many research studies focus on influencing these vortices and limiting their growth.

The experimental study conducted by Reibert et al. [64] and Saric et al. [70] showed that by placing roughness elements with a spacing smaller than the natural most dominant wavelength, laminar-to-turbulent transition could be delayed. Other experimental, theoretical and numerical investigations by, amongst others, Müller & Bippes [12], Malik et al. [50] and Wassermann & Kloker [90], reported similar results, indicating that this form of flow control can be used as a method to reduce the skin friction drag. As investigated by Wassermann & Koker, by forcing at a sub-critical wavelength, the growth of the most unstable wavelength is suppressed due to the shear generated from the more closely spaced co-rotating vortices. Considering they attain a lower saturation amplitude and are more resistant to the rise of secondary instabilities, laminar-to-turbulent transition is delayed under these conditions.

Where Saric et al. [70] used an array of discrete roughness elements to initiate sub-critical modes and delay transition, White & Saric [92] later attempted to assess the possibilities of variable leading-edge roughness. The aim of such a system would be to allow for wavelength and height variations, resulting in a wider operating range. Their initial system consisting of micro-electrical mechanical systems (MEMS) presented some technical difficulties and thus an alternative pneumatically driven system was chosen. Judging from the results, White & Saric [92] concluded that such an actuator would be capable of delaying transition, although the system itself was rather primitive and required more development.

Hosseini et al. [29] performed direct numerical simulations resembling the flow configuration as in the experiments of Saric et al. [70] and Reibert et al. [64]. The DNS results were in good agreement and showed an attenuation of the most unstable wavelength when sub-critical forcing was in place. Interestingly, when unsteady disturbances were introduced into the flow field, laminar-to-turbulent transition was caused by the breakdown of steady and unsteady cross-flow modes of similar amplitudes, rather than purely by the stationary cross-flow vortices. Also in this scenario, transition could be delayed by sub-critical forcing, indicating the effectiveness of the roughness elements in various flow conditions. The reduction in amplitude corresponding to the secondary instability of the z-type can be clearly observed from figure 2.10.

The idea of DRE and UFD was further proved to be effective for hypersonic flows by Saric & Reed [69] and Schuele et al. [77], who performed experiments on a swept wing and a right-circular cone, respectively. Clearly, the ability of discrete roughness elements to control and suppress the cross-flow instability has been shown through various theoretical, experimental and numerical investigations. However, as the cross-flow instability does not only depend on surface roughness, but also on the levels of free-stream turbulence, the Reynolds number and other factors, a delay in laminar-to-turbulent transition is not always guaranteed, as shown by Downs & White [14]. When the flow conditions are steady and known a priori, the upstream flow deformation technique in the form of discrete roughness elements can yield successful results. In the case of varying external factors, further dedicated research studies will be required to ensure successful and efficient control of the cross-flow instability.

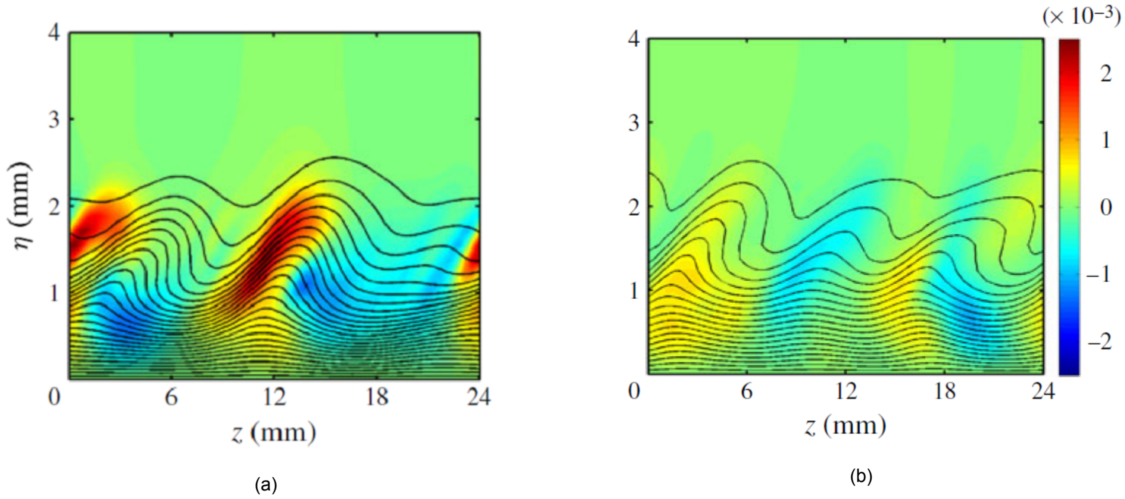

Figure 2.10: Wall-normal plane showing the instantaneous velocity (black lines) and real parts of the Fourier amplitude (contour) for a high-frequency mode of 3622 Hz, taken at x/c = 0.4, for the natural case (a) and sub-critical case (b). As in Hosseini et al. [29].

2.4.2. Suction and Blowing Systems

In an attempt to broaden the operating range, Lohse et al. [46] extended the idea of DREs and assessed the possibility of delaying cross-flow induced transition by employing localised, sub-critically spaced blowing and suction orifices. This flow control method had the advantage that it could be switched on and off and allowed for a variation in initial disturbance amplitude by adjusting the mass flow of the pneumatic actuator. Sharing similarities with the working principle of DRE, the active flow control technique that was utilised in this research study can be classified as a form of upstream flow deformation (UFD). This term covers any flow control technique that attempts to induce particular stationary cross-flow modes with the aim to delay transition. From the hot-wire measurements, it was found that both steady suction and steady blowing were able to delay transition. However, considering the suction case yielded better results and the blowing case is limited in its initial disturbance amplitude as to avoid bypass transition, sub-critical suction seems a better candidate for further development. The reduction in stream-wise velocity fluctuations due to suction can be clearly seen in figure 2.11.

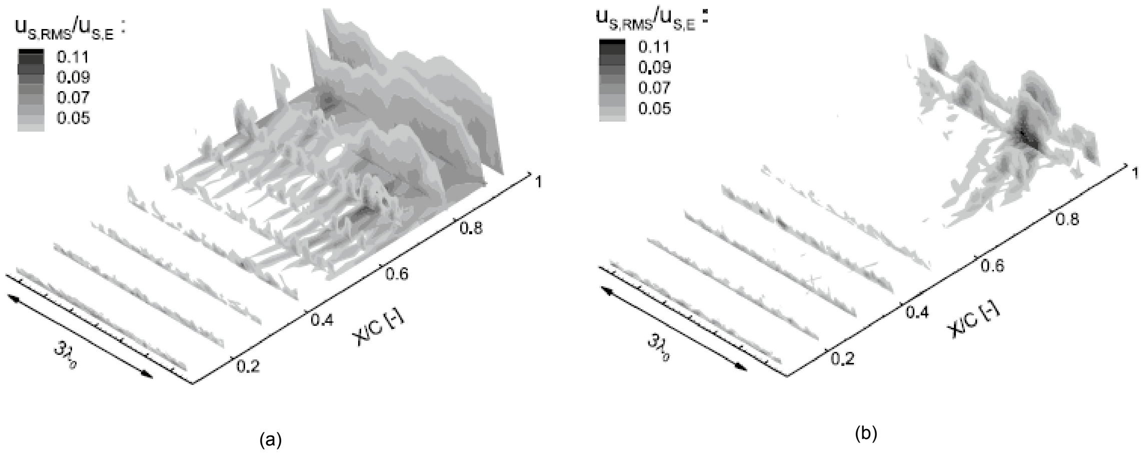

Figure 2.11: Stream-wise velocity fluctuation contours for the case of no control (a) and sub-critically forced suction (b). The reduction in stream-wise velocity fluctuations is clearly visible. As from Lohse et al. [46].

Friederich & Kloker [22] investigated the possibility of transition control through various localised suction configurations, featuring homogeneous suction, suction holes and suction slits. A schematic representation of how such a suction hole acts on the cross-flow vortices and the secondary instability can be found in figure 2.12.

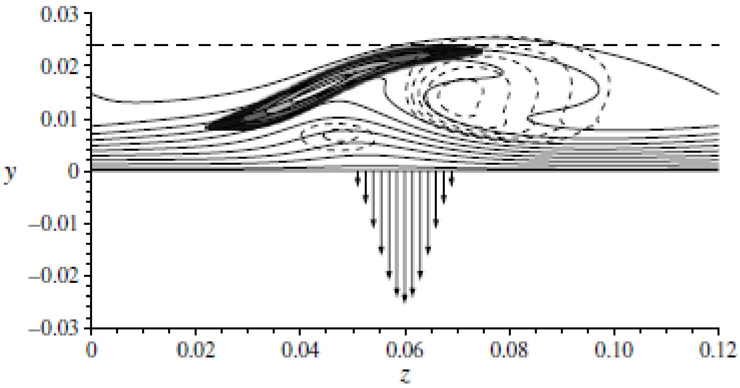

Figure 2.12: Schematic representation of the pinpoint suction set-up for a cross-flow vortex. The solid lines represent the streamline-oriented velocity component, whereas the dashed lines correspond to λ_2-isocontours. The high-frequency secondary instability is visualised by grey scale and the arrows indicate the suction distribution along the hole. As from Friederich & Kloker [22].

This type of flow control is referred to as the pinpoint technique, as introduced by Friederich & Kloker [22]. The technique aims to directly weaken the cross-flow vortices by applying strong localised suction, or in the case of Dörr % Kloker [17] in their DNS study, by utilising plasma actuators to induce a force against and with the cross-flow. From the study performed by Friederich & Kloker [22], it could be concluded that suction can successfully stabilise fully three-dimensional boundary layers featuring large-amplitude cross-flow vortices. Two effects were observed that could explain the mechanism behind the achieved transition delay. By applying suction, the cross-flow vortices were flattened and pulled towards the wall, which resulted in a reduction in span-wise shear and a weakening of the secondary instability. The other effect was found to be slightly counter-intuitive. When the suction was concentrated directly underneath the upwelling region of the cross-flow vortices, rather than directly weakening vortex its rotational motion, the suction induced a pair of counter-rotating vortices. The vortex that was rotating opposite to the primary cross-flow vortex was suppressed rather quickly and the other vortex hampered the primary cross-flow vortex before it was eventually suppressed. These flow alterations led to a drastic change in the position and characteristics of the secondary instability, as the unsteady secondary vortices shifted to be more aligned with the cross-flow direction (i.e. a change from z-type to y-type secondary instability). This span-wise shift also resulted in a reduction in planar angle between the axes of both the primary CFV and secondary vortex. With the in-plane shear significantly reduced, the growth rate of the secondary instability was significantly modulated or even halted in some scenarios. Friederich & Kloker [22] found nine successive holes along the cross-flow vortex yielded the best performance, as this configuration was able to fully suppress the secondary instability. Each hole had a diameter equal to two times the local displacement thickness and the suction velocity was set equal to approximately 20% of the free-stream velocity. They concluded that the additional introduced wall shear due to concentrated suction was not negligible, but the delay in transition far outweighed this effect. If this 'pinpoint' suction method is to be applied in practical applications, it is essential to fix the position of the cross-flow vortices relative to the suction orifices. Alternatively, a slit-version can be used, although this method was found to be less effective.

The flow control technique mentioned so far mostly focused on laminar-to-turbulent transition by the suppression of the most unstable wavelength through sub-critical forcing. Another method to control the cross-flow and the associated cross-flow instability is to suppress the base-flow itself, a form of flow control known as base-flow modification or base-flow modulation (BFM). In his review paper, Bippes [8] noted that the most straight forward method to stabilise the boundary layer velocity profile would be to apply surface suction, as it has the capability of reducing both the cross-flow velocity component and the cross-flow instability. Following up on a previous experiment by Bippes et al. [9], the experimental results showed that the suction technique had a stabilising effect on the cross-flow and the cross-flow instability. However, technical and manufacturing imperfections hurt the suction system its performance, indicating that more research is required to take profit of the full potential of the suction technique. The beneficial change in velocity profiles due to suction can be found in figure 2.13.

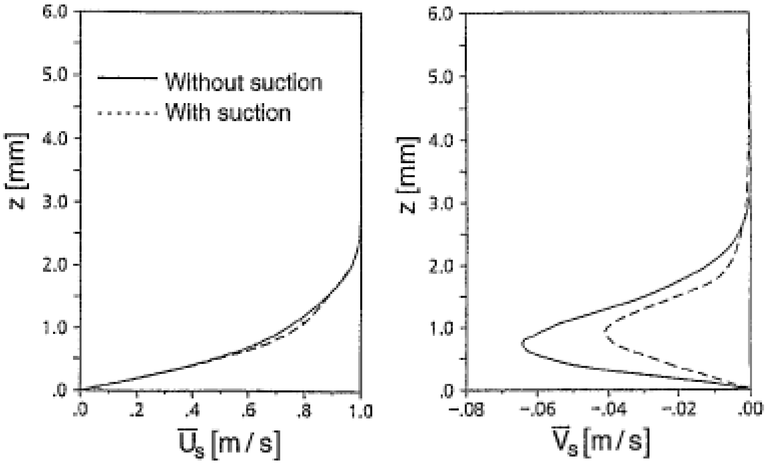

Figure 2.13: Span-wise averaged mean flow profiles of the stream-wise (left) and span-wise (right) velocity component along a streamline with and without suction. As from Bippes [8].

Messing & Kloker [52] investigated the effect of suction on the disturbance evolution in a swept plate boundary layer. Similarly to Bippes [8], they found that suction enhanced the stability of the boundary layer stability as it led to a fuller stream-wise velocity profile and a weaker cross-flow velocity when considered along an inviscid streamline. Nevertheless, too high suction velocities or manufacturing imperfections led to a promotion of transition or bypass transition, indicating the strong sensitivity to external disturbances. Finally, Messing & Kloker introduced the idea of formative suction, where UFD is used to initiate stationary vortices that are consequently controlled by downstream suction orifices. Such a technique could reduce the suction rate for the same degree of stabilisation, resulting in a lower required pump power.

2.5. AC-DBD Plasma Actuators

Although suction systems have shown to be capable of weakening the cross-flow over swept wings, they feature several drawbacks. The, amongst others, high required pump power, tight manufacturing tolerances and difficult integration have resulted in few scenarios where suction systems have been adopted for full-scale flight, as discussed by Joslin [32]. Sub-critical forcing via roughness elements seems a simple yet effective solution for the control of the cross-flow instability, however its operating range is limited due to its static nature. Researchers have explored various other flow control techniques and devices that initially showed distinct advantages over the conventional UFD and DRE methods discussed in the previous sections. A device that has seen a rise of interest over the last decades are plasma actuators. This has been mainly due to their favourable characteristics, as they feature no moving parts, exhibit a high frequency response and can be manufactured and installed in a straightforward manner, as discussed by Benard & Moreau [5]. Various types of plasma actuators exist, such as the Direct Current corona (DC-corona) and nanosecond pulsed dielectric barrier discharge (ns-DBD) actuator, as discussed by Léger et al. [47] and Roupassov [66] respectively, although this research focuses on the alternating current dielectric barrier discharge (AC-DBD) plasma actuator due to the aforementioned reasons. This section introduces the reader to the working principle of the AC-DBD plasma actuator as well as several relevant plasma actuator flow control studies to date.

2.5.1. Working Principle of AC-DBD Plasma Actuators

The general AC-DBD plasma actuator configuration consists of two electrodes and a dielectric layer, which are powered by a power supply and a high voltage amplifier. In the typical asymmetric electrode configuration, one electrode is exposed to the air, whereas the other electrode is encapsulated by the dielectric material. A schematic representation of an AC-DBD plasma actuator can be found in figure 2.14. Once an AC voltage is supplied that causes an electric field larger than the breakdown limit, the air over the electrode is weakly ionised. As the electrode generates an electric field, the ionised air (or plasma) transfers momentum and imposes a body force on the neutrally charged surrounding air, resulting in a localised flow acceleration. This body force is the driving mechanism behind the plasma actuator its function concerning active flow control.

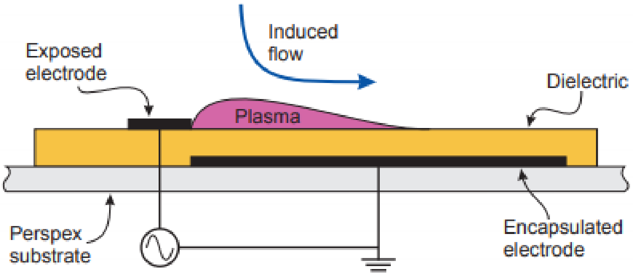

Figure 2.14: Illustration of a typical AC-DBD plasma actuator configuration. As from Erfani et al. [20].

Plasma Formation

Considering the plasma actuator is supplied with an AC signal, which varies in time, the morphology of the plasma is dependent on the position within a cycle. During the negative half-cycle (i.e. when the input signal has a negative slope), the electrons are coming off the exposed electrode, whereas for the positive half-cycle the electrons originate from the dielectric surface. This difference in electron source leads to a variation or asymmetry in the plasma structure, as the electrons do not come off as easily from the dielectric surface when compared to the almost infinite source that is the high voltage electrode, as discussed by Corke et al. [11]. This can be clearly seen in figure 2.15, where the positive half-cycle is characterised by branch-like streamers and the negative half-cycle shows more plume-like microdischarges.

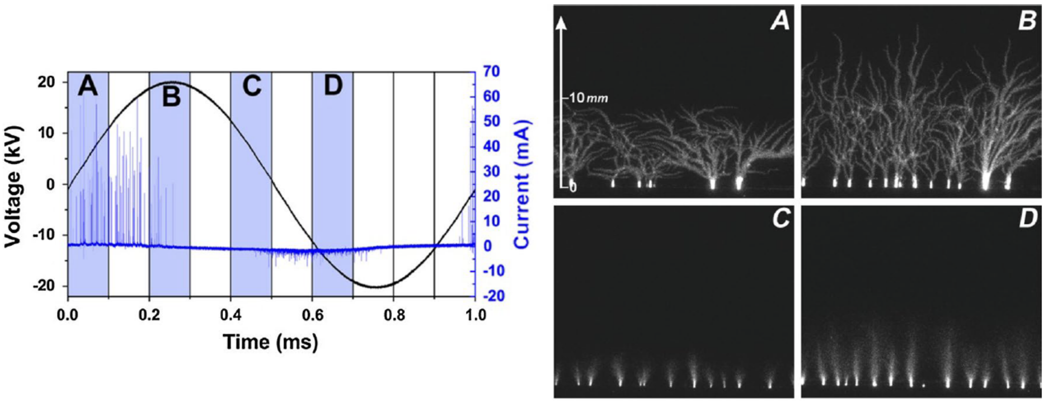

Figure 2.15: AC input and corresponding discharge currents (left) with the corresponding intensified Charged-Coupled Device (iCCD) camera images for each section of the cycle, clearly showing a strong asymmetry. As from Benard & Moreau [67].

Induced Velocity Jet

As mentioned, this plasma formation effectively translates into a body force and an induced velocity jet. This jet is strongest near the wall, can extend up to the length of the covered electrode and reach a maximum velocity of approximately 10 m/s in quiescent conditions, as shown by, amongst others, Thomas et al. [87]. How this velocity jet depends on the geometrical configuration and operating conditions has been the topic of many research studies. Benard & Moreau [5] have shown with the use of experiments that the induced velocity asymptotically increases with frequency and voltage. By increasing the frequency, the discharges that occur at the dielectric surface become filamentary and no longer aid in the production of electric wind. Regarding the geometry of an AC-DBD plasma actuator, it has also been shown that the magnitude of the induced velocity is indirectly affected by the dielectric material and its thickness. For a given voltage and dielectric material, reducing the dielectric thickness leads to a stronger electric field and thus a higher induced velocity, whereas increasing the dielectric thickness allows for higher voltages and therefore a higher maximum induced velocity, as discussed by Thomas et al. [87].

Advantages and Disadvantages

Plasma actuators provide several benefits over previously mentioned flow control concepts. First of all, the frequency and amplitude of the supplied voltage signal can be adjusted to allow for a dynamic range of forcing frequencies and amplitudes. Secondly, in contrast with for example a suction system, the manufacturing process and application of AC-DBD plasma actuators allows for minimal interference with the cross-flow instability, which is very sensitive to surface roughness. Furthermore, the actuators can be manufactured and positioned as to exert flow control in a designated direction and do not feature any moving parts, simplifying their operation and maintenance.

On the other hand, the required high voltage amplifiers that are required for proper operation are expensive and can introduce significant electromagnetic interference. As the authority of plasma actuators does not scale adequately with increasing Reynolds numbers, their effectiveness is limited at these higher Reynolds numbers, as discussed elaborately by Benard & Moreau [5] and Corke [11]. For this reason, it is essential to operate the plasma actuators at locations where their limited control can have a significant impact downstream by utilising the receptivity process. It must be noted that, as the operation of the plasma actuator is inherently unsteady and the cross-flow instability manifests itself as stationary and travelling instabilities, there is the possibility of directly or indirectly triggering unsteady cross-flow instability modes, leading to early transition and breakdown. This interference should therefore be avoided at all times by operating the actuator at a frequency outside the relevant instability frequency band. Furthermore, not only the primary cross-flow instability can be affected by the unsteady character of the plasma actuator, but also the secondary instability, as it similarly is of an unsteady and convective nature, as presented by Malik et al. [51] and Wassermann & Kloker [90].

2.5.2. Flow Control by AC-DBD Plasma Actuators

One of the major advantages of plasma actuators is the flexibility they offer in terms of geometry and directional control. So far, the cross-flow instability control methods that have been discussed can be classified into three categories; that of base-flow modification (BFM), upstream flow deformation (UFD), which includes the method of discrete roughness elements (DRE) and the pinpoint technique. Various numerical and experimental research studies have been performed on the performance of AC-DBD plasma actuators functioning as either BFM, UFD or pinpoint devices for a range of flow conditions, of which several are discussed here.

Discrete Roughness Elements / Upstream Flow Deformation

In their experiment, Schuele et al. [77] assessed the possibility of controlling the stationary CFI modes through patterned passive and active roughness. In contrast with previous cross-flow experiments, where often swept wings or flat plates were used, they opted for a sharp-tipped cone and performed the test in supersonic conditions. To properly induce the cross-flow, the Mach number was set at 3.5 and the model was positioned at an angle of attack of 4.2°. The passive roughness featured evenly-spaced indentations, whereas for the active roughness case, use was made of an azimuthal array of plasma actuators. For each case, two azimuthal spacings were considered. One configuration corresponded to the most amplified mode number, whereas the other was chosen to suppress the most amplified mode with the aim to delay transition. The results of the experiment showed that both the passive and active roughness positively influenced the steady CFI modes, with an increase in transition Reynolds number of 35% in the case of the sub-critically spaced passive roughness. As mentioned in the previous section, the advantage of these plasma actuators lies in their ability to produce a wide spectrum of frequencies and amplitudes.

Following up on the DRE flow control strategy, Yadala et al. [96] conducted an experimental investigation on laminar-to-turbulent transition delay using AC-DBD plasma actuators. DREs were mounted near the leading edge of the respective swept wing, with a spacing equivalent to the wavelength of the most critical mode ($\lambda_z = 8\ mm$) to ensure consistent stationary cross-flow vortices. The plasma actuators were installed slightly further downstream to force the sub-critical modes ($\lambda_z = 4\ mm$). The actuator was operated at a high AC frequency ($10\ kHz$) such that the introduced frequencies did not influence the more unstable frequency bands. Two plasma actuator configurations were considered that both imparted momentum against the incoming flow; one where the stationary CFVs pass over the plasma jet and one where the vortices pass in between adjacent jets. The two configurations are visualised in figure 2.16.

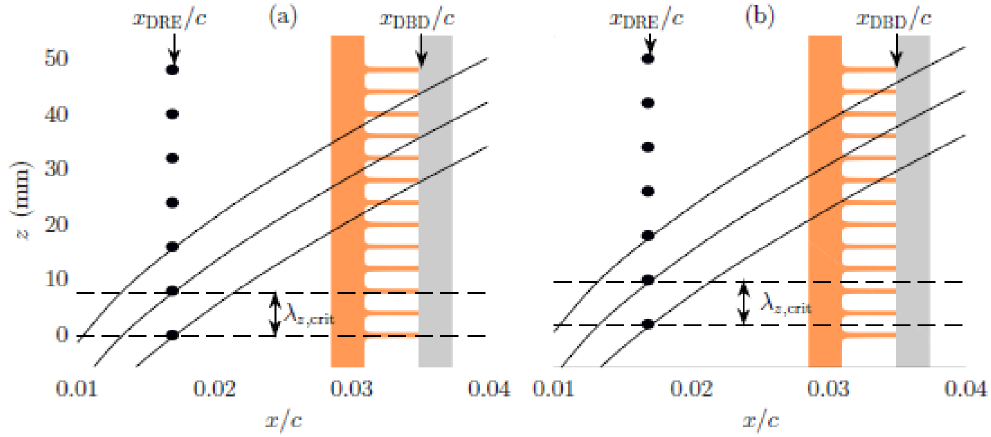

Figure 2.16: Experimental set-up where the CFVs pass over the plasma jets (a) and in between the plasma jets (b). Furthermore, the discrete roughness elements, the DBD actuator with its exposed electrode (grey) and encapsulated electrode (orange) and three inviscid streamlines are shown. As from Yadala et al. [96].

Infrared (IR) thermography was used as a flow visualisation tool to detect shifts in the transition front. Although both aforementioned configurations yielded a delay in laminar-to-turbulent transition, the delay of the latter was only half of the former configuration. Interestingly, the relative position of the plasma jet with respect to the incoming cross-flow vortices is of importance in terms of control performance, as concluded by Yadala et al. [96]. This is in agreement with the results obtained by Dörr & Kloker [17], who observed a large sensitivity in the success of the pinpoint technique regarding the orientation and location of the plasma actuator with respect to the cross-flow vortices. It can be argued that the successful transition delay is rather the result of the pinpoint technique than due to the DRE flow control strategy.

Dörr & Kloker [18] investigated the possibility of controlling cross-flow induced transition by the DRE method using DBD plasma actuators. Direct numerical simulations were performed for two forcing scenarios; in one case the plasma actuators forced against the cross-flow, whereas in the other case the plasma actuators forced in the cross-flow direction. The results showed that forcing against the cross-flow had a direct, positive influence on the boundary layer stability due to a reduction of the cross-flow, whereas forcing in the direction of the cross-flow resulted in the opposite effect. In the former case, flow stabilisation occurred for a wide range of forcing strengths, although excessive forcing led to flow tripping and a promotion of transition, as is the case with excessive suction or blowing.

Serpieri et al. [84] performed an experimental investigation on the forcing of selected CFI modes on a 45° swept wing featuring uniformly spaced AC-DBD plasma actuators. Four plasma actuator geometries were developed for the experiment; a critical geometry, a sub-critical geometry, a super-critical geometry and a spanwise-uniform actuator. Use was made of IR thermography and time-resolved PIV to qualitatively and quantitatively assess the control of the plasma actuators and the boundary layer velocity field, respectively. The IR thermography highlighted the influence of the plasma actuators, as the spanwise-uniformly-spaced streaks as well as the jagged transition front could be clearly observed. A reduction in growth rate was found for the sub-critical case, whereas an increase in growth rate was seen for the plasma actuator featuring a critical spacing. Spectral analysis of the flow field however, showed a strong amplification of fluctuations in the cases where the plasma actuator was switched on, regardless of the wavelength. Two possible mechanisms were presented for the occurrence of these fluctuations. As the plasma actuators inherently introduced an unsteady body-force component into the flow, it could have introduced low-frequency fluctuations into the boundary layer and excite disturbances. A second mechanism could be related to the modification of the mean boundary layer through steady forcing, affecting its stability and receptivity characteristics to various instability modes. Further research efforts are required to present a conclusive answer.

Base-flow Modification

Although it has been shown that plasma actuators acting as UFD/DRE devices are effective in controlling the cross-flow instability and the consequent cross-flow induced transition, the method of operation features a high sensitivity to specific flow conditions, such as free-stream disturbances and surface roughness. Instead, the base-flow modification approach aims to directly influence the cross-flow velocity profile rather than to attenuate the cross-flow instability, rendering it less sensitive to external disturbances. The drawback of this technique is that it requires significantly more energy compared to the UFD/DRE method and thus has to provide a significant improvement in flow control authority to be competitive.

Yadala et al. [95] investigated the possibility of delaying swept-wing laminar-to-turbulent transition through base-flow modification using AC-DBD plasma actuators. As the swept-wing boundary layer is extremely sensitive to surface roughness and thickness variations, a prototype spray-on technique was used to fabricate minimum thickness silver electrodes. The most unstable wavelength for the tested flow conditions was found to be in the vicinity of $\lambda_z = 8\ mm$ according to LST and consequently, to provide a worst case scenario and attain a more uniform transition front, the flow was forced by placing discrete roughness elements near the leading edge with a spacing of $8\ mm$. The plasma actuators were installed slightly downstream and two configurations were considered; one where the generated body force was against the cross-flow ($-F_x$) and one where the body force was in the direction of the cross-flow (F_x). A visualisation of the forcing set-up can be found in figure 2.17.

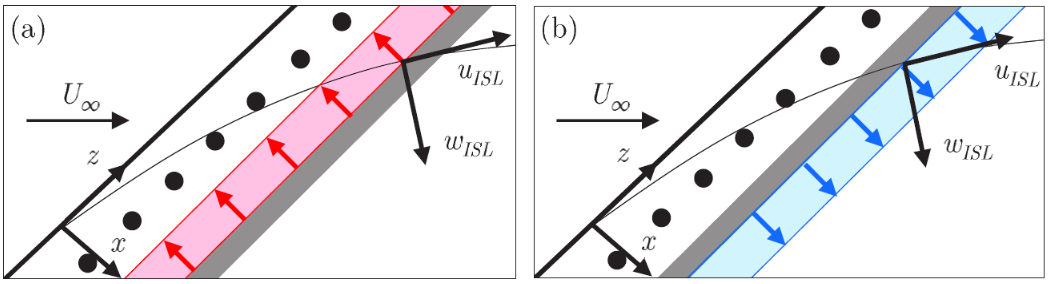

Figure 2.17: Experimental set-up of forcing against the cross-flow (a) and in the direction of the cross-flow (b). The discrete roughness elements (black dots), the exposed electrode (grey bar) and an inviscid streamline (thin line) along with the local streamwise and spanwise velocity components are also visualised. As from Yadala et al. [95].

IR thermography fields showed a downstream shift in transition front in the case of $-F_x$ forcing, whereas an upstream shift in transition front was observed for F_x forcing. It was noted that $-F_x$ forcing and F_x forcing resulted in an artificial decrease and increase of the N-factors, respectively. The N-factor at which transition occurred for the clean configuration was found to be approximately 5.6, and this value was reached at a point further downstream or upstream for the $-F_x$ forcing and F_x forcing cases respectively. Furthermore, the inherent insensitivity of the BFM strategy was demonstrated through this experiment, as the plasma actuator forcing was observed to remain effective even as the most amplified wavelength changed with Reynolds number.

Dörr & Kloker [16] performed direct numerical simulations to study the effectiveness of various flow control techniques, including DBD plasma actuators, on controlling the cross-flow instability. All the techniques had the objective to reduce the cross-flow velocity such that the primary cross-flow instability was weakened and the destabilisation of the secondary instability was delayed. Two plasma actuator configurations were considered; one where the force was applied against the cross-flow and one where the force was applied in span-wise direction, much like the study of Yadala et al. [95]. It was observed that the wall-normal force distribution induced by the plasma actuators should be moderately uniform, as too strong localised forcing could lead to an inflection in the cross-flow velocity profile. The DNS results showed a reduction in cross-flow velocity for both forcing directions, with a stronger decrease for the scenario of forcing against the cross-flow. In both cases the forcing reduced the growth rates of both the stationary and travelling cross-flow vortex modes, which resulted in an attenuation of the secondary instability and delayed laminar-to-turbulent transition significantly.

Rizzetta & Visbal [65] performed large-eddy simulations (LES) to study the possibility of delaying excrescence-induced transition on a swept wing by using AC-DBD plasma actuators. The excrescence was generated near the leading-edge and the plasma actuators were placed parallel to the leading-edge slightly further downstream. The generated wall-parallel body force acted in the chordwise direction. To guide as a reference, simulations were performed on a clean configuration without excrescence and active plasma actuators. The results showed a reduction in lift as the sweep angle increased, in accordance with simple sweep theory. The transition location moved forward for increasing sweep angle, although when excrescence was introduced, laminar-to-turbulent transition occurred immediately downstream of the elements. For a sweep angle of 30° with excrescence and an active plasma actuator, the transition region shifted downstream to a location near that of the clean configuration. For a sweep angle of 45° a delay in transition could not be realised, most likely due to the strength of the instabilities. The plasma actuator was separated into 5 segments (segmented swept actuator, SSA) and re-aligned with the free-stream flow with the objective to increase the effectiveness of the flow control. Although a slight delay in transition was obtained with this new configuration, the region of laminar flow diminished due to the large sweep angle and therefore was not deemed to be efficient.

2.6. Research Objective

As shown, a variety of flow control methods exist, both passive and active, that are able to positively influence the limiting mechanism for swept wing boundary layer transition that is the cross-flow instability. The AC-DBD plasma actuator has seen a rise of interest due to its ability of directional control, the relatively low power consumption and the fact it contains no moving parts. In recent experiments by Yadala et al. [95] and Serpieri et al. [84], AC-DBD plasma actuators were successfully employed to affect the cross-flow instability and cross-flow induced transition through the BFM and UFD control method respectively. Although plasma actuators based on the method of UFD/DRE feature a much lower power consumption, as presented by Dörr & Kloker [18], the success of such actuators is still highly dependent on external factors such as surface roughness, turbulence intensity and Reynolds number. Plasma actuators operating by the principle of BFM are instead more robust to environmental changes, with the most significant drawback being a higher power consumption.

Experimental proof of cross-flow instability control by base-flow modification through plasma actuators was first presented by Yadala et al. [95] in 2018. In this study, Yadala et al. placed an actuator near the leading edge of a swept wing and forced against the direction of the cross-flow component. Although this study has shown that plasma-based base-flow modification can lead to a delay in laminar-to-turbulent transition, the physical mechanism that causes this has not yet been experimentally investigated. It is for this reason that the following research objective is formulated:

To assess how an AC-DBD plasma actuator, with the objective of base-flow modification, affects the cross-flow instability in relation to cross-flow induced transition over a swept wing.

In order to achieve this objective, first of all the AC-DBD plasma actuator and its performance are quantified in quiescent conditions, both in terms of electrical and mechanical characteristics. This characterisation yields information on the power consumption as well as the flow control authority, which can be used for comparison and in future optimisation studies. Subsequently, the effect of the actuator on the swept wing boundary layer is investigated, as the change in boundary layer velocity profile is the essence of base-flow modification. Finally, the evolution and development of the primary cross-flow instability is studied with and without plasma actuator.

Several theoretical models and flow measurement techniques are employed during this thesis to aid in answering the research question. Chapter 3 introduces the reader to these theoretical methods. A description of the experimental setup is provided in chapter 4, whereas the results are elaborated in chapter 5. A conclusion regarding the outcome of thesis and further recommendations are presented in chapter 6.

3

Methodology

This chapter provides a background on the leading methods and theories that are employed during this research. Techniques not introduced in this chapter are instead introduced in the report when appropriate. First of all, considering the relevance and importance with respect to the cross-flow instability, Linear Stability Theory (LST) is discussed in section 3.1. The working principles of the consulted experimental methods, which are planar and stereoscopic particle image velocimetry (PIV), are discussed in section 3.2. In section 3.3, various essential data analysis methods and theories are introduced to aid in the comparison of the AC-DBD plasma actuators' authority, operation and effectiveness.

3.1. Linear Stability Theory

Linear Stability Theory (LST) is an essential tool in cross-flow instability studies due to its capability of predicting the onset of the primary modes and the related frequencies, wavelengths as well as the associated amplification and damping rates. The theory is based on the assumptions of a parallel mean flow and small disturbances. Although an introduction to LST is given below, the reader is referred to the work of Mack [49] for a more thorough description.

First, the relevant flow variables are divided into a mean-flow term and a small fluctuation or disturbance term, which are denoted by an upper-case letter and a lower-case letter respectively. Assuming an incompressible parallel flow, such that the normal velocity V is equal to zero and U and W are only a function of y, the two-dimensional linearised parallel-flow equations can be written as:

$$\frac{\partial u}{\partial x} + \frac{\partial v}{\partial y} + \frac{\partial w}{\partial z} = 0 \tag{3.1a}$$

$$\frac{\partial u}{\partial t} + U\frac{\partial u}{\partial x} + W\frac{\partial u}{\partial z} + v\frac{\partial U}{\partial y} = -\frac{\partial p}{\partial x} + \nu\nabla^2 u \tag{3.1b}$$

$$\frac{\partial v}{\partial t} + U\frac{\partial v}{\partial x} + W\frac{\partial v}{\partial z} = -\frac{\partial p}{\partial x} + \nu\nabla^2 v \tag{3.1c}$$

$$\frac{\partial w}{\partial t} + U\frac{\partial w}{\partial x} + W\frac{\partial w}{\partial z} + v\frac{\partial U}{\partial y} = -\frac{\partial p}{\partial x} + \nu\nabla^2 w \tag{3.1d}$$

The equations can be re-written in normal-mode or wave form by considering the expression:

$$[u, v, w, p]^T = [\hat{u}(y), \hat{v}(y), \hat{w}(y), \hat{p}(y)]^T \cdot e^{i(\alpha x + \beta z - \omega t)} \tag{3.2}$$

Here, α and β are the spatial stream-wise and span-wise wavenumbers corresponding to the x and z components of the wavenumber vector k, whereas ω is the frequency and the components denoted with a hat are complex functions. In the case of a boundary layer, the disturbances approach zero far away from the wall and the no-slip condition applies such that the velocity components are similarly zero at the wall. Equation 3.2 can be substituted into equation 3.1a to 3.1d to obtain a set of ordinary differential equations for the modal functions, as presented by Mack [49]. This yields a set of four equations with six real quantities; $\hat{u}$, $\hat{v}$, $\hat{w}$, $\hat{p}$, $d\hat{u}/dy$ and $d\hat{w}/dy$, as seen in equations 3.3a to 3.3d.

$$i(\alpha U + \beta W - \omega)\hat{u} + \hat{v}\frac{\partial U}{\partial y} = -i\alpha\hat{p} + \frac{1}{Re}\left[\frac{\partial^2}{\partial y} - (\alpha^2 + \beta^2)\right]\hat{u} \tag{3.3a}$$

$$i(\alpha U + \beta W - \omega)\hat{v} = -\frac{\partial \hat{p}}{\partial y} + \frac{1}{Re}\left[\frac{\partial^2}{\partial y} - (\alpha^2 + \beta^2)\right]\hat{v} \tag{3.3b}$$

$$i(\alpha U + \beta W - \omega)\hat{w} + \hat{v}\frac{\partial W}{\partial y} = -i\alpha\hat{p} + \frac{1}{Re}\left[\frac{\partial^2}{\partial y} - (\alpha^2 + \beta^2)\right]\hat{w} \tag{3.3c}$$

$$\alpha\hat{u} + \beta\hat{w} + \frac{\partial \hat{v}}{\partial y} = 0 \tag{3.3d}$$

The sixth-order system can be reduced to a fourth-order system in order to determine the eigenvalues. Through manipulation, a system of equations is obtained for the four variables $\alpha\hat{u} + \beta\hat{w}$, $\hat{v}$, $\alpha\hat{w} - \beta\hat{u}$ and $\hat{p}$. Following further elimination of terms, a single fourth-order equation can be derived, the Orr-Sommerfeld equation. The result is shown in equation 3.4 and forms the basis of most incompressible stability studies. Typically the Orr-Sommerfeld is derived from the vorticity equation, in which case the stream function ψ is used.

$$\left[\frac{\partial^2}{\partial y^2} - (\alpha^2 + \beta^2)\right]^2 \hat{v} = i\,Re\left\{(\alpha U + \beta W - \omega)\left[\frac{\partial^2}{\partial y^2} - (\alpha^2 + \beta^2)\right] - \left(\alpha\frac{\partial^2 U}{\partial y^2} + \beta\frac{\partial^2 W}{\partial y^2}\right)\right\}\hat{v} \tag{3.4}$$

The imposed conditions at the wall and far away from the wall remain, such that:

$$\hat{v}(0) = 0 \quad , \quad \frac{\partial \hat{v}}{\partial y}(0) = 0 \quad \text{and} \quad \hat{v}(y) = 0 \quad , \quad \frac{\partial \hat{v}}{\partial y}(y) = 0 \quad \text{as} \quad y \to \infty \tag{3.5}$$

For a two-dimensional boundary layer, the Orr-Sommerfeld equation can be further reduced. As W = 0 and β = 0, equation 3.6 is obtained.

$$\left[\frac{\partial^2}{\partial y^2} - \alpha^2\right]^2 \hat{v} = i\,Re\left\{(\alpha U - \omega)\left[\frac{\partial^2}{\partial y^2} - \alpha^2\right] - \alpha\frac{\partial^2 U}{\partial y^2}\right\}\hat{v} \tag{3.6}$$

As the Orr-Sommerfeld equation contains both spatial and temporal factors in α and β and ω respectively, the stability analysis can be approached in two manners. The temporal amplification theory assumes that the frequency ω is complex and of the form $\omega = \omega_r + i\omega_i$, whereas α and β are real. In the spatial amplification theory, ω is real whereas α and β are complex. These expressions for each theory can be substituted into a stream function resembling a single disturbance of the form:

$$\psi(x, y, z, t) = \psi(y)e^{i(\alpha x + \beta z - \omega t)} \tag{3.7}$$

If A then represents the amplitude of ψ at an arbitrary height y, it follows that the temporal amplification rate and spatial amplification rate can be expressed as:

$$\frac{1}{A}\frac{dA}{dt} = \omega_i \quad \text{and} \quad \frac{1}{A}\frac{dA}{dx} = -\alpha_i \tag{3.8}$$

After substitution, it is apparent that the disturbances are damped when ω_i or $-\alpha_i$ is negative and amplified when ω_i or $-\alpha_i$ is positive for the temporal and spatial amplification theory respectively. A neutral condition exists when either quantity is zero for the respective theory. A quantity that is closely related to the spatial amplification rate is the amplification factor, or the N-factor. The N-factor at a particular x-location is obtained by computing the integral of the amplification rates over the spatial domain, according to:

$$N(x) = ln\left(\frac{A(x)}{A_0(x)}\right) = \int_{x_0}^{x} -\alpha_i dx \tag{3.9}$$

As can be observed from equation 3.9, the amplitude ratio $A(x)/A_0(x)$ is equal to e^N. This expression is at the basis of the laminar-to-turbulent transition prediction method, independently introduced by Van Ingen [88] and Smith & Gamberoni [85]. For a range of frequencies, the N-factor at each x-location can be computed such that an envelope of curves is obtained. By consulting the transition location as obtained through experiments, the associated N-factors can be determined. If no such data is available prior to the experiment, a first-estimate of the 'critical' N-factor can be used to predict the transition Reynolds number. For this, Mack [48] published the following empirical equation for the critical N-factor, as a function of the absolute turbulence level:

$$N = -8.43 - 2.4\ \ln(T) \tag{3.10}$$

As discussed by Van Ingen [89], clearly the free-stream turbulence by itself is not adequate to describe the disturbance environment, and as such, it should be noted that, although the e^N-method performs rather well for two-dimensional flows featuring linear disturbances, its accuracy is limited in the case of non-linear or three-dimensional scenarios due to its linear theory.

3.2. Particle Image Velocimetry

A successful flow measurement technique that has seen a rise in popularity over the past decades is Particle Image Velocimetry, or PIV. PIV allows for the non-intrusive measurement of instantaneous velocity fields within a plane (planar PIV), and, with specific optical arrangements, this domain can be further extended to a three-dimensional volume (stereoscopic or tomographic PIV), making it an excellent tool for quantitative flow visualisation. This section briefly discusses the working principle of planar PIV, what additional arrangements are required for stereoscopic PIV and the uncertainty that is associated with the PIV measurements.

3.2.1. Working Principle

PIV is based on the illumination of tracer particles and recording these on two separate frames with a known time interval, such that through the particle displacement the velocity can be resolved at each location within the frame. A typical arrangement for planar (two-dimensional) PIV can be found in figure 3.1.

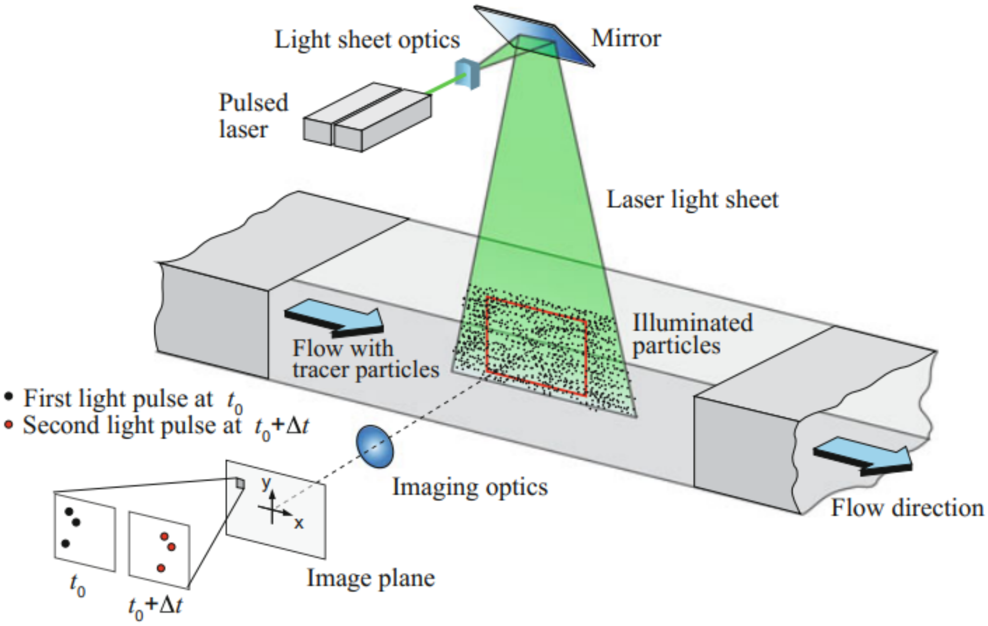

Figure 3.1: An example of a planar PIV arrangement for a wind tunnel experiment, as presented by Raffel et al. [62].

These tracer or seeding particles should not interfere with the object of interest and have a similar density as the flow they operate in such that they accurately follow the motion of the flow, where especially the former point is of interest when considering the electromagnetic field of AC-DBD plasma actuators.

The particles should be sufficiently small to achieve a high spatial resolution, but still large enough such that enough light is scattered following Mie's scattering theory. For low-speed experiments in air, water-glycol based solutions have been a common choice for creating suitable droplets featuring a diameter of approximately 1 μm.

Laser light sources are generally employed to provide the adequate illumination such that the scattered light can be detected by the digital imaging devices. As described by Raffel et al. [62], the collimated light beam along with the use of optical instruments allows for straightforward shaping into a thin laser sheet, which is required to ensure all particles are in focus. Furthermore, the duration of a laser pulse can be very short, ensuring a short exposure time such that the particles appear circular rather than streaks.

Typically the cameras used to record the images do so in either a double-frame or single frame mode. In the double-frame mode, an image pair is recorded with a time interval of dt and a specified acquisition frequency. On the other hand, in the single frame mode, the camera continuously records images with a time interval of dt and an acquisition frequency equal to 1 divided by dt. At sufficiently high acquisition frequencies and in the case of relatively low velocities, PIV can be used to achieve a very high temporal resolution; a technique known as time-resolved PIV. This technique also requires the use of a laser with a high repetition rate (typically of the Nd:YLF-type) to maintain adequate image quality.

Once all images have been recorded, in order to obtain the velocity at each location in the measurement plane, the images must first be processed to aid the cross-correlation procedure. This step usually involves a background intensity removal through a combination of several minimum intensity subtraction operations. Once most reflections and background noise are eliminated, the image is divided into interrogation windows. The intensities of each interrogation window are evaluated for two consecutive frames with a cross-correlation operator. The outcome of this process is a correlation peak for each interrogation window, indicating the displacement of the particles for that particular region. Considering the time interval between the two consecutive images is known and the scaling in terms of pixels per millimeter can be obtained through imaging a simple calibration target, the velocity of the flow at each point in the measurement domain can be retrieved.

The size of the interrogation window is of great importance in relation to the resulting flow field. For too small interrogation windows, particles in the first frame will possibly have departed the interrogation window in the second frame and similarly, particles that were not present in the first frame might have entered the window in the second frame, hindering proper cross-correlation. A solution to this issue would be to decrease the time interval, such that the particle displacements are lowered, however this method harms the signal to noise ratio, as discussed by Serpieri [80]. Instead, multi-pass cross-correlation methods are used, as presented by Scarano [73]. Starting from a large window, an initial estimation of the displacement is made, after which the cross-correlation is performed on smaller windows via multiple passes.

3.2.2. Stereo Particle Image Velocimetry

Whereas planar PIV allows for the measurement of two velocity components in a two-dimensional domain, stereoscopic or stereo-PIV employs one additional camera in order to resolve the third velocity component; the out-of-plane component. When considering the flow over a swept wing, which is highly three-dimensional, stereo-PIV proves to be an excellent technique to simultaneously measure not only the stream-wise velocity, but also the span-wise, out-of-plane velocity component. An example of a stereoscopic PIV set-up featuring two cameras can be found in figure 3.2.

Although the working principle of stereo-PIV is similar to planar PIV, there are distinct differences in terms of the experimental set-up and the image processing. Considering the cameras are positioned at an angle with respect to the laser sheet, the distance from the field of view to the camera is no longer uniform over the image, as would be the case for planar PIV. This variation in distance along the image leads to particles that are in focus only in a specific region of the image. To ensure the full image is in focus, a Scheimpflug mount has to be used to fulfill the Scheimpflug criterion. This mount tilts the image plane such that it coincides with the lens and object plane, ensuring the complete image is in focus, as discussed by Hinsch [27].

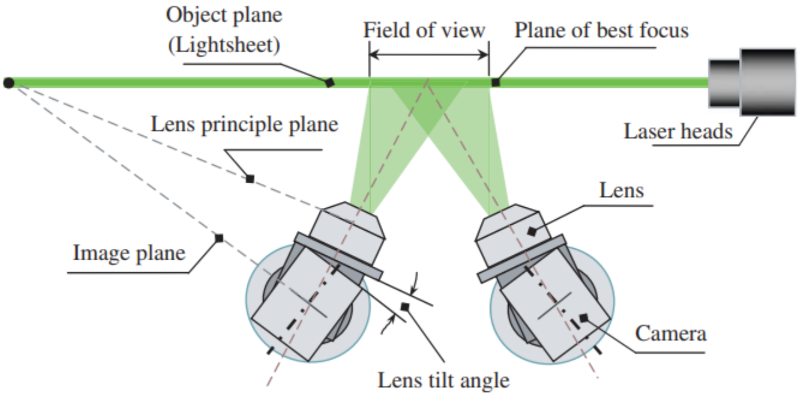

Figure 3.2: Example of an optical arrangement for stereoscopic PIV, showing the necessity of the Scheimpflug mount in order to ensure a fully focused image. As from Liu et al. [45].

In order to perform a calibration for a stereo-PIV set-up, a double-sided calibration target is required. This calibration target features a precise grid of markers, such as dots or lines, from which the mapping between the image space and the object space can be calculated. Due to camera vibrations or small shifts in the location of the laser sheet, as described by Raffel et al. [62], it is unlikely that the laser light sheet corresponds perfectly to the axis of the calibration target and as such, a disparity correction or self-calibration is required. This self-calibration relies on the cross-correlation of the actual particle images, such that a displacement field is found that represents the disparity between both camera views. This disparity field can then be used to correct the initial mapping coefficients that were calculated from the calibration target, such that a more representative calibration is obtained. Due to the finite thickness of the laser sheet, it is impossible to acquire a perfect match of particles in both views. It is for this reason that the cross-correlation peaks of the self-calibration have a distinct elongated shape rather than a circular shape, as would be the case for two-dimensional, two components (2D2C) PIV data.

3.2.3. Uncertainty Quantification & Error Propagation

Although the stereo-PIV self-calibration process described above aims to reduce the error in the measurement, an inherent uncertainty invariably remains present in the results when using PIV and the associated methods and instruments. The quantification of the uncertainty regarding PIV measurements is non-trivial due to the considerable amount of measurement and experimental parameters. The most relevant sources of uncertainty are presented here, along with the measures that are taken in this report to include the certainty in the analysis.

Particle Image Velocimetry Error Sources

Due to the great variation in experimental studies, equipment and environment, there is no universal value for the PIV uncertainty, although the value of 0.1 pixels is often mentioned [78]. In general, a distinction is made between systematic uncertainties, which stem from, for example, perspective or calibration errors, and random uncertainties, which can be quantified through various methods and include for example, illumination and seeding density. Raffel et al. [62] note that these PIV errors are generally introduced in the experimental set-up, by the flow itself or in the post-processing of the data. These three error sources are briefly discussed below.

In the case of the former, systematic errors can be introduced through improper installation and alignment. Clearly, when the light sheet is not properly aligned with the flow direction, the measured velocities differ from the velocities of interest. Discrepancies in the calibration target and misalignment of the calibration target with respect to the measurement plane can lead to further systematic errors, although in the case of stereoscopic PIV these can be reduced through self-calibration techniques, as mentioned by Raffel et al. [62]. Next to these misalignment and positioning errors, errors can be attributed to the measurement instruments, the illumination and the particle characteristics, as discussed by Sciacchitano [78]. A discrepancy in the selected laser pulse delay and the actual pulse delay has a significant effect on the measured velocity, which is directly related to the particle displacement and the time step. Furthermore, a misalignment of the laser pulses or a difference in laser intensity (profile) can lead to a disparity in intensity for the seeding particles in consecutive frames, leading to an error in the cross-correlation process, as described by Sciacchitano [78].

The flow itself can be the source of various measurement errors. As discussed by Sciacchitano [78], the image post-processing algorithm may be unable to resolve strong streamline curvatures, velocity fluctuations and gradients. Other measurement errors can be attributed to changes in the fluid properties, such as the temperature or density, throughout the measurement campaigns. In case out-of-plane velocity gradients are present, the associated particles can enter the in-plane domain and cloud the correlation process by their random locations. When these particles are smaller than the pixel size, the velocity is either overestimated or underestimated; an error known as peak-locking.

Even under perfect and ideal conditions, where there are no errors in the experimental set-up and the associated instruments, the obtained data has to be processed such that the velocity fields of interest are obtained. It is this evaluation in which additional errors are introduced. As discussed by Sciacchitano [78], a significant amount of research has been conducted in order to mitigate this error. These efforts ranged from adjusting the interrogation windows and shapes as well as optimising the algorithms related to finding the cross-correlation peak.

For a more complete study on PIV error sources and quantification, the reader is referred to the articles by amongst others, Sciacchitano [79] and Raffel et al. [62].

Particle Image Velocimetry Uncertainty Quantification

It should be clear that (measurement) errors are introduced at each step of the experiment. Prior to the experiment, particular care should be taken in terms of amongst others, the alignment of the laser, the measurement plane and the calibration target as to limit the systematic errors. Whereas it is assumed that these systematic errors cannot be quantified from the resulting PIV images, the random measurement errors yield different results for each measurement, such that an uncertainty can be defined through a statistical approach. The approach that is taken in this report regarding the PIV uncertainty and the related error propagation is briefly discussed here.

During this research, the main parameter of interest is the velocity. As discussed by Sciacchitano & Wieneke [79], assuming the samples are independent and the standard deviation σ_x follows a normal distribution, the time-averaged uncertainty for the mean and the standard deviation can be expressed as:

$$U_{\bar{x}} = \frac{\sigma_x}{\sqrt{N}} \quad , \quad U_{\sigma_x} = \frac{\sigma_x}{\sqrt{2(N-1)}} \tag{3.11}$$

The expression for the uncertainty of the mean velocity can be used to compute the uncertainty at each location in the measurement domain. When parameters of interest follow from the mean velocity field, such as the thrust, as will be described in the following section, the resulting vector field containing the uncertainties is added and subtracted from the mean velocity field to obtain an uncertainty band. This uncertainty band indicates a range in which the true value exists with a probability of one standard deviation.

3.3. Data Analysis Techniques

In this section various methods and theories are introduced that are directly and indirectly related to the characterisation of the AC-DBD plasma actuators. The characterisation of plasma actuators in quiescent conditions allows for a proper comparison between the performance of various actuator configurations and operating conditions. Such a characterisation generally covers the electrical, thermal and mechanical effects. As measured through Hot- and Cold Wire Anemometry (HWA, CWA) by Jukes et al. [33], the temperature increase near the respective AC-DBD actuator due to the plasma has a limited effect on the induced velocity, in contrast with ns-DBD plasma actuators. The theory and methods employed for the electrical and mechanical characterisation are discussed in the following sections.

3.3.1. Electrical Characterisation

The main parameter of interest in relation to the electrical characterisation is the power consumption. The power consumption allows for a fair comparison between different actuator designs and operating conditions as well as a cost-benefit analysis, as described by Ashpis et al. [3]. However, the electrical characterisation of plasma actuators is complicated by the unsteady plasma formation featuring short periods of milliseconds and high frequency current discharges taking place on an even smaller timescale. Despite this, in his review paper, Kotsonis [39] presents an overview of literature featuring various methods that have been employed to obtain the voltage, current and power of AC-DBD plasma actuators.

The output voltage is often readily available from the power supply or high voltage amplifier and can be read from the associated data acquisition unit (DAQ) or through an oscilloscope. Ashpis et al. [3] note that the performance of the actuators is affected by the impedance of the circuit and thus particular attention must paid with regards to the length of high-voltage cables and other components.

Ashpis et al. [3] propose various methods in order to measure the power consumption of AC-DBD plasma actuators. One of these methods is based on the electrical charge, which is employed in this research. When a capacitor with capacitance C_m is mounted in between the buried electrode and the ground connection (in series), the instantaneous charge is equal to:

$$Q_m(t) = C_m \cdot V_m(t) \tag{3.12}$$

Following this expression, the current through the capacitor is then equal to:

$$I(t) = C_m \frac{dV_m(t)}{dt} \tag{3.13}$$

In these equations, C_m is equal to the capacitance, V_m is the voltage that is measured over the capacitor and Q_m is the accumulated charge over the capacitor. Knowing that the actuator and capacitor are positioned in series, the current must be equal and thus the instantaneous power consumption for the actuator can be expressed as:

$$P_a(t) = V_a(t) \cdot I_a(t) = V_a(t) \cdot C_m \frac{dV_m(t)}{dt} \tag{3.14}$$

The average power consumption per cycle with period T can then be derived and is equal to:

$$\overline{P}_a = \frac{1}{T} \int_0^T V_a(t) \cdot C_m \frac{dV_m(t)}{dt} = \frac{1}{T} \int V_a \cdot C_m dV_m = \frac{1}{T} \oint V_a dQ_m \tag{3.15}$$

From the final expression, it can be observed that the average power consumption must be equal to the area that is encapsulated by a V_a-Q_m curve divided by the period of the signal, as presented by Kotsonis [39] and Ashpis et al. [3]. This curve is better known as a Lissajous curve and an example is presented in figure 3.3.

3.3.2. Mechanical Characterisation

As discussed in chapter 2, the primary function of the AC-DBD plasma actuator is to induce a velocity to the adjacent flow by the formation of plasma. The term mechanical characterisation is used here to quantify this aerodynamic effect. In order to eliminate any external effects that can influence the characterisation, such as hydrodynamic or pressure influences, the mechanical characterisation is conducted in quiescent conditions. This allows for a proper comparison between various operating conditions and actuator geometries.

In his review paper, Kotsonis [39] presents an overview of literature in which various methods are described to measure the induced velocity. These methods range from straightforward Pitot tube measurements to the more complex HWA, PIV, Schlieren and Laser Doppler Velocimetry (LDV) techniques. In contrast with the other techniques, PIV allows for a complete instantaneous quantitative description of the flow field in the vicinity of the actuator. Furthermore, the non-intrusive nature of PIV limits any undesirable interaction between the measurement system and the plasma actuator, as is the case for

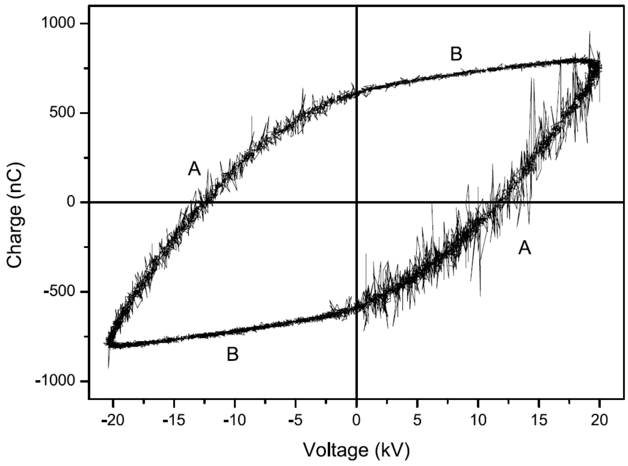

Figure 3.3: Lissajous curve, clearly showing the high-frequency discharges in the lower-right quadrant, which corresponds to the positive half-cycle of the respective input signal. As from Pons et al. [59].

HWA. Electromagnetic interference (EMI) and electrical arcing have been encountered in various studies, including the study performed by Jukes et al. [33], and therefore restricts the applicability of HWA in most scenarios.

Although the instantaneous and mean velocity field can be obtained through the processing of the PIV images, the spatial distribution of the body force that is responsible for the flow control authority of AC-DBD plasma actuators has also received significant attention. Various methods and assumptions have been employed to accurately resolve the full spatio-temporal evolution of the body force, including those of Wilke [94] and Benard et al. [6], which are based on phase-averaged LDV measurements and phase-averaged PIV measurements respectively. For this research, the approach described by Kotsonis et al. [40] is consulted.

Body Force Computation

The two techniques proposed by Kotsonis et al. [40] rely on images obtained by high-speed time-resolved particle image velocimetry as an input. As discussed in chapter 2, the two-dimensional incompressible Navier-Stokes equations can be written as:

$$\frac{\partial U}{\partial t} + U \cdot \nabla U - \nu \nabla^2 U = -\frac{\nabla p}{\rho} + \frac{F}{\rho} \tag{3.16}$$

In this equation, U is the two-dimensional velocity field obtained from the time-resolved PIV, p is the static pressure, ν is the kinematic viscosity of the respective medium and ρ is the corresponding density. When considering the initial moments after the activation of the plasma actuator, it is assumed that the acceleration is dominating in comparison to the other terms in the equation. This assumption results in the following expression:

$$\frac{\partial U}{\partial t} = \frac{F}{\rho} \tag{3.17}$$

This simple method effectively represents Newton's second law, where the force is linearly related to the acceleration. Kotsonis et al. [40] refer to this method as the reduced method, in contrast with the gradient method.

The gradient method makes use of the full two-dimensional Navier-Stokes equations, although two major assumptions are introduced. First of all, it is assumed that the body force is (quasi-) steady in time and secondly, the pressure gradient is assumed to be zero up until the point of actuation. Although it is known that the plasma generation (and therefore the body force) is asymmetric for a single cycle, the first assumption is justified by considering the high frequency at which the actuator operates in combination with the relatively high inertia or low response time of the flow. With these assumptions, the two-dimensional Navier-Stokes equations can be differentiated in time to eliminate the body force term:

$$\frac{\partial^2 U}{\partial t^2} + \frac{\partial (U \cdot \nabla U)}{\partial t} - \nu \frac{\partial (\nabla^2 U)}{\partial t} = -\frac{\partial (\nabla p)}{\partial t} \tag{3.18}$$

As all terms on the left-hand side can be obtained from the instantaneous velocity field, the only remaining unknown is the derivative of the pressure gradient. By integrating back in time and considering the second assumption, which states that the pressure is zero prior to the actuation, the pressure gradient can be obtained according to the following expression:

$$\int_0^t \left(\frac{\partial^2 U}{\partial t^2} + \frac{\partial (U \cdot \nabla U)}{\partial t} - \nu \frac{\partial (\nabla^2 U)}{\partial t} \right) dt = -(\nabla p) + \text{Constant} \tag{3.19}$$

This integration constant is set to zero for $t = 0$ and as such, the pressure gradient can be calculated and substituted into equation 3.16, leaving the body force as the only unknown.

As discussed by Kotsonis et al. [40], the gradient method features a higher level of accuracy due to the inclusion of more Navier-Stokes terms. Furthermore, the reduced method is more sensitive to the chosen time interval beyond actuation for which the acceleration at $t = 0$ is calculated. However, as the velocity and pressure terms at $t = 0$ are small in comparison to the acceleration, the discrepancy between both methods is considered to be present but limited.

Thrust Computation

The thrust can be directly obtained by integrating the body force over the respective spatial domain. By doing so, the information on the spatial distribution of the body force is lost and instead a scalar value is obtained. Such a value could be of interest for a straightforward quantitative comparison regarding the performance of various actuator configurations and operating conditions. However, as the actuator develops a strong wall jet, particular care must be exercised as to what exactly is being measured or calculated. Load cells that operate based on the principle of Newton's third law typically measure a combination of the thrust exerted by the actuator plus the shear forces at the wall. The same holds for the control volume method as presented by Hoskinson et al. [28] that is introduced here.

The method considers a control volume that is placed in the vicinity of the plasma actuator, as shown in figure 3.4.

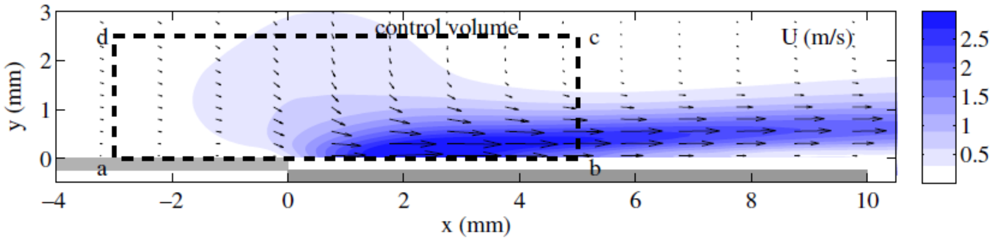

Figure 3.4: Example of a time-averaged velocity field induced by an AC-DBD plasma actuator. The control volume used for the thrust calculation is shown by the dashed line. As from Kotsonis et al. [40].

For this particular control volume, the expression for the momentum balance is equal to:

$$T = \oint_{abcd} (\rho U \cdot dS)\, U + \oint_{abcd} p dS \tag{3.20}$$

In this equation, T is the total force exerted on the flow, which therefore includes the contribution of the actuator as well as the shear force. An assumption has to be made for the pressure, as the value cannot be readily obtained from the velocity field, as also discussed in the previous section. As introduced by Hoskinson et al. [28] and Kotsonis et al. [40], it is assumed that the pressure is uniform and equal within the control volume, provided that the boundaries are located sufficiently far away from the region of the body force. With these assumptions, the expressions for the thrust in both x- and y-direction can be written as:

$$T_{x,plasma} + T_{x,shear} = \rho \int_{da} u_x^2 dy + \rho \int_{cd} u_x u_y dx - \rho \int_{bc} u_x^2 dy \tag{3.21}$$

$$T_y = \rho \int_{da} u_x u_y dy + \rho \int_{cd} u_y^2 dx - \rho \int_{bc} u_x u_y dy \tag{3.22}$$

It should be reiterated that the thrust obtained from integrating the body force over the spatial domain inherently differs from the thrust calculated through the control volume method. The thrust obtained by the body force represents the component that is directly exerted by the actuator, whereas the thrust obtained via the momentum balance method consists of the two components that have been formed as a reaction to this body force; specifically the induced velocity and shear force. Nevertheless, the momentum balance method operates directly on the measured average velocity field, whereas the calculation of the body force through the gradient or reduced method requires requires further manipulation of the data in terms of spatial and temporal filters, as well as a proper selection of the time interval. These additional operations increase the uncertainty, such that the thrust obtained through the momentum balance method is a more reliable criterion.

3.3.3. Cross-Flow Instability Metrics

In order to quantify the effect of the AC-DBD plasma actuator on the cross-flow instability, various methods exist in order to quantify the amplitude and modal growth of the stationary cross-flow vortices. Two commonly accepted methods are described here.

Both methods rely on the computation of the mode shape profile. This disturbance profile is obtained by computing the span-wise standard deviation of the mean velocity field. Once a single profile is obtained per chord station, the amplitude growth of the stationary cross-flow vortex can be computed. This can be done by tracking the maxima, as proposed by Haynes & Reed [26], according to:

$$A_I(x) = \text{max}\,|_y \left(\text{std}\left(\frac{w(x)}{U_e(x)} \right) \right) \tag{3.23}$$

Here, A_I is the non-dimensionalised amplitude, y is the height at which the maximum is located, w is span-wise velocity component and U_e is the local external velocity. Alternatively, the wall-normal integral of the mode shape profile can be computed. This method accounts for the increase of the boundary layer in wall-normal direction, as described by Downs & White [14] and can be calculated according to:

$$A_I(x) = \frac{1}{y_{99}} \int_0^{y_{99}} \left(\text{std}\left(\frac{w(x)}{U_e(x)} \right) \right) dy \tag{3.24}$$

, where y_{99} is the boundary layer edge. It should be noted that both methods are rather similar and should therefore yield a similar trend.

3.3.4. Power Spectral Density

As elaborated in chapter 2, the cross-flow instability is highly receptive to surface roughness and turbulence intensity. Small disturbances can enter the boundary layer through the process of receptivity and influence the evolution of the primary and secondary instabilities. For this reason, it is essential to investigate the frequencies that are introduced into the flow field by the actuator, as the introduction of frequencies in the frequency band of these respective instabilities can accelerate the path towards transition.

With the use of a Fourier transform, the time (or space) signal can be transformed to the frequency (or wavelength) domain. The power spectral density (PSD) gives insight in how the power is distributed over the frequency (or wavelength) spectrum as well as the spatial domain. Typically the temporal evolution of the fluctuating velocity field is used as an input for such studies related to aerodynamics. If the signal is assumed to have the form $x(t)$, then the average power of one period is simply:

$$P = \lim_{T\to\infty} \frac{1}{T} \int_{-\infty}^{\infty} |x(t)|^2 dt \tag{3.25}$$

Employing Parseval's theorem and rewriting the average power in the frequency domain, where the Fourier transform is expressed as $\hat{x}(f)$, yields:

$$P = \lim_{T\to\infty} \frac{1}{T} \int_{-\infty}^{\infty} |\hat{x}(f)|^2 df \tag{3.26}$$

The spectral density is then simply found by integrating the expression, such that:

$$S_{xx} = \frac{1}{T} |\hat{x}(f)|^2 \tag{3.27}$$

A popular method for calculating the power spectral density using the fast Fourier transform has been proposed by Welch [91] in 1967. Welch's method initially splits the signal into overlapping segments, which are then multiplied by a window function, usually in the form of a Hamming window. For each segment, a modified periodogram is computed and averaged such that an estimation of the complete power spectral density is obtained.

4

Experimental Setup

This chapter presents the various setups that are used for the electrical and mechanical characterisation as well as for the wind tunnel experiments. All tests are performed using facilities in the Low Speed Laboratory at the Delft University of Technology.

4.1. Plasma Actuator Design

As a requirement, the AC-DBD plasma actuator design that is used throughout the research must be capable of inducing a span-wise uniform plasma discharge. In their study featuring AC-DBD plasma actuators used for swept-wing laminar-to-turbulent transition control, Yadala et al. [95] employed a novel ink-jet printing technique that was developed in-house, which involves spraying conductive silver particles to produce electrodes with a thickness in the order of several micrometers. As it is known that the cross-flow instability is extremely sensitive to surface roughness, following the research by, amongst others, Saric et al. [72], the minimum thickness electrodes provide a significant advantage over more traditional (adhesive copper tape) actuators, which typically have a thickness in the order of 60 μm. Following the success and simplicity of this method, it is adopted as the main technique for creating the AC-DBD plasma actuators. The printer itself is presented in figure 4.1.

The electrodes are printed on NB-TP-3GU100 transparent PET sheets, which feature a micro-porous coating to ensure the mixture of conductive silver particles rapidly dries. The silver nano-particle ink as well as the specially designed subtrates are obtained from Mitsubishi Paper Mills Ltd. Following the efforts of Yadala et al. [95] and Serpieri & Kotsonis [83] in similar studies, the silver ground and high-voltage electrodes have a width of w = 5 mm and the electrodes have no overlap. The two sheets with the respective ground and high-voltage electrode are separated by a dielectric layer of PET-G. All three components are bonded together with spray glue. PET-G is chosen for its excellent dielectric properties and its transparent nature allows for a straightforward validation of the alignment of the electrodes. As high voltages (and frequencies) are required for the plasma actuators to be effective in its capability of base-flow modification, an initial dielectric thickness of 1 mm is chosen.

Component	Material	Thickness	Length	Width
High-Voltage Electrode	Printed silver coating	<10 μm	160 mm	5 mm
Ground Electrode	Printed silver coating	<10 μm	160 mm	5 mm
Dielectric	PET-G	1 mm	-	-
Adhesive	Spray Glue	<10 μm	-	-
Printing Sheet	Transparent PET	135 μm	-	-

Table 4.1: AC-DBD plasma actuator configuration for the electrical characterisation experiment.

A larger dielectric thickness effectively increases the limit at which electrical breakdown occurs, allowing for the application of higher voltages, as discussed by Benard & Moreau [5]. The total thickness of the considered plasma actuator is measured to be approximately 1.28 mm, where the thicknesses of the individual components can be found in table 4.1.

An example of the resulting electrode configuration can be seen in figure 4.1. The sheets are of A4-format and the silver electrodes (in black) are purposefully placed at a 45° angle such that minimal changes are required once the actuators are placed on the swept wing model in future wind tunnel experiments. A thin 45 ° diagonal line is introduced for alignment purposes, while also guiding as the indicator of the leading edge of the wing.

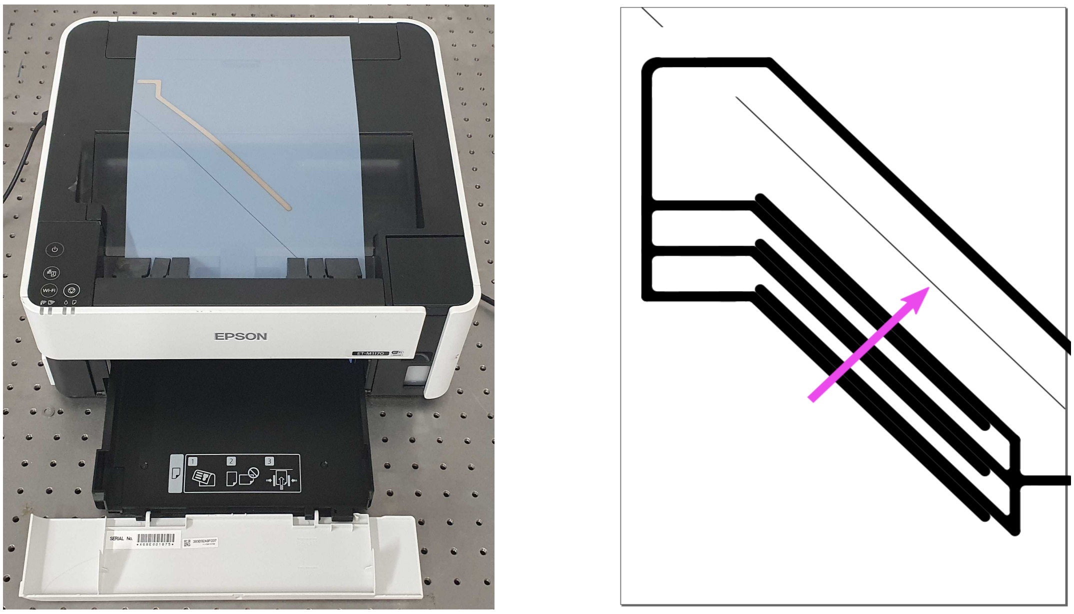
(a) (b)

Figure 4.1: Printer that is used to print the silver electrodes on the designated sheets, with an example sheet visible featuring the ground electrode on top of the printer (a) and an example of a complete AC-DBD plasma actuator sheet featuring three consecutive electrode pairs (b). Two paths exit the page on the right, with the high-voltage connection being the upper electrode and the ground connection being the lower electrode. The purple arrow indicates the direction in which the plasma is formed.

4.2. Electrical Characterisation

Following the completion of the design of the actuator, a sensitivity analysis is performed on various parameters to assess their influence on the operation and, in particular, the power consumption of the plasma actuator. These parameters include the number of actuators, the spacing (gap) between the electrodes of these actuators and the thickness of the dielectric material. The definition of this spacing as well as how such a multitude of actuators operate is sketched in figure 4.2. Measurements are performed at various frequency and voltage combinations to obtain insight in the power consumption for each change in the respective parameter.

The electrical characterisation of the actuators is done through the shunt capacitor method, as discussed in section 3.3. The exposed electrode is connected to a Trek 20/20C-HS high-voltage amplifier (20 kV_{pp}, 20 mA) through copper tape, while the covered electrode is grounded. Depending on the combination of voltage and frequency, a capacitor of either 0.039 or 0.22 μF is placed in between the buried electrode and the ground connection in order to maintain an adequate resolution for the measured voltage over the capacitor. The actuator is operated via a computer, where the input signal is generated in LabView and a Digital/Analog (D/A) converter is used to send the signal to the high-voltage amplifier. The voltage, current and capacitor voltage can be readily obtained from the amplifier. Throughout this research, the actuators are consistently operated at the carrier frequency and thus no modulation frequencies or duty cycles are specified. Each measurement features 300000 samples, which is equal to a measurement time of 3 seconds considering the 100 kHz acquisition frequency.

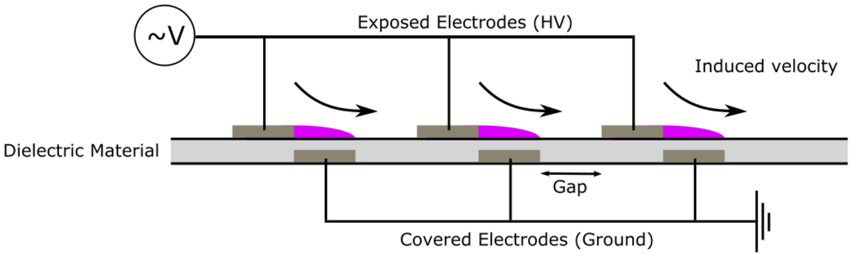
~V
Exposed Electrodes (HV)
Induced velocity
Dielectric Material
Gap
Covered Electrodes (Ground)

Figure 4.2: Sketch of three consecutive actuators and their method of operation; the flow is continuously accelerated over the electrodes.

4.3. Mechanical Characterisation

Although the electrical characterisation of the various plasma actuator configurations yields information on the power consumption of each actuator, the power consumption is not a direct indicator of the effectiveness of the actuator in inducing a velocity. As shown by Benard & Moreau [5], there is an asymptotic relationship between the maximum electric wind velocity and the power consumption, indicating that a significantly larger power consumption does not always lead to a corresponding increase in induced velocity. It is for this reason that a mechanical characterisation is performed. The working principle of high-speed, time-resolved planar PIV has been briefly described in section 3.2 and its set-up is discussed here.

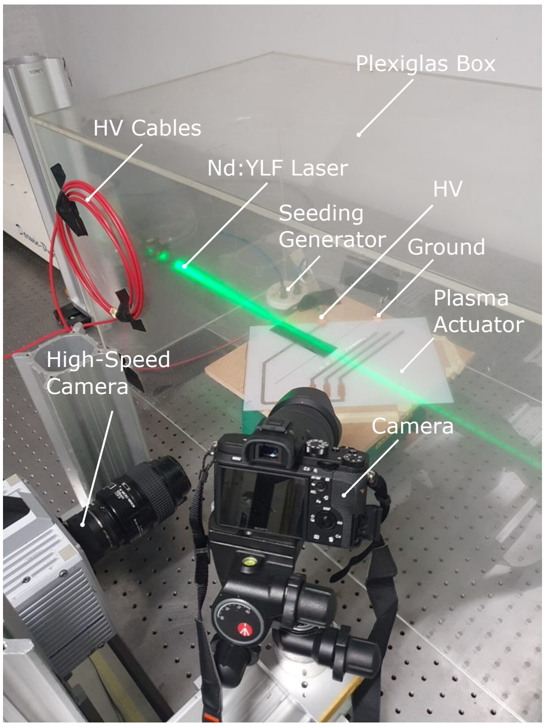
Plexiglas Box
HV Cables
Nd:YLF Laser
HV
Seeding Generator
Ground
Plasma Actuator
High-Speed Camera
Camera

Figure 4.3: Experimental set-up for the mechanical characterisation experiment, as conducted in a Plexiglas box.

To limit the influence of pressure or other hydrodynamic related effects, the characterisation is performed in quiescent conditions by placing the actuators inside a large Plexiglas box. For the measurements regarding a single actuator, a Photron Fastcam SA1.1 high-speed camera is fitted with a Nikon Micro Nikkor 200 mm lens and three consecutive extension tubes of 36 mm, 36 mm and 20 mm to ensure an in-focus field of view (FOV) of approximately 11 x 3 mm^2. The lens is set to an f-stop of 8. By vertically cropping the full sensor size from 1024 x 1024 pixels to 1024 x 288 pixels, an acquisition rate of 10 kHz can be achieved in double-frame mode. An image time separation of 50 μs is chosen, such that the second image of the first pair can be cross-correlated to the first image of the second pair, effectively doubling the acquisition frequency to 20 kHz. Additionally, a DSLR camera is positioned to record videos and images for promotional purposes. The seeding or tracer particles of approximately 1 μm are generated by a TSI Atomizer using paraffin oil (Shell Ondina). In order to generate a laser sheet of approximately 1 mm thickness, the high repetition rate Quantronix Darwin-Duo Nd:YLF laser system is employed. The laser sheet is oriented perpendicular to the electrodes at approximately half-span. Only a single plane is considered, as, following from the span-wise unvarying geometry, it is assumed that the behaviour of the actuator is uniform over its length. The Quantronix Darwin-Duo is capable of delivering an average power of 80 W at 3 kHz at a wavelength of 527 nm. The camera and laser are operated through the DaVis 10.1 software and by making use of a LaVision Programmable Timing Unit (PTU). In the case of multiple actuators, in order to ensure all electrodes and their effect on the flow are imaged, different optical instruments and settings are used, which can be found in table 4.2. A photo of the experimental setup can be found in figure 4.3.

Parameter	Single Actuator	Multiple Actuators
Lens	Nikon Micro Nikkor 200 mm	Nikon Nikkor 105 mm
Field of View (FOV)	11.08 x 3.12 mm	62.5 x 17.58 mm
Sensor Size	1024 x 288 px	1024 x 288 px
$f_{\#}$	8	5.6
Acquisition Method	Double Frame	Single Frame
Acquisition Rate	10 kHz	5.4 kHz
Image separation time	50 μs	0 μs
Samples acquired	9701	19403

Table 4.2: Camera settings for the AC-DBD plasma actuator mechanical characterisation PIV experiment.

Two distinct experiments are performed for the mechanical characterisation, which are summarised in table 4.3. These experiments have been constructed following the results of the electrical characterisation, which are presented in the following chapter. Experiment 1a considers a single actuator for which a voltage and frequency sweep are performed with the Trek 20/20C-HS high-voltage amplifier. This experiment is then repeated (experiment 1b), although a time delay is now introduced on the actuation of the plasma actuator. Doing so allows for the numerical determination of the body force, which requires the moment of actuation to be captured, such that the instantaneous acceleration can be calculated. The final experiment, experiment 2, involves the measurement of three consecutive actuators with gaps varying from 5 to 7 mm.

Experiment	Spacing	Voltage	Frequency
1a	-	12-14 kV_{pp} (steps of 1 kV)	5 kHz
1a	-	15 kV_{pp}	1-5 kHz (steps of 1 kHz)
1b	-	12-14 kV_{pp} (steps of 1 kV)	5 kHz
1b	-	15 kV_{pp}	1-5 kHz (steps of 1 kHz)
2	5, 6, 7 mm	8, 10, 12 kV_{pp}	5 kHz

Table 4.3: Test matrix for the AC-DBD plasma actuator mechanical characterisation PIV experiment.

4.4. Base-Flow Modification Wind Tunnel Experiment

The first of two wind tunnel experiments focuses on the interaction of the AC-DBD plasma actuator with the base flow over a swept wing. Of particular importance are the stream-wise and span-wise velocity profiles in the vicinity of the plasma actuator and how they respond to the induced body force exerted by the actuator. As such, stereoscopic PIV is employed to simultaneously measure all three velocity components. The working principle of stereoscopic PIV has been briefly discussed in chapter 3.

4.4.1. Wind Tunnel Facility and Wing Model

The experiment is conducted in the anechoic vertical tunnel (A-tunnel) at the Delft University of Technology. The high contraction ratio enables testing at turbulence intensities of lower than 0.10%, which is of particular importance when considering the sensitivity of the receptivity process as well as the cross-flow instability. The 0.60 m diameter circular wind tunnel duct allows for the placement of various test sections and geometries.

The wing model used in this experiment is based on the '66018M3J' (or M3J) 45° swept wing model, which was purposefully designed by Serpieri & Kotsonis [81] to be installed in the Delft University of Technology LTT facility to perform cross-flow instability studies. The M3J is a modified version of the NACA 66-018 airfoil and features a small leading edge radius and an extended region of favourable pressure gradient. The model used throughout this experiment has a pressure coefficient distribution that mimics the C_p distribution of the leading edge region of the M3J, allowing for detailed plasma actuator, cross-flow instability and receptivity studies. The shape of the airfoil (red) used throughout this research is presented in figure 4.4, along with the airfoil of the M3J for comparison.

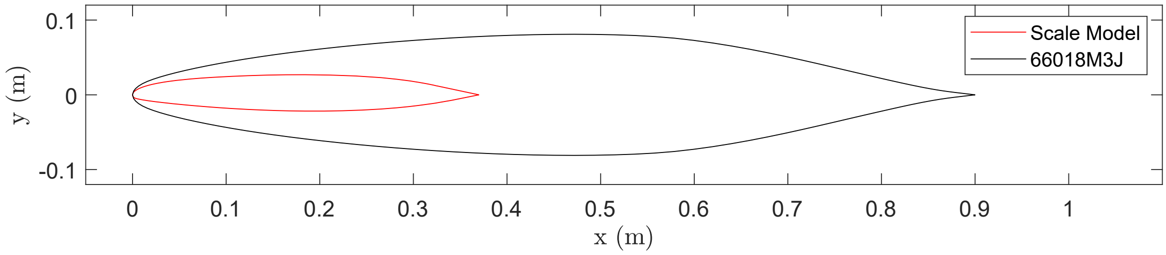

Figure 4.4: Airfoil of the wing used throughout this research (red) and the M3J (black).

The suction surface of the wing is made of aluminium, whereas the pressure surface featuring the HV and ground connections is made of Polyoxymethylene (POM) to avoid electrical interference and arcing. The model has a sweep angle of 45 degrees, a width of 980 mm and the chord length measured perpendicular to the leading edge is 370 mm. A distinct difference with the M3J wing is that this miniature model features a wide stream-wise recess of 3.1 mm deep on both the upper and lower surface in which the plasma actuator and dielectric material can be placed. The recess starts from approximately 3% of the chord. Two stream-wise array of static pressure taps are present on the left and right of the stream-wise recess, spanning from approximately 10% to 80% of the wing chord. For a more detailed description of the wing, the reader is referred to the conference article by Peng et al. [57].

4.4.2. Experimental Set-up

In this experiment, a rectangular test section of 400 x 700 mm is fitted to the wind tunnel duct, after which the wing model and its structure in which it is mounted are placed flush to the test section. The 3.1 mm recess is filled with sheets of PET-G up to a height of 2 mm, after which the sheet containing the ground electrode and the dielectric material (PET-G) of 1 mm thickness are placed. Finally, the sheet containing the HV electrode is placed on top and wraps over the leading edge to maintain the intended leading edge shape and airfoil profile. The upstream edge of the covered electrode in each plasma actuator configuration is located at $X/c_X \approx 0.06$, where c_X is the chord of the wing in stream-wise direction. The exposed sheets are painted black to mitigate any reflections caused by the laser. The electrodes are connected to the HV and ground connections on the wing by copper tape. Zig-zag strips are placed on both surfaces to trigger flow transition as to avoid unsteady phenomena. A Pitot tube is installed at the edge of the test section to measure the instantaneous free-stream velocity. A schematic of the stereoscopiv PIV set-up can be found in figure 4.5a. The two cameras are positioned such that the angle between the two devices is approximately 30°, as is advised by LaVision in their documentation on stereoscopiv PIV.

One coordinate system is visualised in figure 4.5a; the wind tunnel coordinate system, which is denoted by the upper case letters XYZ, where X is directed in the stream-wise direction, Z is the span-wise direction and Y is orthogonal to the (X, Z)-plane. As the laser sheet is oriented perpendicular to the

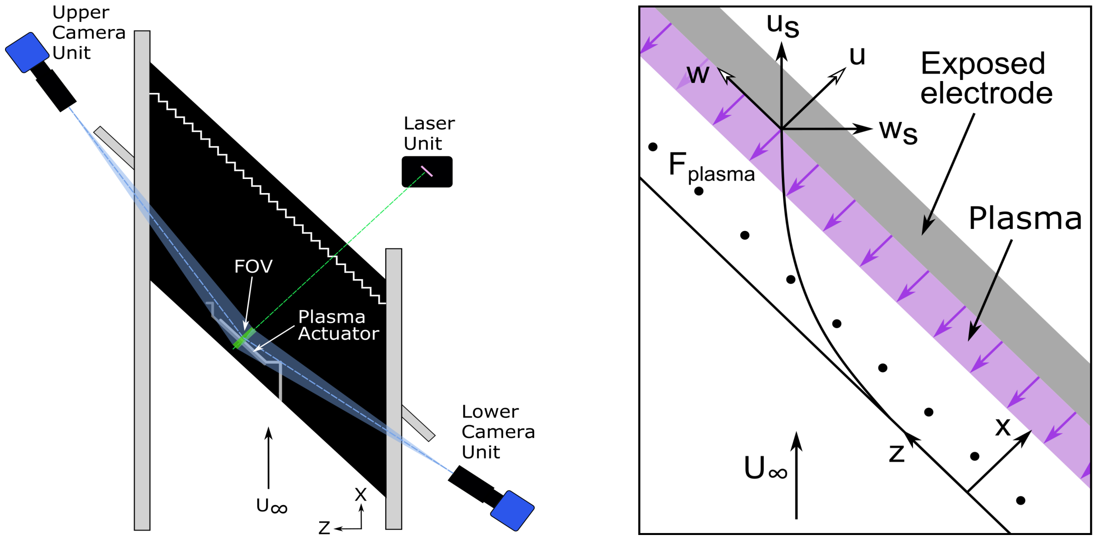

(a) (b)

Figure 4.5: (a) Schematic of the test set-up and (b) sketch of the wing leading-edge region, as seen when rotated clock-wise by 90° (not to scale). Although not used in this experiment, DREs (•) are included in relation to the subsequent wind tunnel experiment.

leading edge, a second coordinate system is introduced, which is denoted by the lower case letters xyz. Here, the x-axis is in the direction perpendicular to the wing leading edge, the z-axis is parallel to the leading edge and the positive y-axis is again normal to the (X, Z)-plane, pointing away from the wall. This coordinate system is shown in figure 4.5b, which includes a schematic of the actuator and the leading edge of the wing. A third coordinate system is located on any inviscid streamline. The x_s-axis is in the direction tangential to the inviscid streamline, the z_s-axis is normal to the inviscid streamline and the y_s-axis is normal to the wall. Once the stream-wise and span-wise velocity components are known from direct measurements, the angle of the inviscid streamline follows from trigonometry through α = atan(-w / u), considering the expression $u_s = \sqrt{u^2 + w^2}$ holds. From the angle of the inviscid streamline, u_s and w_s can be computed according to the following coordinate transformation matrix, where it should be noted that the minus signs are a result of the chosen coordinate system:

$$\begin{bmatrix} u_s \\ w_s \end{bmatrix} = \begin{bmatrix} \cos(\alpha) & -\sin(\alpha) \\ -\sin(\alpha) & -\cos(\alpha) \end{bmatrix} \begin{bmatrix} u \\ w \end{bmatrix} \tag{4.1}$$

The employed Quantel Evergreen Nd:YAG laser is capable of delivering 200 mJ pulse energy at a repetition rate of 15 Hz and a wavelength of 532 nm and is used to illuminate the FOV, which is located around the mid-span of the actuator. The laser sheet is approximately 1.5 mm thick, is oriented perpendicular to the actuator and the leading edge and is therefore at a 45° angle with respect to the free-stream. One Imager sCMOS LaVision camera featuring a sensor size of 2560 x 2160 pixels is fitted with a Nikon Micro Nikkor 200 mm lens and positioned on the lower right of the wing, whereas the other camera is placed on the upper left of the wing and features an additional Kenko N-AF 2X Teleplus Pro 300 DGX teleconverter to yield a similar FOV despite the additional distance from the measurement region. For convenience, the sensor is cropped in the wall-normal direction to arrive at an effective sensor size of 2560 x 900 pixels. A significant overlap between the two FOV is realised to limit the loss of information in the post-processing procedure. An image rate of 13 Hz is used to avoid phase-locking with the carrier frequency used to operate the plasma actuator. The images are acquired in double-frame mode with an exposure time of 10 μs. Based on the results obtained from the physical calibration involving a double-sided target with dot pattern, the dt is varied between 17 μs for 22 m/s and 22.38 μs for 16 m/s to ensure a particle displacement of approximately 20 pixels in the free-stream. 2000 Images are recorded for each measurement. Furthermore, both cameras feature an f-stop of 8 and are fitted with Scheimpflugs to ensure the images are focused in the complete field of view. Several pressure modules of 600 and 160 Pa are installed to measure the static pressure such that the pressure distribution over the wing can be obtained. The SAFEX fog generator F2010

Plus along with the corresponding SAFEX water-glycol mixture are used to generate tracer particles of approximately 1 μm in diameter. A close-up of the swept wing along with the relevant elements in this experiment can be found in figure 4.6, whereas an overview of the mentioned optical parameters can be found in table 4.4.

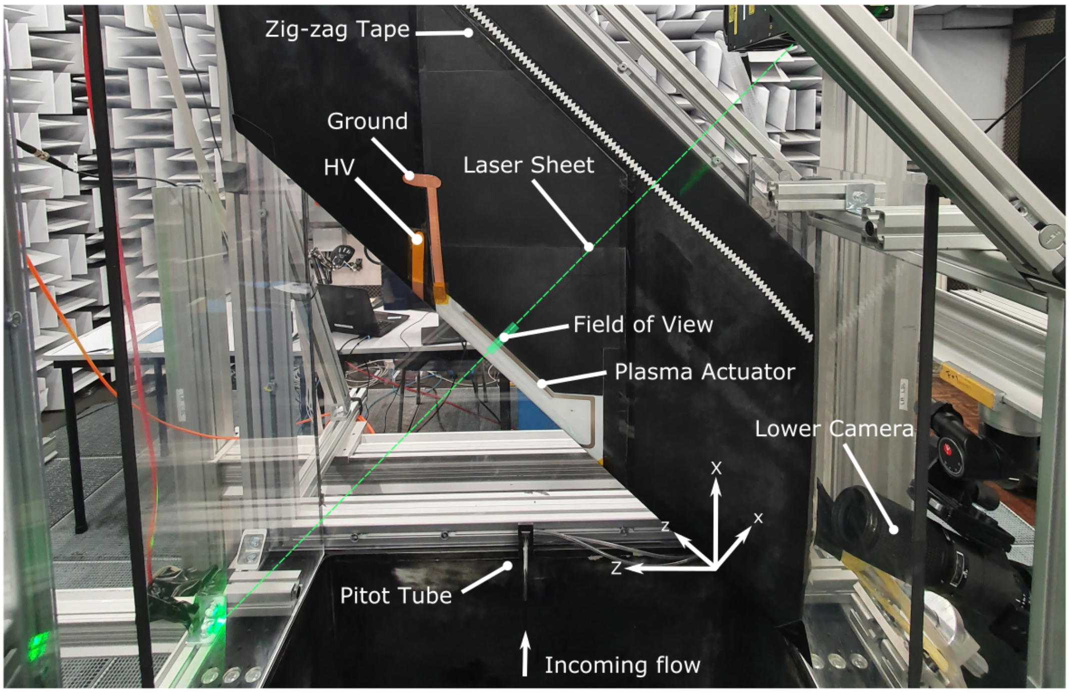

Figure 4.6: Close-up of the experimental set-up for investigating the effect of the AC-DBD plasma actuator on the base flow near the leading edge of the wing.

Parameter	**Upper Camera**	**Lower Camera**
Lens	Nikon Micro Nikkor 200 mm	Nikon Nikkor 200 mm
Teleconverter	-	Kenko N-AF 2X Teleplus Pro 300 DGX
Field of View (FOV)	30.9 x 11.8 mm	30.9 x 11.8 mm
Sensor Size	2560 x 900 px	2560 x 900 px
$f_{\#}$	8	8
Acquisition Method	Double Frame	Double Frame
Acquisition Rate	13 Hz	13 Hz
Image separation time	17 - 22.38 μs	17 - 22.38 μs
Samples acquired	2000	2000

Table 4.4: Optical settings for the wind tunnel experiment focused on the influence of the plasma actuator on the base flow.

4.4.3. Test Matrix

The same test matrix as was used during the mechanical characterisation is adopted for the wind tunnel experiment, although only a single spacing is selected for the configuration consisting of three actuators. The test matrix can be found in table 4.5. In this matrix, experiment 1a is a repeat of various voltage and frequency combinations for a single actuator. The free-stream velocity is set 22 m/s, which is approximately equal to a chord Reynolds number Re_X of $7.59 \cdot 10^5$. Experiment 1b focuses on the effect of the Reynolds number on the effectiveness of the plasma actuators and therefore considers two actuator operating conditions that vary considerably in terms of flow control authority. The velocity is reduced in steps of 2 m/s up to a minimum velocity of 16 m/s, which corresponds to a decrease in Re_X of approximately $7.0 \cdot 10^4$ per step.

Exp.	Spacing	Velocity	Voltage	Frequency
1a	-	22 m/s	12-14 kV_{pp} (steps of 1 kV)	5 kHz
1a	-	22 m/s	15 kV_{pp}	1-5 kHz (steps of 1 kHz)
1b	-	16-22 m/s	12, 15 kV_{pp}	5 kHz
2	6 mm	22 m/s	8, 10, 12 kV_{pp}	5 kHz

Table 4.5: Test matrix for the base-flow wind tunnel experiment.

4.5. Cross-Flow Instability Wind Tunnel Experiment

The focus of the second wind tunnel experiment is on the interaction of the AC-DBD plasma actuator with the (primary) cross-flow instability over the swept wing. The same wind tunnel facility and model are used as in the experiment concerning the base-flow modification, as first presented in subsection 4.4.1. To ensure steady experimental conditions with respect to the cross-flow instability, discrete roughness elements are placed near the leading edge that force the relevant stationary mode. The distance between each neighbouring roughness element is obtained through a preliminary analysis involving a boundary layer solver and linear stability theory. To track the influence of the AC-DBD actuator as well as the growth and evolution of the stationary cross-flow vortices, the laser and single camera are placed on traversing systems, allowing for straightforward planar PIV measurements at consecutive chord locations.

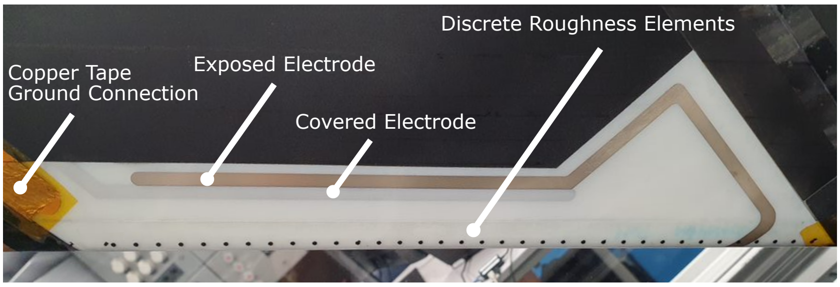

Figure 4.7: Close-up of the wing leading edge, featuring the silver electrodes that make up the plasma actuator and the discrete roughness elements spaced 8 mm apart.

4.5.1. Linear Stability Analysis

Prior to the experimental investigation, a preliminary stability analysis is conducted by considering the velocity and pressure measurements obtained from the preceding experiment. The obtained pressure distribution as well as the C_p-distribution of the M3J reference wing are shown in figure 4.8.

As can be observed, the C_p values of both pressure tap arrays obtained from the initial wind tunnel measurements rather accurately follow the pressure distribution of the M3J. This confirms the ability of the model to replicate the initial section of the C_p distribution of the M3J, allowing for comparisons and alternative, more detailed receptivity and cross-flow instability studies next to the M3J.

The pressures measured at the locations of the pressure taps are employed to estimate the external velocity of the boundary layer. The airfoil geometry as well as the temperature and density are then used to compute the development of the steady, incompressible boundary layer over the wing. The instantaneous velocity field is split into a mean and fluctuating solution and is used as an input for the Orr-Sommerfeld solver to determine the stability characteristics for various frequencies and wavelengths. The frequency is varied from 0 to 1000 Hz in steps of 100 Hz, whereas the chosen wavelength λ ranges from 5 to 11 mm. A comparison of the stationary modes with different wavelengths in the case of a frequency of 0 Hz is presented in figure 4.9a. The predicted instability is seen to be dominated by the 7 and 8 mm wavelengths in the most downstream regions, whereas the smaller wavelengths feature a stronger upstream growth due to the lower local Reynolds number. The result of the most dominant wavelengths being the 7 and 8 mm mode is in agreement with a previous study performed

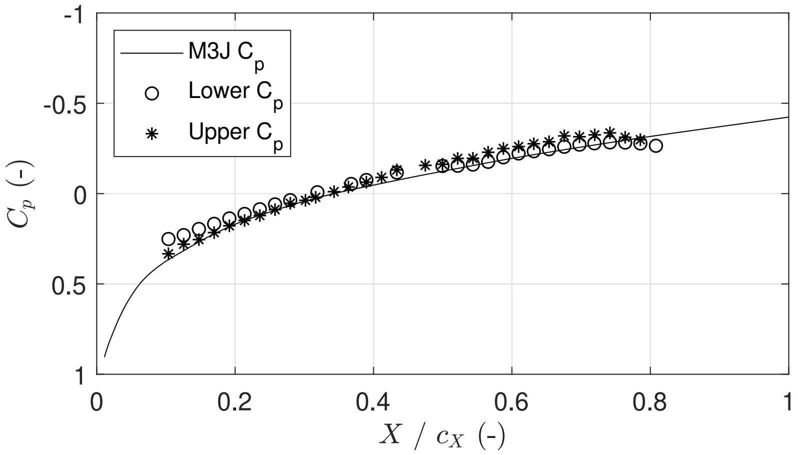

Figure 4.8: Pressure coefficient distribution for the wing used in the wind tunnel experiments in comparison to the M3J wing. The upper and lower C_p values are obtained from the outboard and inboard pressure taps respectively.

by Peng et al. [57]. With the most dominant wavelength on the M3J wing being $\lambda = 8\ mm$, the similarity of the growth of the stationary modes for both wing models is further shown. Interesting to note is the reduced maximum N-factor for the lower wavelengths, which forms the basis of the DRE/UFD flow control technique.

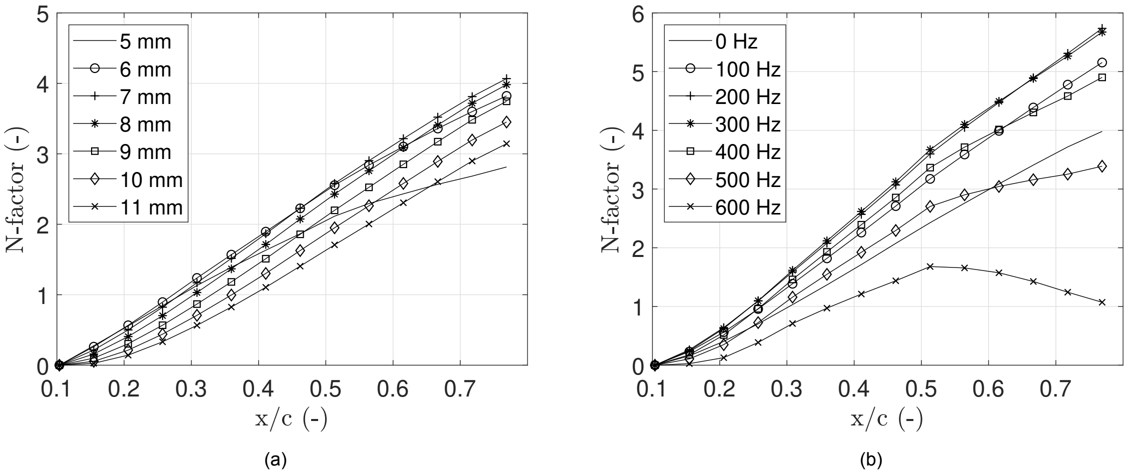

Figure 4.9: (a) N-factor as a function of the wavelength for a frequency of 0 Hz and (b) N-factor as a function of the considered frequency for a wavelength of $\lambda = 8\ mm$.

Figure 4.9b presents the N-factor as a function of different frequencies for the critical wavelength of $\lambda = 8\ mm$. The frequencies pertaining to the largest amplitude growth are found to be 200 and 300 Hz. As the frequency is increased from 0 Hz, the N-factor initially increases for an increase in frequency, after which it decreases again below the level of the stationary mode for frequencies higher than 500 Hz. It is found that for frequencies beyond 600 Hz, the modes do not reach significant N-factors. Thus it can be concluded that the low-frequency modes are more unstable in comparison to the modes of the high-frequency band. This fact necessitates the higher forcing frequencies of the AC-DBD plasma actuators in order to avoid preliminary transition, as also described by Yadala et al. [95]. Nevertheless, as observed from the mechanical characterisation and the frequency spectra, the actuators consistently introduce lower-frequency oscillations even at significantly high carrier frequencies.

The N-factors are visualised as a function of the wavelength and the stream-wise chord location in figure 4.10. When the considered mode is changed from 0 Hz to 200 Hz, the region of higher N-factors (colored in red) shifts upstream, such that higher N-factors are attained at a more upstream chord location. Following the e^{n}-method as presented by Van Ingen [88], it can be assumed that transition occurs when the N-factor passes a threshold value. Therefore, for any considered wavelength, the 200 Hz frequency mode will pass this threshold value at a more upstream chord location in comparison to the 0 Hz mode, resulting in earlier transition. This effect diminishes for the frequency band containing frequencies higher than 400 Hz.

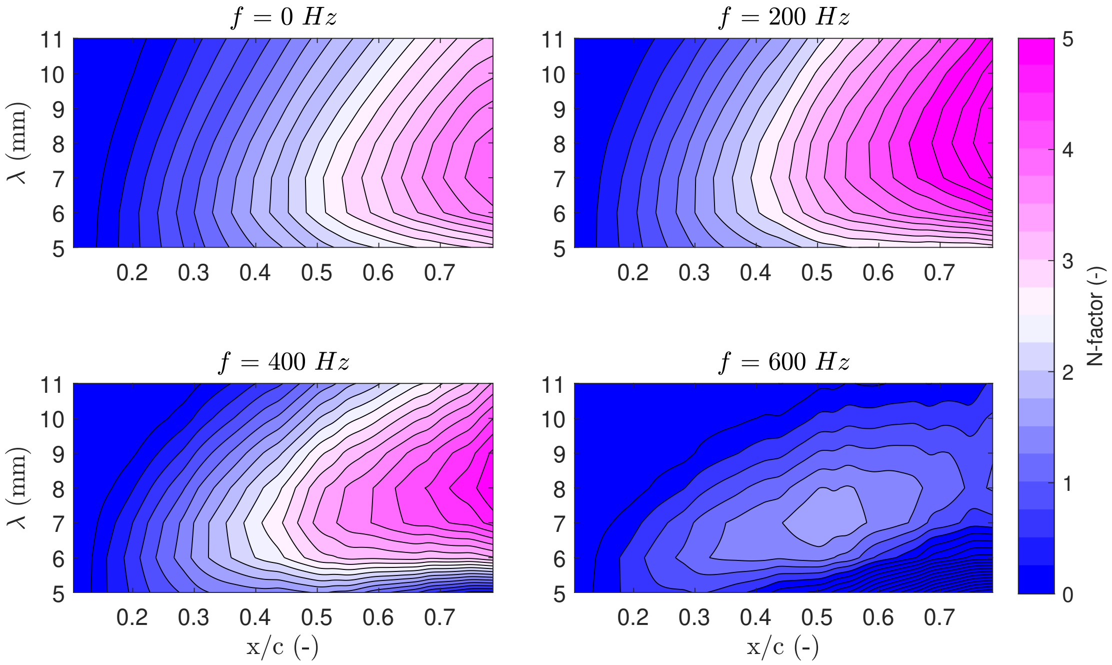

Figure 4.10: N-factor as a function of the wavelength λ and the stream-wise chord location for various frequencies (0, 200, 400 and 600 Hz).

4.5.2. Experimental Setup

As the experimental investigation is focused on the effect of the DBD actuator on the development of the primary cross-flow instability, a series of chord-wise measurements is performed, varying from X/c_X = 0.10 to X/c_X = 0.35. As such, the Quantel Evergreen Nd:YAG laser and the Imager sCMOS LaVision camera, as used in the preceding experiment, have been placed on Zaber traversing systems to adjust the measurement location in stream-wise direction in an accurate and repeatable manner. The thickness of the laser sheet is approximately 1.5 mm. The Imager sCMOS LaVision camera is fitted with a Nikon Micro Nikkor 200 mm lens with an f-stop of 5.6 and is positioned aft of the trailing edge of the wing, imaging a (z,y)-plane that is parallel to the leading edge. The sensor is cropped accordingly for each stream-wise chord location, yielding an average field of view of 36.2 x 6.5 mm with a corresponding sensor size of approximately 2160 x 400 pixels. An image acquisition rate of 13 Hz is used to avoid phase-locking with the carrier frequency of the plasma actuator. The images are acquired in double-frame mode with an exposure time of 10 μs and an image separation time of 20 μs to obtain a pixel displacement in the free-stream of approximately 20. 1000 Images are recorded for each measurement. Discrete roughness elements of 2 mm diameter featuring various spacings and heights are installed downstream of the leading edge, at x/c_x = 0.02, to enhance the stationary cross-flow instability. These elements are formed by laser cutting circular patterns out of black adhesive PVC foil with a thickness of 100 μm. In order to generate taller DREs, the foils are stacked and pasted on top of each other prior to the laser cutting, such that the resulting DREs are of a typical cylindrical shape. The SAFEX fog generator F2010 Plus along with the corresponding SAFEX water-glycol mixture are used to generate tracer particles of approximately 1 μm in diameter. Although not principal to this research, an Optris PI 640 thermal imaging camera is positioned on the structure to record the surface temperature of the wing. The camera has an optical resolution of 640 x 480 pixels and a thermal sensitivity of 75 mK. Although the camera has a frame rate of 32 Hz, when recording, the images are stored instantaneously such that the acquisition rate is only set at 5 Hz. Three halogen lamps of 500 W are used to irradiate the wing surface to improve the contrast between the regions of low and high wall shear stress. 100 Images are recorded for each combination of DRE configuration and AC-DBD plasma actuator operating condition. The actual experimental set-up can be found in figure 4.11, along with a schematic including the various instruments and components.

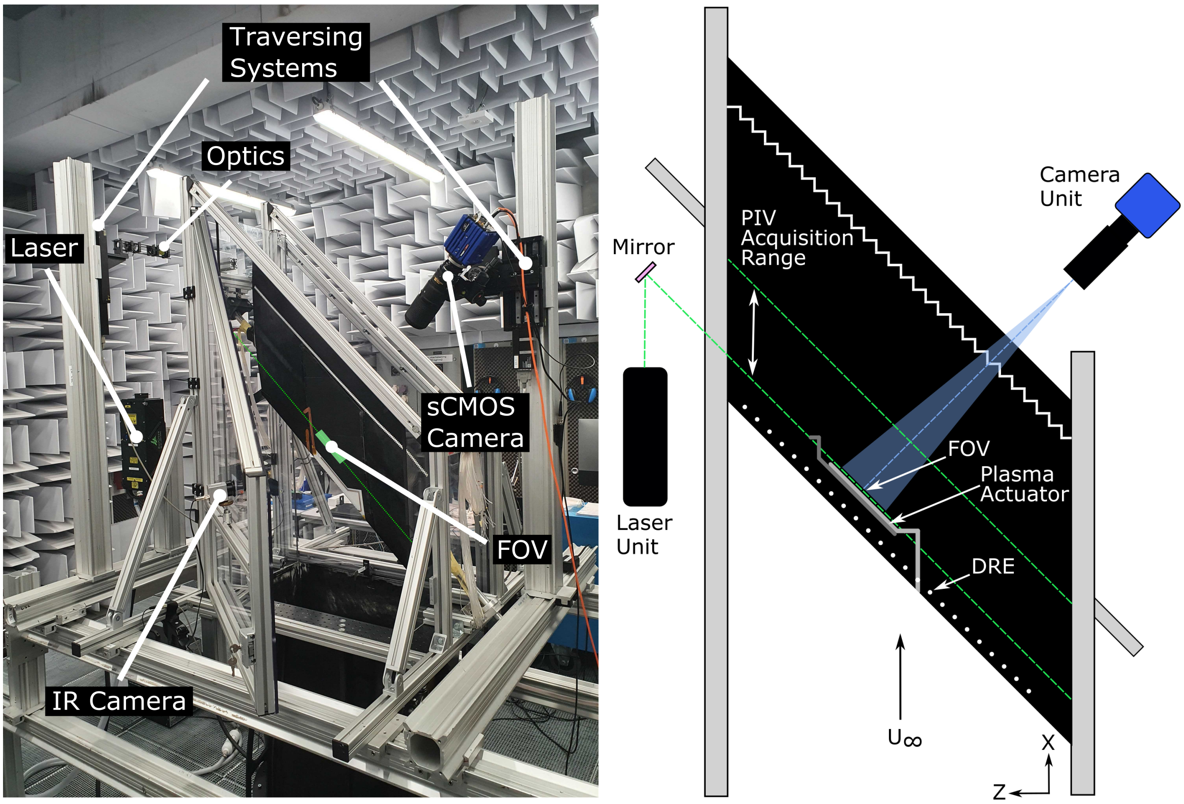

(a)

(b)

Figure 4.11: Experimental set-up for investigating the effect of the AC-DBD actuator on the cross-flow instability (a) and a corresponding schematic indicating the position of the various instruments (b).

The relevant optical parameters are summarised in table 4.6.

Parameter	**Value**
Lens	Nikon Micro Nikkor 200 mm
Field of View (FOV)	36.2 x 6.5 mm
Sensor Size	2160 x ~400 px
$f_{\#}$	5.6
Acquisition Method	Double Frame
Acquisition Rate	13 Hz
Image separation time	20 μs
Samples acquired	1000

Table 4.6: Camera settings for the wind tunnel experiment concerning the effect of the AC-DBD plasma actuator on the cross-flow instability.

4.5.3. Test Matrix

The traversing systems allow for straightforward planar PIV measurements at various stream-wise chord locations. Due to the strut, on which the wing is mounted, blocking the laser light, the most downstream plane at which PIV can be performed is located at 35% of the chord. There is no such limitation on the most upstream plane, although considering the placement of the plasma actuator at approximately 6% of the chord combined with the fact that it is probable that the stationary vortices created by the discrete roughness elements have not grown significantly near the leading edge, the most upstream plane is set at X/C_X = 0.10.

To assess the effect of the different DBD actuator operating conditions on the cross-flow instability, a single upstream and downstream chord location of 15% and 27.5% respectively are chosen at which a frequency and voltage sweep are performed. Following a preliminary analysis of the effect of the induced velocity on the stationary cross-flow vortices, two operating conditions are selected for which measurements are executed at each stream-wise chord location, in steps of 2.5%. Finally, these measurements are conducted for several DRE geometries. From linear stability theory, the highest N-factors are obtained for λ_z= 8 mm, which is in agreement with the results presented by Peng et al. [57]. The initial amplitude of the stationary cross-flow instability is adjusted by changing the height of the DRE. As shown by Peng et al. [57], placing two layers of DRE (200 μm) yields a significant response in terms of the amplitude of the stationary vortices and as such, this configuration is adopted as the primary configuration in this experiment. From hereon the two layers of DREs are referred to as 'L2', whereas one layer of DREs are indicated by 'L1'. With one of the main advantages of base-flow modification in comparison with other UFD and/or DRE methods being the relative insensitivity to environmental conditions, both the height and the spacing of the discrete roughness elements is adjusted. These test conditions are summarised in table 4.7.

Configuration	DRE Height	DRE Spacing	Measurement Chord Location
1a	200 μm	8 mm	15%, 27.5%
1b	200 μm	8 mm	10 - 35% (steps of 2.5%)
2a	100 μm	8 mm	15%, 27.5%
2b	100 μm	8 mm	10 - 35% (steps of 2.5%)
3a	200 μm	6 mm	15%, 27.5%
3b	200 μm	6 mm	10 - 35% (steps of 2.5%)
4a	200 μm	10 mm	15%, 27.5%
4b	200 μm	10 mm	10 - 35% (steps of 2.5%)
5a	200 μm	8 mm	15%, 27.5%
5b	200 μm	8 mm	10 - 35% (steps of 5%)

Table 4.7: DRE configurations for the cross-flow instability wind tunnel experiment.

Table 4.8 contains the various configurations and the associated operating conditions. These operating conditions correspond to those from the preceding experiment and the mechanical characterisation, such that a proper comparison and analysis can be conducted.

Config.	Spacing	Velocity	Voltage	Frequency
1a, 2a, 3a, 4a	-	22 m/s	12-14 kV_{pp} (steps of 1 kV)	5 kHz
1a, 2a, 3a, 4a	-	22 m/s	15 kV_{pp}	1-5 kHz (steps of 1 kHz)
1b, 2b, 3b, 4b	-	22 m/s	14 kV_{pp}	5 kHz
1b, 2b, 3b, 4b	-	22 m/s	15 kV_{pp}	2 kHz
5a, 5b	6 mm	22 m/s	8, 10, 12 kV_{pp}	5 kHz

Table 4.8: Test matrix for the cross-flow instability wind tunnel experiment.

5

Results

This chapter presents the results obtained via the methods discussed in chapter 3 and the experimental setups as presented in chapter 4. First of all, the results of the electrical and mechanical characterisation are presented. Following the characterisation, the results of the first wind tunnel experiment are discussed, revealing the effect of the plasma actuators on the base flow over the swept wing. Finally, the results of the second wind tunnel experiment are elaborated, showing the influence of the actuators on the evolution of the primary cross-flow instability.

5.1. Electrical Characterisation Results

In this section, the results of the electrical characterisation are presented. Knowledge of the average power consumption is required for a fair comparison of the performance for various plasma actuator geometries. Therefore, the shunt capacitor method, as discussed in chapter 3, is employed and consequently Lissajous diagrams are constructed and the average power consumption is calculated.

An example of such an obtained Lissajous diagram can be found in figure 5.1a. As can be seen, the Lissajous diagram has a distinct ellipsoid shape, except for the region spanning from approximately 3000 to 5000 V. This region resembles the positive-going half-cycle of the input signal. The associated current discharges are responsible for these spikes in the diagram. The average power consumption is obtained by computing the average cycle (red) and calculating the enclosed area.

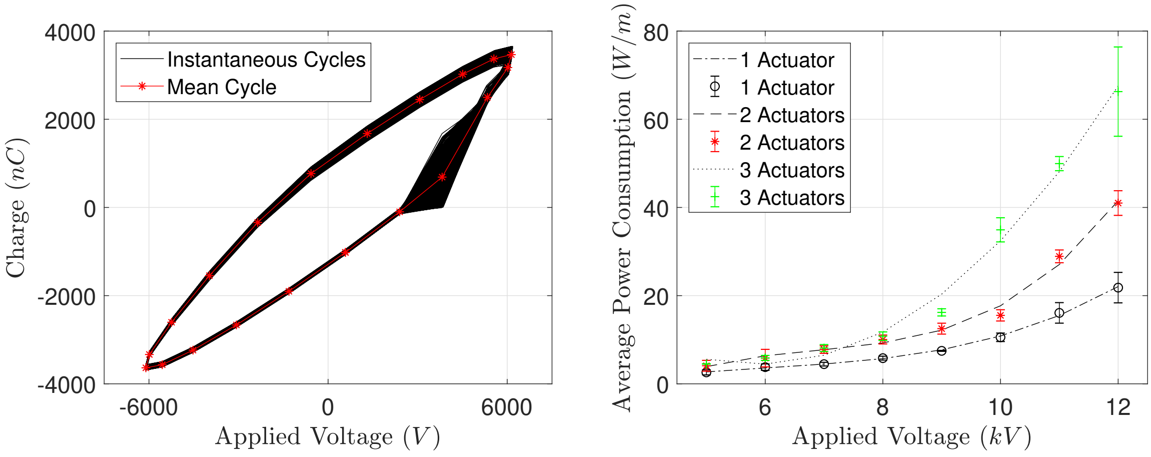

(a)

(b)

Figure 5.1: (a) Lissajous diagram showing 10000 cycles, equal to a measurement time of 0.1 seconds, for the case of 3 consecutive actuators with a spacing of 5 mm (12 kV_{pp}, 5 kHz) and (b) the effect of the number of consecutive actuators on the average power consumption.

As mentioned in chapter 4, a sensitivity study has been performed on the number of actuators, the spacing between consecutive multiple actuators and the thickness of the dielectric material. The former can be observed in figure 5.1b. Here, the calculated values are denoted by the markers and the lines represent power functions that are fit through the data. As the electrodes have a width of 5 mm, the spacing for these multiple actuator configurations has also been set to 5 mm. As expected by the work of amongst others, Enloe et al. [19], the average power consumption increases according to a power law with a magnitude varying from approximately 5/2 to 7/2. It can be seen that for lower voltages, where there is a limited generation of plasma, the power consumption for the three configurations is nearly equal. Only when the voltage is increased does the average power consumption change significantly for the various arrangements. A nearly linear trend can be observed once the voltage is increased, where the two and three AC-DBD plasma actuator configurations have respectively a two and three times higher power consumption in comparison with the single actuator. The error bars are derived from the cycles pertaining to the maximum and minimum power consumption.

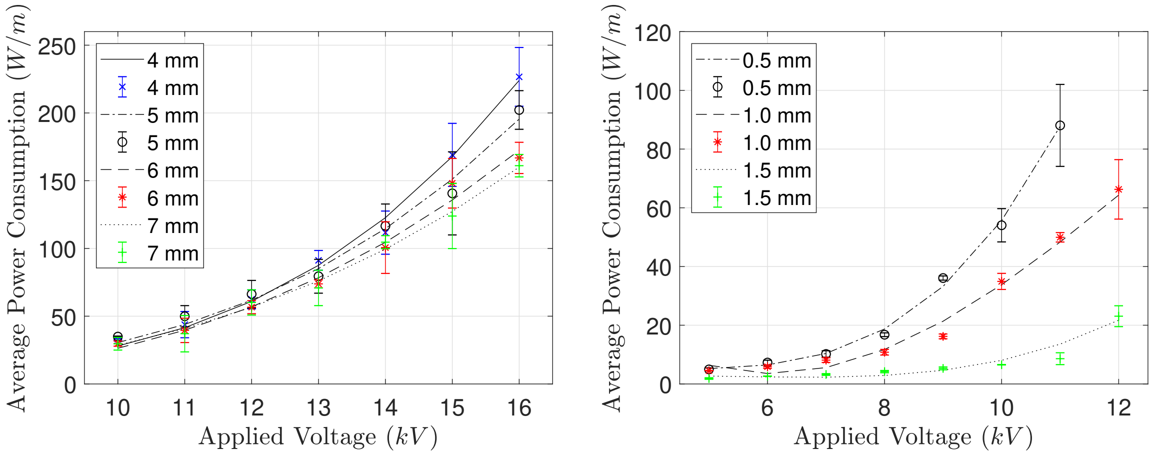

(a)

(b)

Figure 5.2: (a) Effect of the spacing between three consecutive actuators operated at 5 kHz on the average power consumption and (b) the effect of the dielectric thickness on the average power consumption for the case of 3 consecutive actuators with a 5 mm spacing operated at 5 kHz.

Following the calculations regarding the power consumption for a variation in the number of actuators, the spacing between each actuator is varied for the configuration featuring three consecutive plasma actuators. The resulting average power consumption can be observed in figure 5.2a, where furthermore the voltage range has been extended to a higher value. The difference in power consumption at higher voltages can be attributed to the additional formation of plasma in the reverse direction, or backward plasma. At high voltages, it is observed that the actuators featuring a small spacing (i.e. 3 and 4 mm) start to form plasma that reaches from the upstream exposed electrode to both the downstream and upstream covered electrode. Not only do these additional (current) discharges result in a considerable increase in the average power consumption, they furthermore counteract the main purpose of the AC-DBD plasma actuator, which is to induce a velocity in a specified direction. These observations are in agreement with those presented by Do et al. [13], who refer to this phenomenon as 'cross-talk'. It should be noted that by changing the spacing of the electrodes, the length of the electrical circuit is affected accordingly, influencing its characteristics. Nevertheless, it is expected that this effect is of limited importance considering the differences in total circuit length on a case-to-case basis are sufficiently small.

Finally, the thickness of the dielectric material (PET-G) is varied between 0.5 and 1.5 mm. In agreement with the results presented by Thomas et al. [87], a lower dielectric thickness results in a higher power consumption for the same applied voltage. Thomas et al. [87] refer to the saturation condition, beyond which an increase of the applied voltage yields a significant increase in power consumption with a limited effect on the generated thrust. This saturation condition is the result of filamentary structures (or streamers) in the plasma, which develop at higher applied voltage and frequency combinations. By increasing the dielectric thickness, the dielectric breakdown voltage is increased and as such, the maximum achievable voltage can be achieved before the onset of saturation. Furthermore, a thicker dielectric material is less prone to degradation.

5.2. Mechanical Characterisation Results

In this section the results of the mechanical characterisation are discussed. The performance of the actuator is quantified in quiescent conditions by making use of high-speed time-resolved 2D2C-PIV. The performance of the actuator is analysed qualitatively from the induced velocity field and quantitatively by calculating the generated thrust, the induced body force and the frequency spectra. The methods related to these parameters have been discussed in chapter 3.

5.2.1. Raw Data Processing & Uncertainty Quantification

The particle images are cross-correlated with the DaVis 10.1 software through a multi-pass vector calculation. The initial interrogation window is 48 × 48 pixels, whereas the final interrogation window is 12 × 12 pixels and has a 50% overlap. Succeeding this final pass, the resulting vector field features a uniform spacing of 0.0649 mm, or approximately 15 vectors per mm.

Prior to the analysis of the velocity fields, a convergence and uncertainty study is performed. The convergence of the mean and the standard deviation of the u and v velocity components are monitored in DaVis. Due to the inherent fluctuating nature of the AC-DBD plasma actuators, convergence of the mean and the standard deviation of the induced velocity is only achieved at a large amount of frames and as such, the complete set of 19403 images is used for further analysis. The uncertainty field is similarly obtained from DaVis, which makes use of the time-averaged uncertainty formulas presented in chapter 3. The resulting uncertainty fields for both velocity components and a single AC-DBD plasma actuator case are presented in figure 5.3.

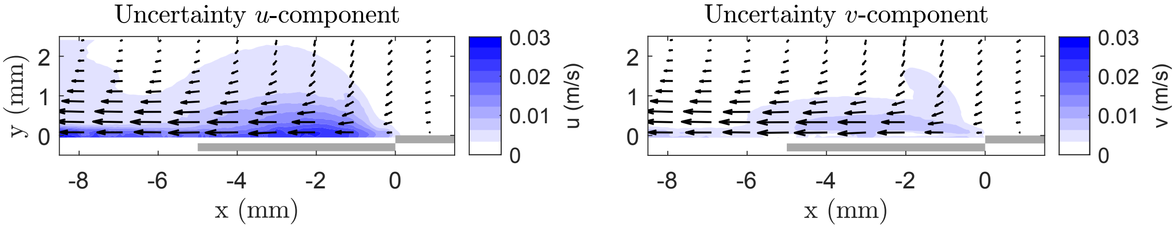

Figure 5.3: Time-averaged uncertainty field of the u velocity component (left) and the v velocity component (right), obtained from 9701 double-frame images for a single actuator (15 kV_{pp}, 5 kHz). The vectors indicate the direction and magnitude of the total velocity U.

The statistical uncertainty is rather low due to the large number of frames. The highest uncertainty can be found in the vicinity of the wall, where the fluctuations and velocity gradients are largest. Assuming an induced velocity in the order of 3 m/s, the maximum statistical uncertainty for the mean and the standard deviation are in the order of 0.03 / 3 ≈ 1% for this experiment.

5.2.2. Induced Velocity Field

Two plasma actuator configurations have been considered for the experiment regarding the mechanical characterisation. These configurations consist of a single actuator and three consecutive actuators with various spacings. The velocity fields for the different AC-DBD plasma actuator configurations are presented below.

Single AC-DBD Plasma Actuator

As an example, the time-averaged induced velocity field for the u and v velocity components for a single actuator operated at 14 kV_{pp} and a carrier frequency of 5 kHz is presented in figure 5.4. The u velocity field shows that a typical wall-parallel velocity jet is formed, which reaches its maximum at the covered electrode and decreases downstream due to viscous dissipation. Furthermore, it can be observed from the total velocity vectors that the maximum induced velocity in the jet is achieved above the wall, at approximately $y = 0.5\ mm$. When compared to u, the magnitude of the velocity component v is significantly smaller. The maximum is found slightly downstream of the intersection of the electrodes, whereas the region of influence is crown-like with respect to u. A moderately strong suction effect is present near x = 0 mm, after which the flow turns 90 degrees and the wall-parallel jet is formed.

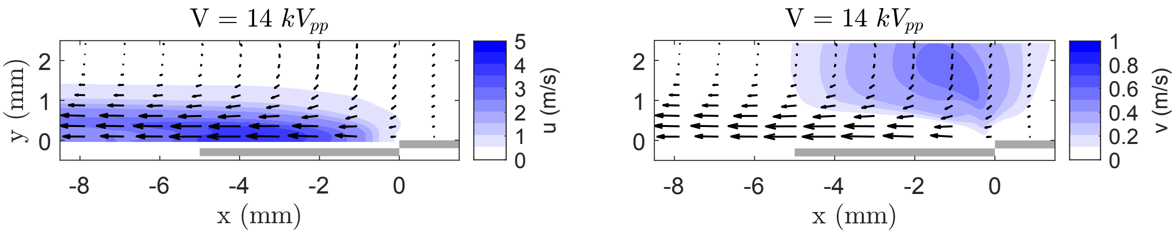

Figure 5.4: Time-averaged velocity field of the u velocity component (left) and the v velocity component (right) obtained from 9701 double-frame images for a single actuator (14 kV_{pp}, 5 kHz). The vectors indicate the direction and magnitude of the total velocity U.

The mean and standard deviation of the total velocity field for a single actuator operated at 14 kV_{pp} and a carrier frequency of 5 kHz can be found in figure 5.5. As expected, the largest velocity fluctuations are located slightly downstream of the exposed electrode, where the bulk of the induced body force is located and the fundamental frequency is introduced into the flow. Furthermore, fluctuations are observed at the wall and in the jet, downstream of the covered electrode. This can be attributed to the finite spatial resolution of the PIV measurements in combination with the influence of the inherent unsteadyness and the viscous effects at the wall.

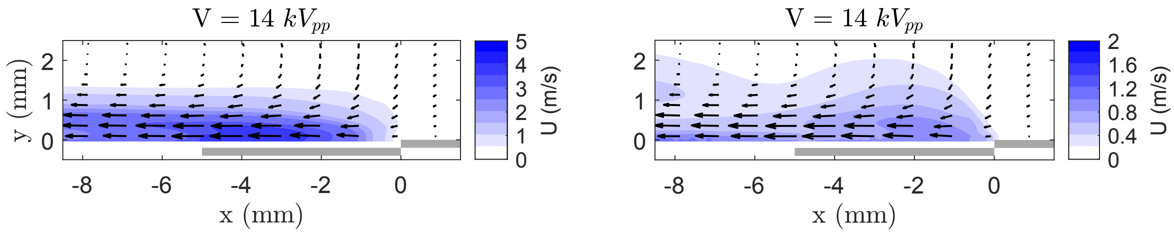

Figure 5.5: Mean (left) and standard deviation (right) of the total velocity field (U) of 9701 double-frame images for a single actuator (14 kV_{pp}, 5 kHz). The vectors indicate the direction and magnitude of the total velocity U.

As an indication, time-averaged induced velocity fields for a single actuator operated at various carrier frequencies and applied voltages are shown in figure 5.6.

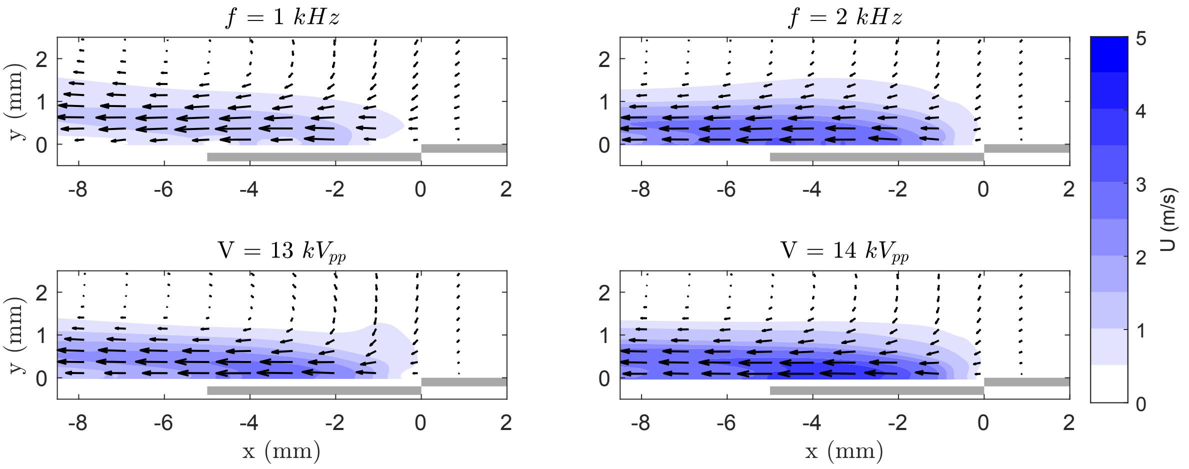

Figure 5.6: Time-averaged total velocity field U of 9701 double-frame images for a single actuator operated at 15 kV_{pp} and 1 kHz (top left), 15 kV_{pp} and 2 kHz (top right), 13 kV_{pp} and 5 kHz (bottom left) and 14 kV_{pp} and 5 kHz (bottom right).

As expected, when the voltage is increased from 13 kV_{pp} to 14 kV_{pp}, the induced velocity increases accordingly. Of interest is the change in morphology of the induced velocity jet by increasing the carrier frequency. In the case of 1 kHz, the jet is directed at a slight upward angle with respect to the wall. The relatively low carrier frequency results in the formation of weak plasma, in correspondence to the low power consumption observed from the electrical characterisation. As a result, the velocity jet is too weak to overcome the viscous effects near the wall and instead moves away from it. Increasing the carrier frequency to 2 kHz already yields a more parallel wall jet with a higher maximum induced velocity. As increasing the carrier frequency results in more collisions between the ions and the gas, there is an increase in the electrohydrodynamic force and therefore a higher induced velocity, as discussed by Benard & Moreau [5].

Multiple AC-DBD Plasma Actuators

In addition to a single AC-DBD plasma actuator, a configuration featuring multiple (i.e. three) consecutive actuators has been investigated. Employing multiple actuators in series offers the benefit of a larger region of active flow control and higher electric wind velocities. As described by Enloe et al. [19], the effect of multiple actuators is additive when stationed not too far apart.

In figure 5.7, three time-averaged total velocity fields are presented for a configuration featuring three DBD actuators in series. The spacing between each exposed electrode and the subsequent covered electrode is varied between 5 and 7 mm. As can be observed, the most upstream actuator introduces a wall-parallel velocity jet, which is then further accelerated by the two downstream actuators. When the actuators are placed in too close proximity, there is a possibility of cross-talk, as previously discussed in section 5.1. On the other hand, when the actuators are positioned too far apart, the velocity jet induced by the first actuator will have diminished in magnitude due to viscous dissipation once the flow reaches the second actuator. In this case, the flow at the second actuator is re-accelerated from a low velocity, such that the efficiency decreases and the configuration featuring multiple actuators loses the desirable additive velocity effect.

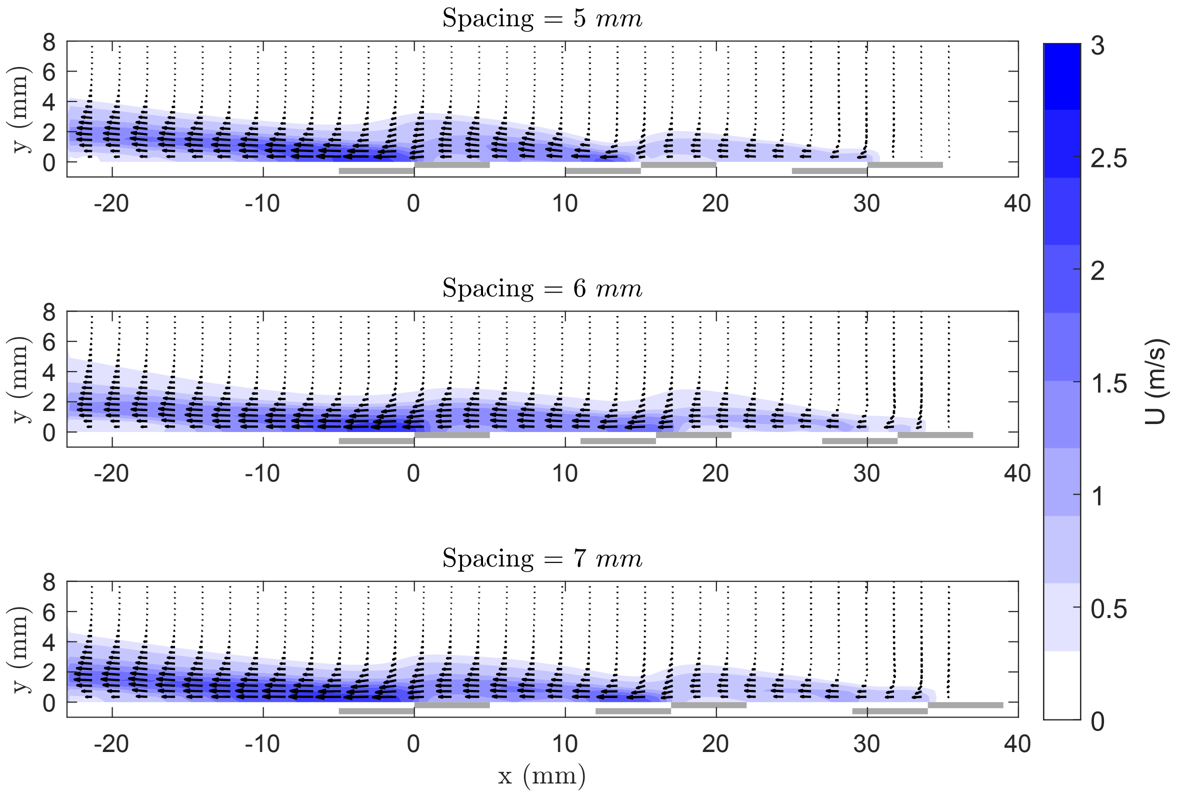

Figure 5.7: Time-averaged total velocity field U of 19403 single-frame images for three consecutive actuators operated at an applied voltage of 12 kV and a carrier frequency of 5 kHz.

As can be observed from the length of the velocity vectors in figure 5.7, the case where the actuators are placed in series with a 7 mm spacing yields the highest induced velocity jet downstream of the cascade. This is confirmed by visualising the horizontal velocity component u along a line located at y = 0.73 mm, as seen in figure 5.8a. The drawn actuators represent the locations of the electrodes for the configuration featuring a 5 mm spacing. The difference in electrode positions for the various spacings explains the slight horizontal shift between the curves. The induced velocity does not increase linearly with the number of actuators, although a significant increase in velocity is obtained of approximately 50% with each subsequent actuator in the case of an applied voltage of 12 kV. Downstream of the electrode cascade, the configuration with a 7 mm spacing attains the highest induced velocity, whereas the other two configurations achieve slightly lower values. Figure 5.8 shows how the induced velocity varies with an increase in applied voltage. As can be observed, the induced velocity increases with the applied voltage and the additive effect is reduced for lower voltages. This can be explained by the fact that when a lower voltage is supplied, the induced velocity reduces. By the time the low-velocity jet of the upstream actuator arrives at the downstream actuator, it has dissipated considerably and lost most of its momentum due to viscous effects. The flow then has to be re-accelerated from a value close to zero, after which this cycle repeats at the next DBD actuator.

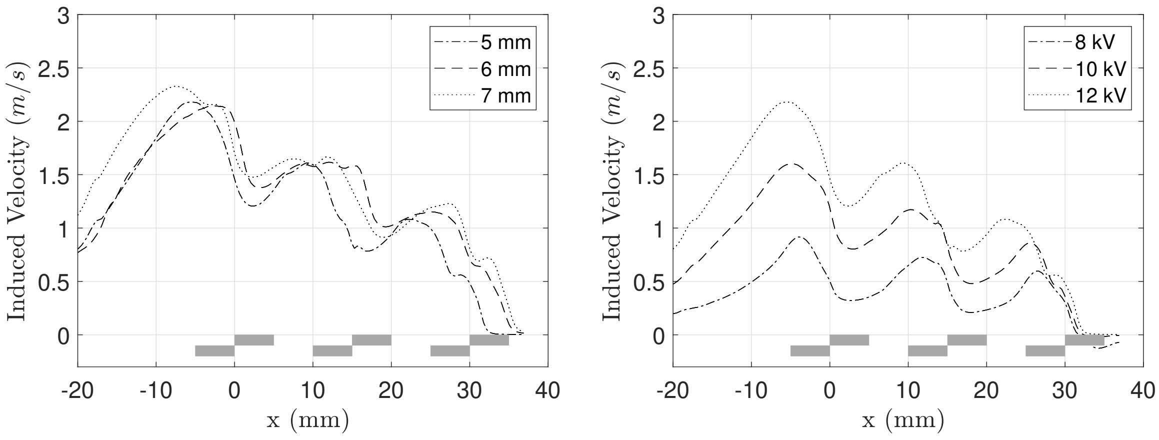

(a)

(b)

Figure 5.8: (a) The influence of the spacing between three consecutive actuators in series, operated at 12 kV_{pp} and 5 kHz and (b) The influence of the applied voltage on the induced velocity for the configuration featuring three actuators in series with a spacing of 5 mm, operated at a carrier frequency of 5 kHz. Curves shown for y = 0.73 mm.

Although the induced velocity (or thrust) plays an important role in the selection of the most effective and efficient DBD plasma actuator, as shown in section 5.1, the velocity is generally a function of the voltage or frequency and can therefore be adjusted in a straight forward manner if required. Instead, the uniformity or smoothness of the continuously accelerated wall jet may be of interest. As can be observed in figure 5.8, the shape of the induced velocity jet near the wall is nearly equal for each spacing. However, the contour of the upper free shear layer is not, as can be observed from the height of the velocity jet at, for example, x = 0. As the vertical velocity component v is not insignificant in the vicinity of the intersection of the exposed and covered electrode, placing the electrodes of the actuators in too close proximity results in large wall-normal velocity gradients. On the other hand, when placed too far apart, as discussed, the main benefit of the additive effect of the induced velocity is lost. From the selected configurations, although not shown here, the case featuring a 6 mm spacing shows the smallest vertical velocity v gradient. Another indicator of the degree of parallel flow is the vorticity, defined as the curl of the velocity according to $\omega = \nabla \times U$, which describes the local rotational motion in the flow. The time-averaged vorticity field for the same cases as presented in figure 5.7 can be found in figure 5.9.

The positive and negative values of the vorticity indicate a clockwise and anti-clockwise rotation respectively. Interestingly, all regions feature a small recirculation region above the induced velocity jet of the most upstream actuator. This is confirmed by the velocity vectors in figure 5.7, which show a range of vectors pointing against the direction of the induced velocity. Clearly the electromagnetic or volumetric body force is strongest slightly downstream of the exposed electrode, inducing a velocity field where nearby particles that are present outside the region of influence move down and upstream, before entering the jet and moving in the negative x-direction. This suction effect is characteristic for the

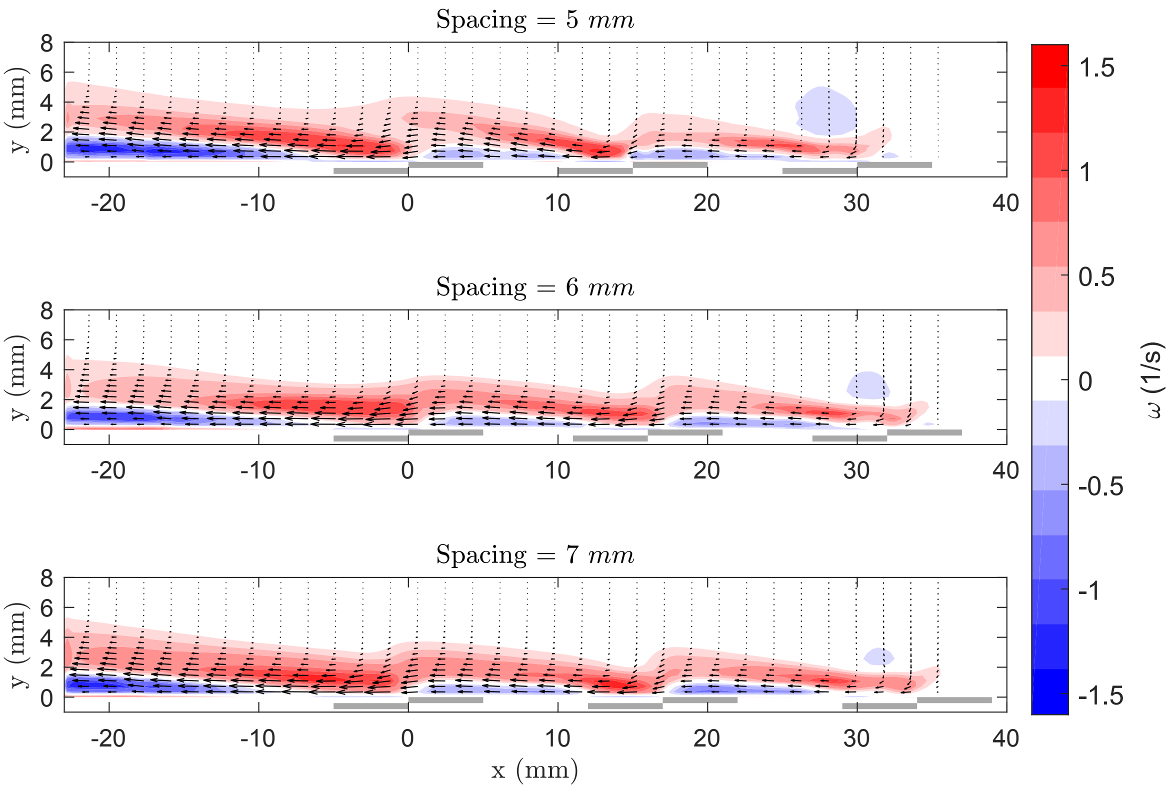

Figure 5.9: Time-averaged vorticity field (ω) of 19403 single-frame images for three actuators in series with various spacings, operated at an applied voltage of 12 kV and a carrier frequency of 5 kHz.

AC-DBD plasma actuator, as similar flow fields are observed in studies by, amongst others, Kotsonis [40] and Thomas et al. [87].

As can be further observed from figure 5.9, regions of anti-clockwise rotation (or negative vorticity) are present between the actuator jet and the wall, which can be explained by the acceleration of the upper region due to the induced velocity jet and the deceleration of the lower region by the presence of the wall. Although the differences are small, it can be observed that the velocity jet is generally of lower vorticity for the configuration with a spacing of 6 mm. This could potentially be attributed to the lower induced velocity that is obtained for this configuration. Nevertheless, the configuration featuring a spacing of 6 mm is chosen for subsequent wind tunnel experiments.

5.2.3. AC-DBD Plasma Actuator Thrust and Body Force

The velocity fields can be further manipulated to obtain insight in the thrust and body force generated by the AC-DBD plasma actuators. The thrust and the body forces are computed from the data set obtained from experiment 1b as discussed in section 4.3, which included the onset of the plasma generation. As such, 1000 images are considered for the determination of the mean flow field and the calculation of the thrust, which is equal to a measurement time of 50 ms. Time-averaged velocity fields are used for the momentum balance method, whereas instantaneous velocity fields are employed for the body force calculation. As the computation of the body force requires velocity gradients, a spatial averaging filter is applied to the instantaneous velocity fields to limit the presence of strong (non-physical) velocity fluctuations. A low-pass 3^{rd}-order Butterworth filter has been applied to the velocity-time signals, where for most cases the cut-off frequency has been set to half the carrier frequency of the high-voltage signal. Filtering the high-frequency fluctuations is required to approximate the time derivative at the start of actuation with reasonable accuracy. The first six images after actuation are considered to approximate the instantaneous acceleration caused by the DBD actuator, which is equal to a measurement time of 3 ms. A brief overview of the used methods can be found in chapter 3 and in the article by Kotsonis [40].

Thrust Calculation

The thrust for a single actuator is calculated according to the momentum balance method. A control volume is placed in the mean velocity field and the momentum equations are applied at the boundaries. The resulting thrust in x- and y-direction consists of the induced velocity as a result of the body force exerted by the DBD actuator as well as the shear force at the wall. The mean velocity field including the constructed control volume for the case of a single actuator operated at an applied voltage of 14 kV and a carrier frequency of 5 kHz is shown in figure 5.10.

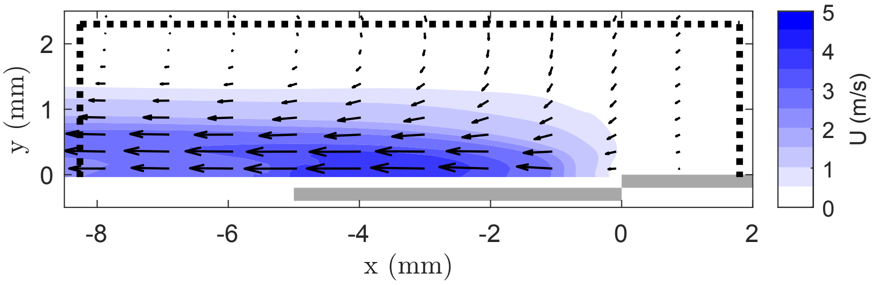

Figure 5.10: Time-averaged total velocity field (U) for a single actuator operated at an applied voltage of 14 kV and a carrier frequency of 5 kHz. The control volume (dotted line) ranges from approximately x = -8 mm to 1.5 mm and from y = 0 mm to 2 mm.

A weak suction effect is present in the region above the electrode pair. As described by Kotsonis [40], this suction effect indicates the presence of a pressure gradient. Far away from the actuator this pressure gradient is negligible, however in close proximity to the actuator this pressure gradient may be rather strong. In order to limit this effect of the pressure on the thrust calculations, the control volume is chosen large enough such that the influence of the pressure is considered to be sufficiently small. Whereas the height of the control volume and the x-position of the right wall have a limited effect on the thrust calculations once positioned far enough from the wall and the inner edge of the electrode, respectively, the position of the left wall has a significant influence on the computed thrust. It is decided that the left wall is placed significantly far away from the bulk of the body force exerted by the actuator and slightly downstream of the location of the maximum velocity. As a result, the control volume is a rectangle, covering the region from approximately x = -8.0 mm to 1.5 mm and y = 0 mm to 2.0 mm. As can be seen, the most significant contribution to the thrust in the x-direction is caused by the outflowing velocity jet through the left boundary. The momentum through the upper and right boundary are fairly small in comparison and, for a first estimate, can even be neglected. Nevertheless, during this research, as these terms are readily available, they are taken into account for all subsequent thrust calculations. The largest contribution to the thrust in y-direction is the upper boundary, which is due to the discussed suction effect.

Body Force Calculation

Following the computation of the thrust according to the momentum balance method, the body force is calculated according to the gradient method, as described in chapter 3. Although the additional terms present in the equations of the gradient method are sufficiently small at t = 0 such that they can be neglected, the gradient method provides a lower uncertainty due to the inclusion of these terms in comparison to the reduced method. Whereas the momentum balance method yields a force that is a scalar quantity, this approach attempts to obtain information on the amplitude and the spatial distribution.

The spatial distribution of the body force for various cases can be observed in figure 5.11. In agreement with the results obtained by Kotsonis [40], the body force presents itself as a concentrated volume slightly downstream of the exposed electrode. Increasing the applied voltage or carrier frequency results in a higher amplitude and a larger region of influence, both in the vertical and horizontal direction. As a larger body force results in a larger acceleration according to the linearised two-dimensional Navier-Stokes equations, these results are to be expected when comparing these results to the previously computed thrust values from the momentum balance method.
A scalar quantity can be obtained for the body force when its distribution is integrated over the spatial domain. The resulting body forces along with the computed thrust values as obtained through the

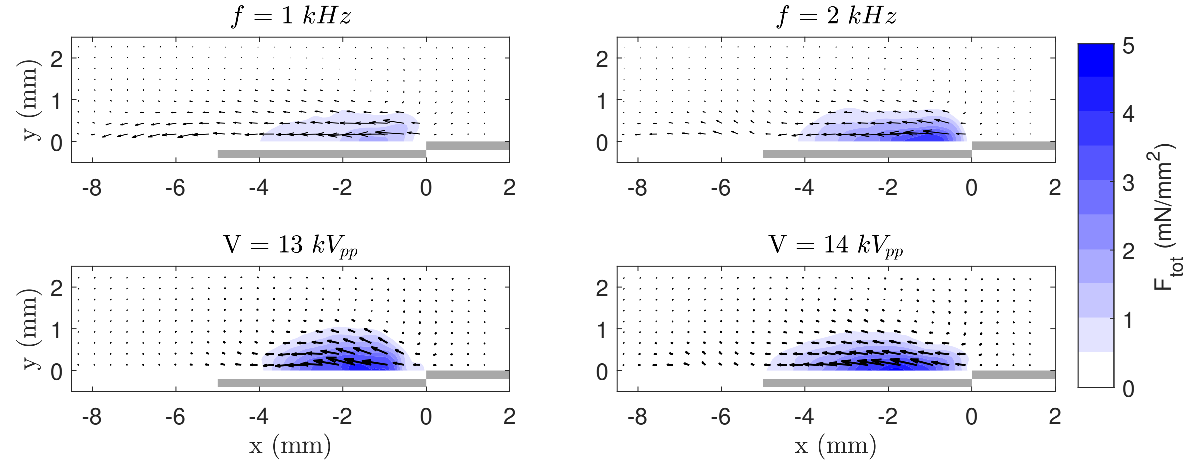

Figure 5.11: Spatial distribution of the body force calculated according to the gradient method for a single actuator operated at 15 kV_{pp} and 1 kHz (top-left) and 2 kHz (top-right) as well as at 13 kV_{pp} (bottom-left) and 14 kV_{pp} (bottom-right) and 5 kHz.

momentum balance method are presented in figure 5.12a and 5.12b. Immediately noticeable is the small discrepancy between the computed thrust and body force, which should theoretically be equal to the wall shear force. It must be noted that the thrust obtained through the momentum balance method is purely a function of the mean velocity field, whereas the body force is computed from only the initial moments after actuation. For this reason the uncertainty of the former is significantly smaller than the latter. Nevertheless, it can be concluded that the body force follows the same trend as the computed thrust.

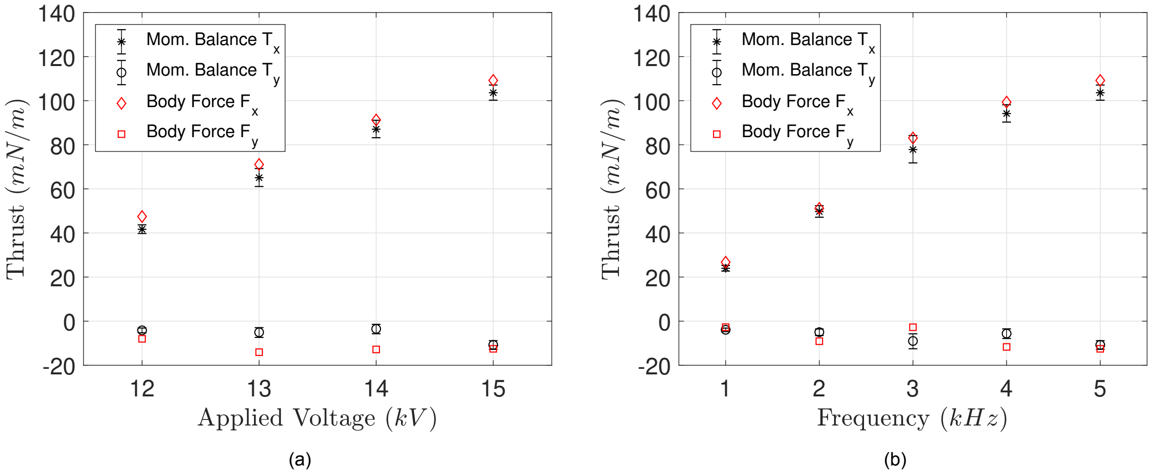

(a)

(b)

Figure 5.12: Computed thrust and body force according to the momentum balance method and gradient method respectively, for a single actuator operated at various applied voltages (5 kHz) (a) and carrier frequencies (15 kV_{pp}) (b).

As can further be observed, the thrust in x-direction per actuator length increases as the voltage or frequency are increased. T_x seems to reach a plateau as the frequency is increased, indicating the potential presence of streamers or filaments. As described by Likhanskii et al. [44] and Corke et al. [11], the increase of the maximum induced velocity (or thrust) with frequency is limited by a phenomenon where the electrons deposited at the dielectric surface during the negative half-cycle do not have enough time to fully relax. The surface discharge then becomes filamentary and as these filaments do not contribute to the electric wind production, as discussed by Benard & Moreau [5], the maximum induced velocity reaches a plateau. Although it is expected that the T_x increases superlinearly as the voltage increases, as observed by amongst others Kotsonis [40] and Benard & Moreau [5], in this case a nearly linear trend can be observed. It is expected the limited amount of data points is the cause of this discrepancy.

Secondly, the thrust in y-direction per actuator length is increasing as a function of the voltage and frequency, similarly to T_x. As the induced velocity in the horizontal direction increases, the pressure gradient or suction effect increases simultaneously, which explains the increase in T_y. This conclusion is in agreement with the observation of the mean velocity field shown in figure 5.4.

5.2.4. Spectral Analysis

Due to the sine input signal and the introduced asymmetric generation of plasma, the velocity field induced by the plasma actuator varies in time. Considering these velocity fluctuations have a particular frequency, a spectral analysis study is of importance when considering the receptivity process and the extreme sensitivity of the cross-flow instability to external disturbances.

The power spectral density is calculated according to the method as proposed by Welch [91] and as described in subsection 3.3.4. The considered quantity is the stream-wise velocity fluctuation $u'(t)$. The acquisition frequency is 20 kHz and the signal is divided into 2000 Hamming windows with an overlap of 50%. The Nyquist frequency is equal to half the sampling frequency, or 10 kHz. From the standard deviation and the location of the body force, it can be deduced that the velocity fluctuations featuring the largest amplitude occur slightly downstream of the electrode intersection, at $x \approx$ -3 mm. The power spectral density is obtained for two cases in the point x = -3 mm and y = 0.3 mm and can be seen in figure 5.13. The frequency is plotted on a logarithmic scale, whereas the PSD is expressed in dB/Hz on a linear scale.

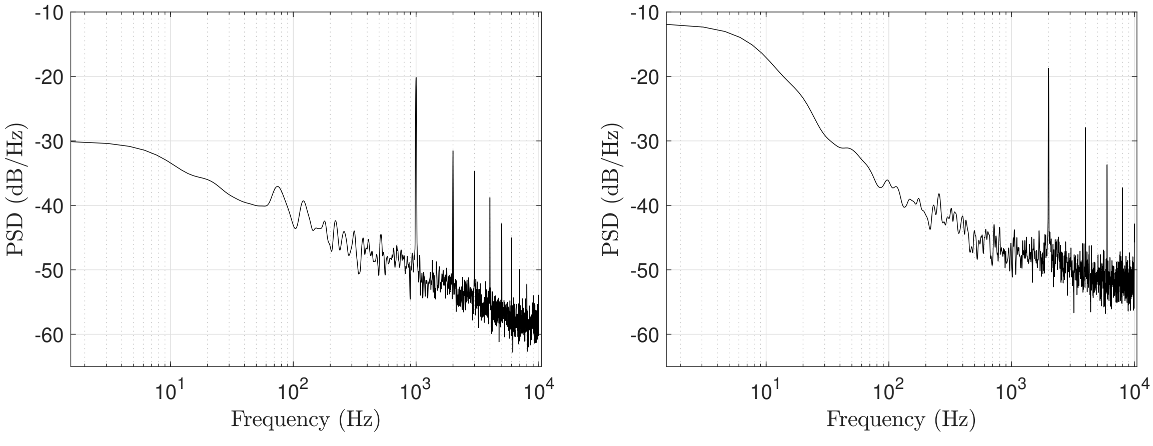

(a) (b)

Figure 5.13: PSD of u' at (-3, 0.3) for a single AC-DBD plasma actuator operating at an applied voltage of 15 kV_{pp} and a carrier frequency of 1 kHz (a) and 2 kHz (b).

Immediately noticeable are the sharp peaks located at the carrier (fundamental) frequency and the corresponding harmonics equal to $f \cdot n$ with n = 1, 2, 3, ..., n. The power is distributed over these fundamental and harmonic frequencies, where the power of a given harmonic frequency decreases as n increases. Furthermore, the power spectral density at lower frequencies (f < 1000 Hz) is rather significant in comparison to the higher frequencies. When the frequency is increased from 1 kHz to 2 kHz, the total power increases and as such, the complete spectra shifts up. This behaviour is seen to saturate for frequencies above 2 kHz. These observations indicate that once the plasma actuator is operating in a consistent manner, that is, the applied voltage and carrier frequency are adequate such that a significant wall-parallel jet is formed, the induced low frequencies feature similar levels of PSD.

Interestingly, the PSD of the case featuring of a single actuator operated at an applied voltage of 15 kV and a carrier frequency of 3 kHz shows further peaks at 8 kHz and 5 kHz. As the division of the sample frequency of 20 kHz by the carrier frequency of 3 kHz does not result in an integer, aliasing occurs, such that the fourth harmonic (12 kHz) and fifth harmonic (15 kHz) are folded or mirrored at the Nyquist frequency of 10 kHz. These peaks at 5 and 8 kHz effectively resemble higher harmonics in comparison with the peak observed at 9 kHz and therefore feature a lower PSD, in agreement with figure 5.14a.

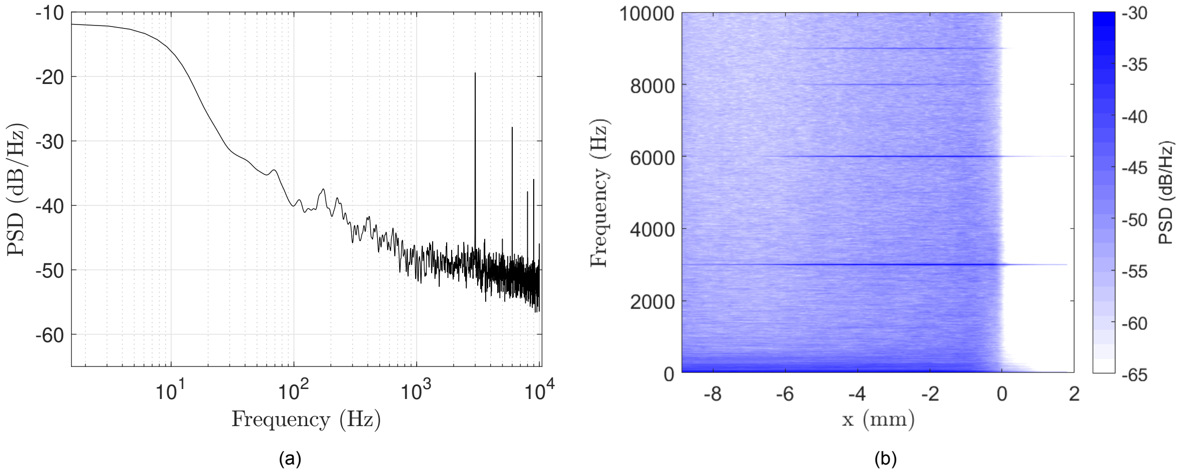

Figure 5.14: PSD of u' at (-3, 0.3) for a single AC-DBD plasma actuator operating at an applied voltage of 15 kV_{pp} and a carrier frequency of 3 kHz (a) and a corresponding PSD contour for y = 0.3 mm (b).

To visualise how the power spectral density is distributed over the frequency range in the spatial domain, the PSD is computed for all x-coordinates at a height of y = 0.3 mm, where the center of the induced velocity jet is located and the standard deviation is highest. The result for the scenario featuring a carrier frequency of 3 kHz can be found in figure 5.14b, whereas the cases featuring a carrier frequency of 1 and 2 kHz are shown in figure 5.15.

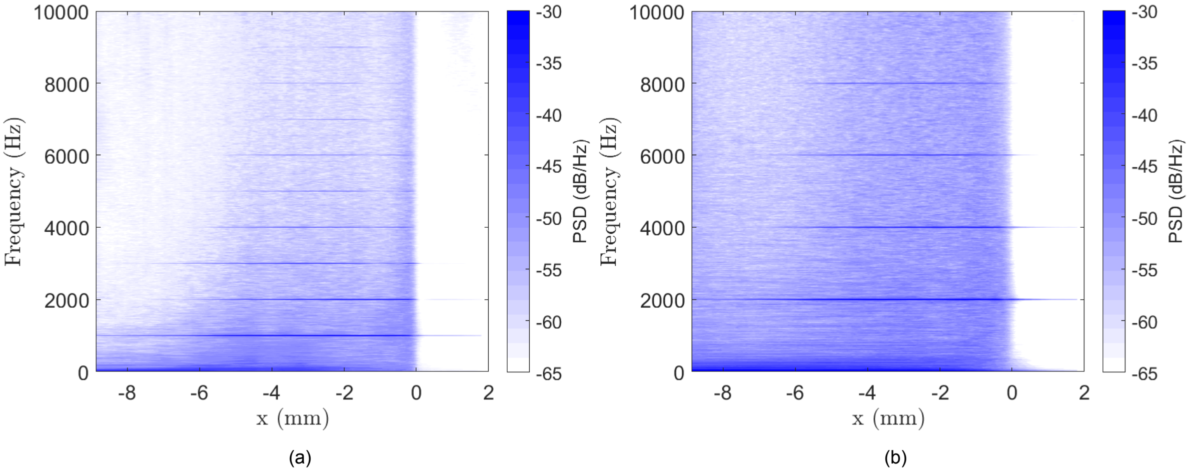

Figure 5.15: Contours of the PSD of u' at y = 0.3 mm for a single AC-DBD plasma actuator operating at an applied voltage of 15 kV_{pp} and a carrier frequency of 1 kHz (a) and 2 kHz (b).

It is evident that apart from a peak at the fundamental frequency, the magnitude and distribution of the power spectral density for the region upstream of the actuator is rather insignificant. Downstream of the location where the electrodes intersect, at x = 0 mm, the fundamental frequency and the harmonic frequencies can be observed for both cases. Interestingly, all harmonic frequencies dissipate at approximately x = -6 mm, whereas the fundamental frequency remains present albeit with a smaller amplitude. Similar observations are made for higher carrier frequencies, although these cases feature larger power spectral densities. It can be concluded that whereas the higher harmonic frequencies are of little influence far away from the bulk of the body force of the DBD actuator, the region of influence of the fundamental frequency is significant.

Furthermore, in the lower section of figure 5.15, a dark region can be observed for both the 1 and 2 kHz carrier frequency. This darker region indicates higher values for the power spectral density in the frequency band ranging from 0 to approximately 1000 Hz, as previously concluded. Although these are small in comparison with the harmonic peaks, the lower frequency modes are more unstable than high frequency modes according to linear stability theory and are therefore of significant importance in the cross-flow instability transition process. These lower-frequency fluctuations have the capability of directly or indirectly triggering travelling cross-flow waves, resulting in early transition, as also described by Yadala et al. [96]. Furthermore, Serpieri et al. [84] note that these low-frequency fluctuations can also directly affect the secondary instability, considering the latter is similarly of unsteady and convective nature, as concluded by both Malik et al. [50] and Wassermann & Kloker [90]. It is clear that for efficient and effective laminar flow control, these low-frequency disturbances should be mitigated as much as possible such that the amplification of travelling cross-flow instability modes is limited.

5.3. Base-Flow Wind Tunnel Experiment Results

Following the electrical and mechanical characterisation, a wind tunnel experiment is conducted that is dedicated to investigating the influence of the AC-DBD plasma actuator on the base flow. Stereoscopic PIV is employed to measure the change in all three velocity components, although emphasis is placed on the stream-wise and span-wise velocity components u and w. The results and outcome are presented in this section.

5.3.1. Raw Data Processing & Uncertainty Quantification

Prior to the cross-correlation process in DaVis 10.1, several operations are performed to improve the quality of the particle images. A self-calibration is performed to reduce the calibration error that is present when the calibration target is not in the same plane as the light sheet. As it is observed the vibrations are of significant influence, a shift-and-vibration correction is applied to ensure a non-moving wall. During the pre-processing, the background noise is removed and the shape of the particles are enhanced to improve the cross-correlation. An initial window size of 48 × 48 pixels is used, whereas the final passes feature a window size of 12 × 12 pixels with a 50% overlap. The resulting vector grid features a spacing of 0.0722 mm, which is equal to approximately 14 vectors per mm. The maximum time-averaged statistical uncertainty as obtained from DaVis 10.1 is approximately 0.07 m/s for the u-component, 0.04 m/s for the v-component and 0.30 m/s for the w-component. Clearly, the out-of-plane component (w) features a significantly higher uncertainty, as is expected from the stereoscopic PIV set-up. These maxima are located in the vicinity of the plasma actuator, whereas lower uncertainties are found for the boundary layer itself. The uncertainty in the free-stream is approximately 0.005 m/s for the u and v component and 0.018 for the w velocity component.

Preceding the analysis of the velocity fields and profiles, several processing operations are performed such that the results can be compared in a fair manner. The first action is to find the location of the wall. This is accomplished by locating the reflection, which is caused by the illumination of the laser, and the associated points of maximum intensity in the raw PIV images. A set of 50 images is used to create a an intensity image that features the absolute minimum intensities within the set of images. As a straight line fails to adequately approximate the airfoil section that is present in the FOV, a 3^{rd}-order polynomial is fitted to the identified intensities that are above a threshold value, such that a good approximation of the contour of the wing is obtained. This process is visualised in figure 5.16.

The next operation involves a coordinate transformation from the Cartesian (x, y) grid to a curvilinear (ξ, η) grid. The polynomial that approximates the wall is discretised with a wall-parallel spacing that is equal to the original spacing of the Cartesian grid, after which the slope of the wall at each location is determined and equidistant points are introduced that are perpendicular to the local wall. The values on the curvilinear grid are then determined through linear interpolation, using the values on the Cartesian grid as input. A visualisation of this grid with respect to the velocity fields as obtained directly from DaVis 10.1 is found in figure 5.17. It should be noted that the obtained velocity field is tilted (as in figure 5.16 and 5.17), as the calibration plate was placed at an angle with respect to the camera FOV and both camera FOVs are mirrored with respect to each other.

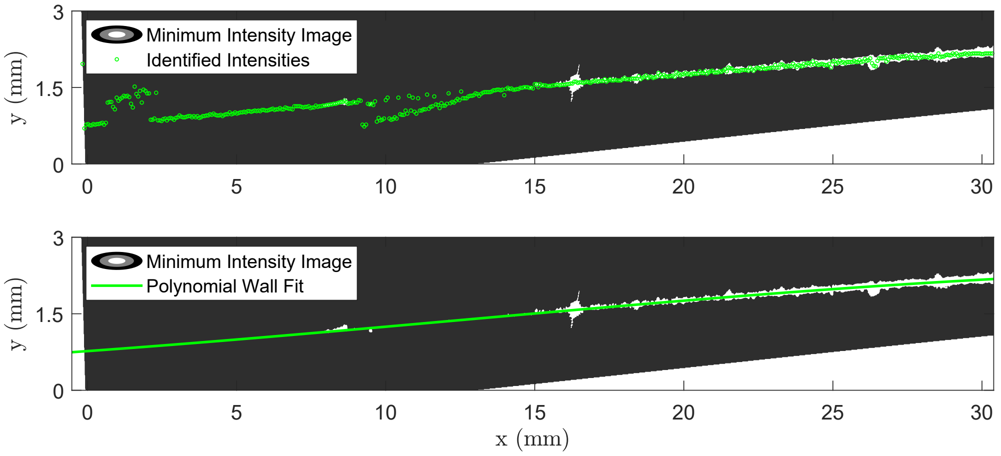

Figure 5.16: Bottom section of a minimum intensity image. The background is black and the reflections at the wall are white. Identified intensities beyond a threshold value are shown as dots in green (top) and the resulting wall polynomial is shown as a green line (bottom).

By calculating the slope of the boundary layer at each location, the linear region is found and extrapolated to 0 m/s to provide an updated approximation of the wall and the velocity profile. Doing so means that information on the velocity very near to the wall is lost, however, as the velocity profiles typically already feature a non-physical inflection near the wall due to the reflection of the laser and the associated mirroring effect in the cross-correlation, this procedure is assumed to be reasonable. Furthermore, although it is expected that (weak) cross-flow vortices are present, the influence of these is assumed to be sufficiently small such that the following analysis and comparison remains valid. A final coordinate transformation is carried out to arrive at the velocity profiles along and perpendicular to the inviscid streamline. The angle of the inviscid streamline is found through trigonometry and the magnitude of u and w, after which the components are projected on the (rotated) coordinate system (x_s, z_s). This relevant coordinate system was already introduced in chapter 4. Finally, a spline interpolation is applied to the resulting velocity profiles such that these can be used as input for numerical solvers for potential future analysis.

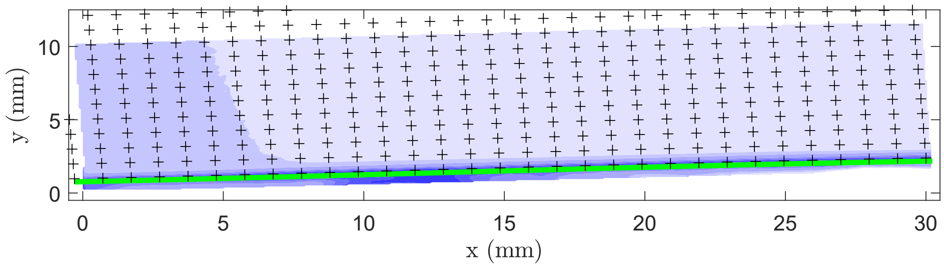

Figure 5.17: Example of a velocity field obtained from DaVis 10.1 (blue colorscale) featuring the approximated wall location (green line) and the introduced wall-normal and -parallel grid (+).

5.3.2. Results

To obtain an idea of the general effect of the plasma actuator on the boundary layer, the stream-wise u and span-wise w velocity profiles are considered in the FOV that is perpendicular to the leading edge of the wing. The varied parameters are the carrier frequency and the applied voltage of the AC-DBD plasma actuator as well as the free-stream velocity (or Reynolds number). The effect of each of these parameters on the magnitude and shape of the respective velocity profiles is presented below. Unfortunately, due to time constraints, the AC-DBD plasma actuator configuration featuring three consecutive electrode pairs has not been tested in this experimental campaign.

Effect of Carrier Frequency

To assess the influence of the AC-DBD plasma actuator on the incoming flow, the velocity profiles perpendicular and tangential to an inviscid streamline are considered at several chord locations. These chord locations are positioned on a line that is perpendicular to the leading edge, ranging from approximately X/c_X = 0.05 to X/c_X = 0.12, where it can be imagined that each location represents a different inviscid streamline. It must be reiterated that the hereafter discussed contours and velocity profiles are presented on the wall-normal and wall-parallel grid in the (x_s, y_s, z_s) coordinate system, which is obtained after the coordinate transformation as discussed in chapter 4.

To visualise the effect of the plasma actuator on the flow field, the flow field where the plasma actuator was inactive (i.e. clean configuration) has been subtracted from the cases pertaining to the various carrier frequencies. These contours are initially presented for the total velocity $U_s = \sqrt{u_s^2 + w_s^2}$ in figure 5.18.

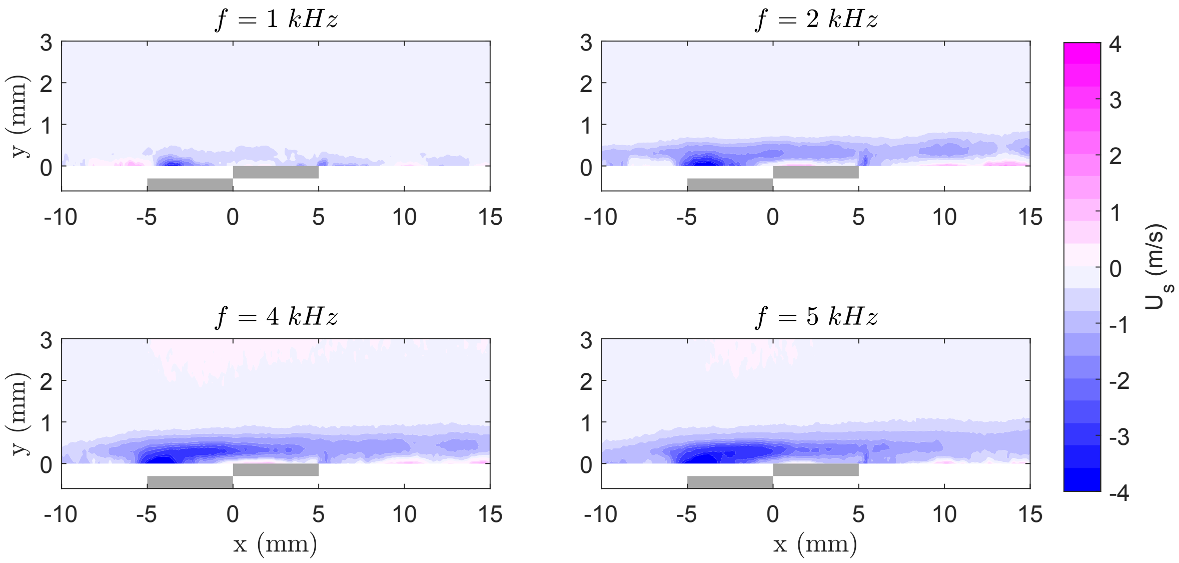

Figure 5.18: Mean total velocity U_s contours displaying the difference between the respective carrier frequency (15 kV_{pp}) and the clean configuration. Visualised on the curvilinear (ξ, η) grid.

As the cross-flow component w is significantly small compared to the stream-wise velocity component u, the same conclusions from these contours can be made for the velocity component u_s. Considering stereoscopic PIV has been employed for this experiment and the span-wise velocity component w was the out-of-plane component, which is known to be less well-resolved, the associated contours for w_s are significantly more noisy. Nevertheless, the result of the actuation of the DBD actuator is a decrease in velocity, as can be observed from figure 5.19. It must be noted that the cross-flow component is negative when adhering to the chosen coordinate system, such that a reduction in magnitude results in a positive difference. Interestingly, a small bump of higher velocity is located at the covered electrode, which is present for all the cases where the AC-DBD plasma actuator is active. The largest effect is seen in the neighbourhood of the actuator, as expected and in agreement with the mechanical characterisation. Increasing the frequency yields a larger induced velocity and therefore a larger effect on the incoming flow. Interestingly, the magnitude of the reduction in velocity is not too dissimilar from what has been measured by the mechanical characterisation. This is an indication that the plasma actuator remains effective even at higher free-stream velocities, as it operates close to the wall and within the boundary layer, where the velocity is significantly lower.

To quantify the influence of the actuator on the base flow, the boundary layer profiles tangential and perpendicular to the inviscid streamlines are considered at various chord locations. The profiles are normalised according to the edge velocity U_e of the respective clean configuration (i.e. without plasma active) and the wall-normal distance is normalised with the boundary layer height of the clean configuration. The boundary layer edge is assumed to be located at the point where the external velocity

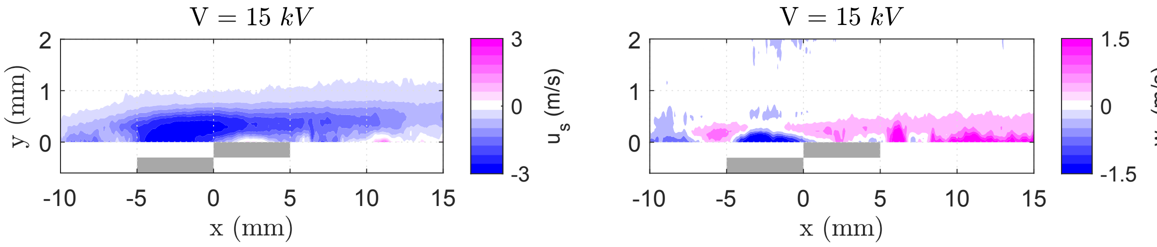

Figure 5.19: Tangential velocity component u_s (left) and perpendicular velocity component w_s (right) contours displaying the difference between the respective carrier frequency (5 kHz) and the clean configuration. Visualised on the curvilinear (ξ, η) grid.

reaches 99% of the free-stream velocity. From the contour images it is clear that the actuator has a strong upstream effect. In the vicinity of the plasma actuator, the generated body force causes the flow to decelerate. Further upstream, the flow instead 'sees' a region of decelerated flow or blockage, and changes path accordingly. The chord locations of interest are ahead of the actuator at x = -2.5, past the actuator at x = 5.0 and further downstream of the actuator at x = 10.0. The obtained velocity profiles for the various carrier frequencies at an applied voltage of 15 kV_{pp} and a velocity of 22 m/s can be found in figure 5.20.

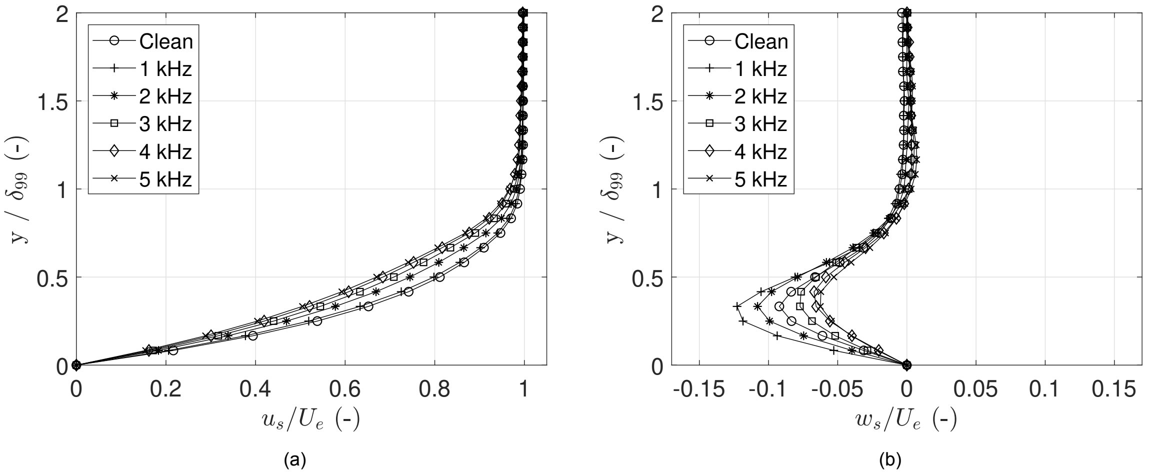

Figure 5.20: u_s (a) and w_s (b) velocity profiles along an inviscid streamline at x = -2.5 as a function of the carrier frequency (15 kV_{pp}).

As can be observed, the tangential velocity component along an inviscid streamline, u_s, decreases as the carrier frequency of the AC-DBD plasma actuator is increased. This is to be expected, as the plasma actuator is inducing a body force or velocity in the direction opposite of the incoming flow. This velocity deficit remains up to the boundary layer edge. The same trend can be observed for the span-wise (w_s) velocity profiles. The largest decrease in amplitude is found to be in the region of 0.3 to 0.5 y/δ_{99}. This location coincides rather well with the centre of the induced velocity jet (and thus the maximum induced velocity) obtained from the mechanical characterisation.

To better visualise the effect of the DBD actuator on the velocity profiles, the profile pertaining to the clean configuration is subtracted from each case where the plasma is active. The resulting velocity profiles can be found in figure 5.21.

Most plasma actuator operating conditions result in a decrease of u_s, however, the lower operating frequencies of 1 kHz and 2 kHz seem to instead increase the cross-flow component. This result is in contradiction with the predicted result, as clearly the actuator is forcing against the cross-flow component and as such, a reduction in u_s is expected for each operating condition. An increase in the cross-flow component indicates a change in the balance between the centrifugal and pressure forces. As

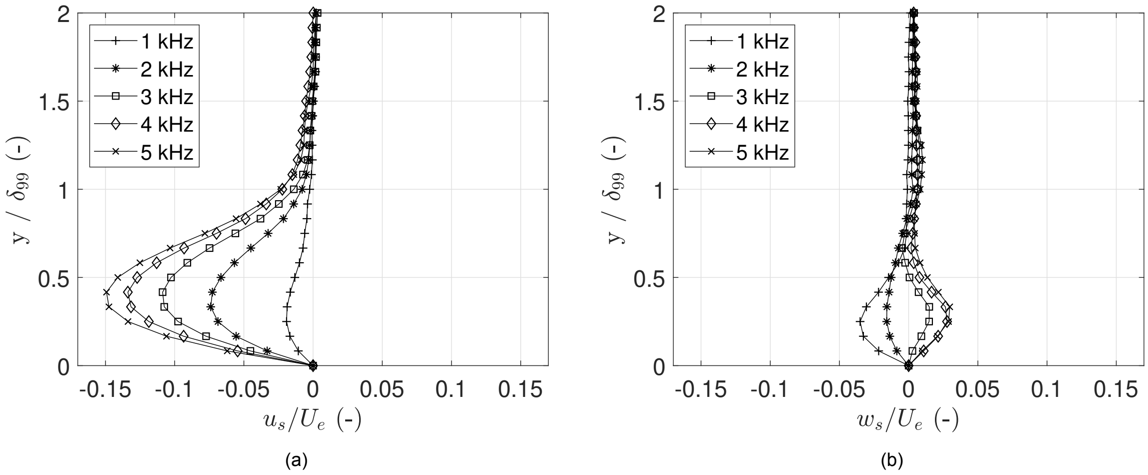

Figure 5.21: Difference with respect to the clean configuration of u_s (a) and w_s (b) along an inviscid streamline at x = -2.5 as a function of the carrier frequency (15 kV_{pp}).

seen during the mechanical characterisation, the plasma is significantly weaker and more non-uniform up to carrier frequencies of 2 kHz in comparison to higher carrier frequencies. Possibly the erroneous behaviour of the actuator at these lower frequencies is responsible for either a strong change in pressure gradient or a direct change in the stability of the base flow. Nevertheless, further investigation is required to understand how the cross-flow component is affected by these lower carrier frequencies, if the increase is in fact genuine and not a measurement or computational error.

Further downstream, the influence of the AC-DBD plasma actuator remains present. As is observed from the contour images in figure 5.19, the velocity deficit decreases downstream of the actuator. This is confirmed by figure 5.22a, which shows smaller differences in the velocity profile for u_s in comparison to figure 5.21, although it is clear the boundary layer edge is located slightly further away from the wall. In contrast, w_s remains largely unaffected, with only a minor increase in the case pertaining to the 5 kHz carrier frequency. This is in agreement with the observations by Yadala et al. [95], where u_s shows a faster transition to the unperturbed clean velocity profile in comparison to w_s. The difference in absolute magnitude between the two velocity components is responsible for this discrepancy, where u_s is an order of magnitude higher than w_s.

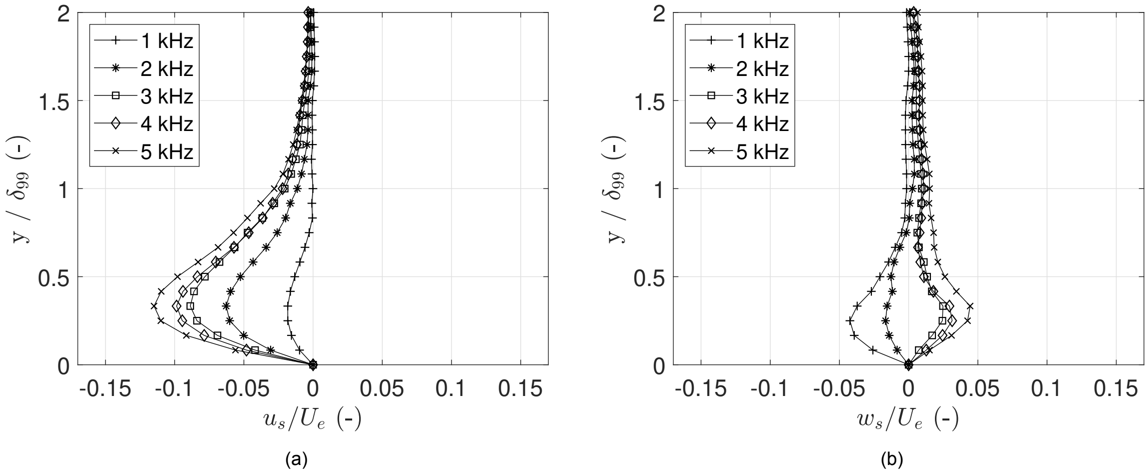

Figure 5.22: Difference with respect to the clean configuration of u_s (a) and w_s (b) along an inviscid streamline at x = -5.0 as a function of the carrier frequency (15 kV_{pp}).

At the most downstream location that is considered, the trend of a decreasing effect on the base flow proceeds to hold, as the magnitude of the velocity deficit further decreases in the case of u_s and w_s. As expected when traversing in the downstream direction, the boundary layer thickens and as a consequence, the influence of the AC-DBD actuator on the velocity profile becomes more pronounced further away from the wall.

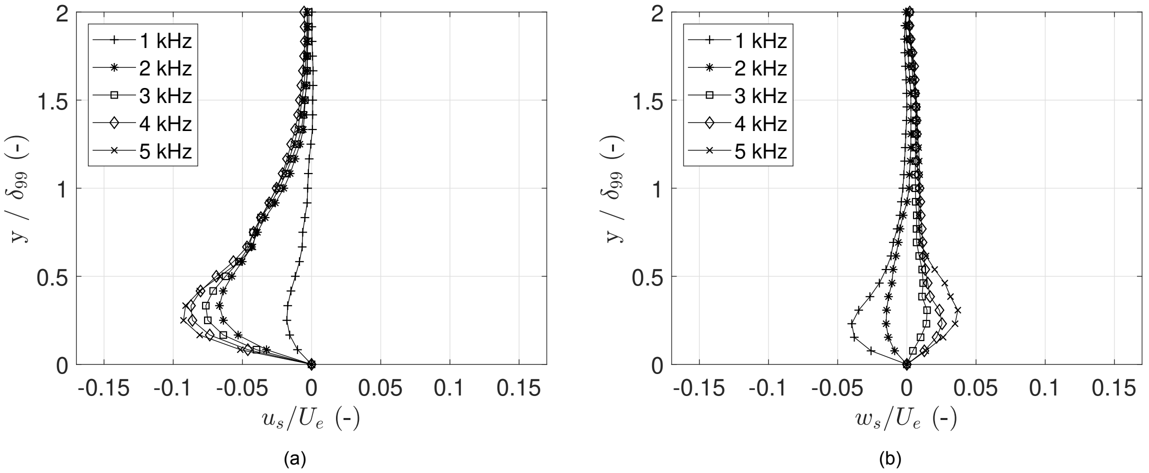

Figure 5.23: Difference with respect to the clean configuration of u_s (a) and w_s (b) along an inviscid streamline at x = -10.0 as a function of the carrier frequency (15 kV_{pp}).

Effect of Applied Voltage

The influence of the plasma actuator on the flow as a function of the applied voltage is presented in figure 5.24. The magnitude of the tangential velocity component u_s is reduced as the voltage is increased. This observation is in agreement with the results obtained from the mechanical characterisation. The magnitude of the velocity component perpendicular to the inviscid streamline, w_s, similarly decreases as the applied voltage is increased. As known from the mechanical characterisation, increasing the voltage is more effective in attaining a higher induced velocity compared to increasing the carrier frequency. Surprisingly, the scenario where the applied voltage is equal to 12 kV_{pp} has a similar effect on the cross-flow component as when the actuator is operated at 14 kV_{pp}. Possibly this can be attributed to the fact that the case of 12 kV_{pp} corresponded to the first measurement of the experimental campaign. Taking into consideration the effect of aging on the performance of the actuator, it is probable that plasma actuator performed significantly better during this first measurement.

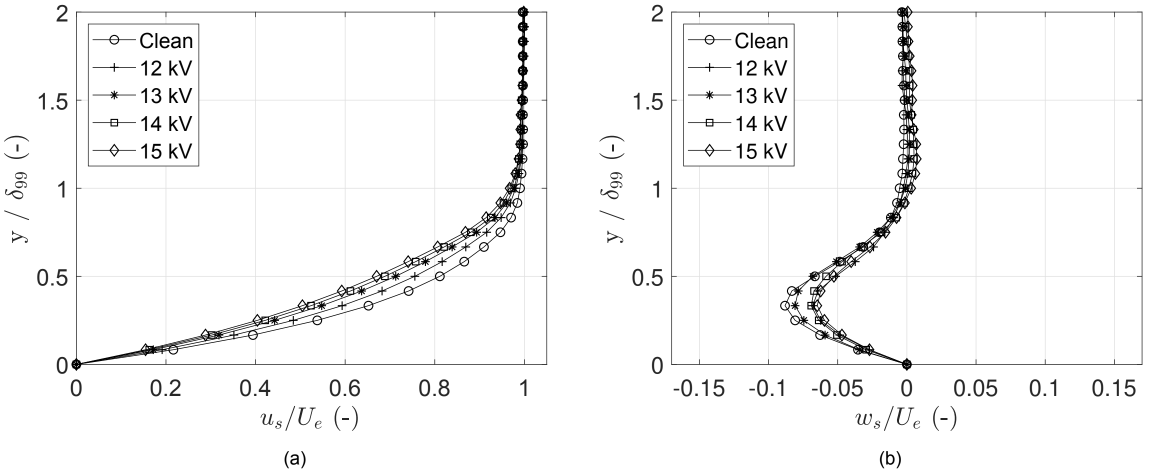

Figure 5.24: u_s (a) and w_s (b) velocity profiles along an inviscid streamline at x = -2.5 as a function of the applied voltage (5 kHz).

The difference in performance for the various plasma actuator operating conditions is more clearly visualised in figure 5.25. The effect of the induced velocity jet on the tangential velocity component u_s is clear, where increasing the applied voltage results in a larger effect. From the mechanical characterisation it is known that the thrust generated by the operating the AC-DBD plasma actuator at 14 kV_{pp} and 5 kHz is similar to that in the case of operating the actuator at 15 kV_{pp} and 3 kHz. This is in agreement with the results presented in figure 5.25b, as the reduction in the cross-flow component is of similar magnitude as presented in figure 5.21. For the sake of brevity, the velocity profiles at the other two chord locations are not presented, however the same trend is visible as is observed from increasing the frequency.

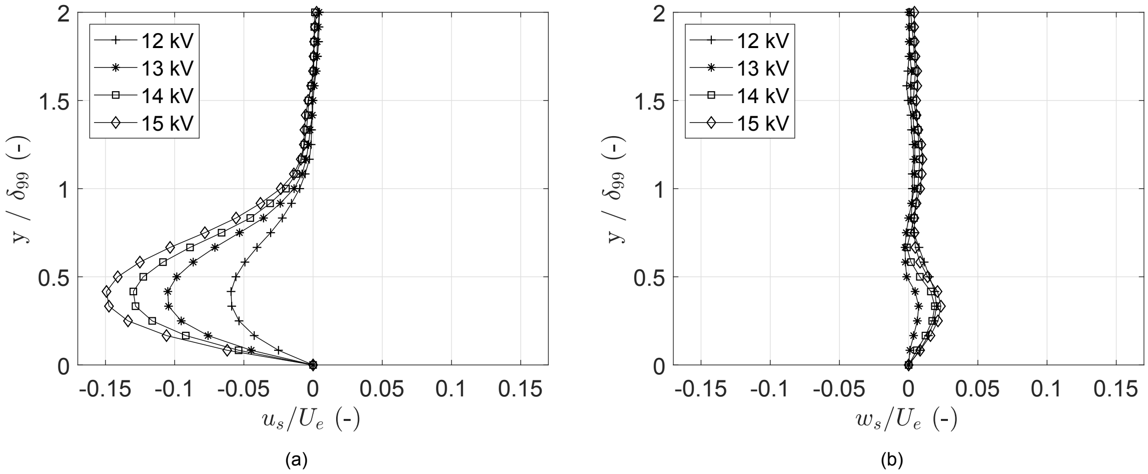

Figure 5.25: Difference with respect to the clean configuration of u_s (a) and w_s (b) along an inviscid streamline at x = -2.5 as a function of the applied voltage (5 kHz).

Effect of Reynolds Number

Lastly, the effect of the free-stream velocity (or Reynolds number) is investigated. It is expected that the authority of the plasma actuator increases as U_∞ is reduced. The baseline case of 22 m/s corresponds to a Reynolds number of approximately 7.59 $\cdot 10^5$. Although measurements have been performed at 16, 18 and 20 m/s, for illustrative purposes only the scenario pertaining to the lowest Reynolds number is considered, as it is found that the same conclusion holds for the higher Reynolds numbers. The free-stream velocity of 16 m/s corresponds to a Reynolds number of approximately 5.51 $\cdot 10^5$, which is a reduction of nearly 210000 or 27.4% when compared to a free-stream velocity of 22 m/s. Only cases pertaining to an applied voltage of 12 kV_{pp} and 15 kV_{pp} are considered to properly assess the effect of a weak and stronger induced velocity jet, as presented in the test matrix in section 4.4. The resulting contours visualising the difference in flow field with the clean configuration can be found in figure 5.26.

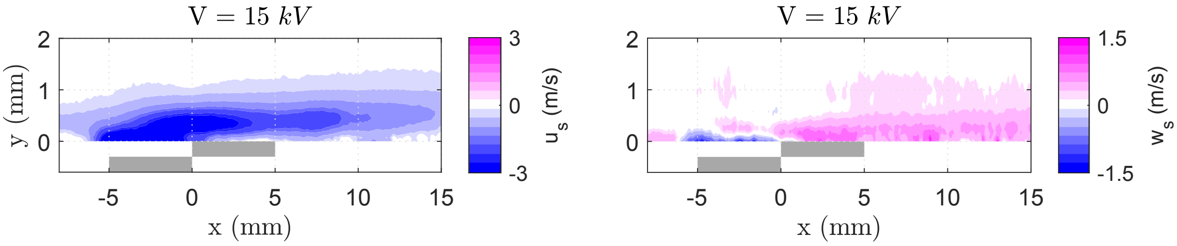

Figure 5.26: Tangential velocity component u_s (left) and perpendicular velocity component w_s (right) contours displaying the difference between the respective carrier frequency (5 kHz) and the clean configuration. Visualised on the curvilinear (ξ, η) grid.

Clearly the plasma actuator its region of influence has grown in the case of u_s and w_s when compared to the scenario where the velocity is equal to 22 m/s. Most notable is the increased height of the wake for both velocity fields. Following the contour images, the stream-wise and span-wise velocity profiles at x = -2.5 can be observed in figure 5.27, whereas the difference with respect to the clean configuration is shown in figure 5.28.

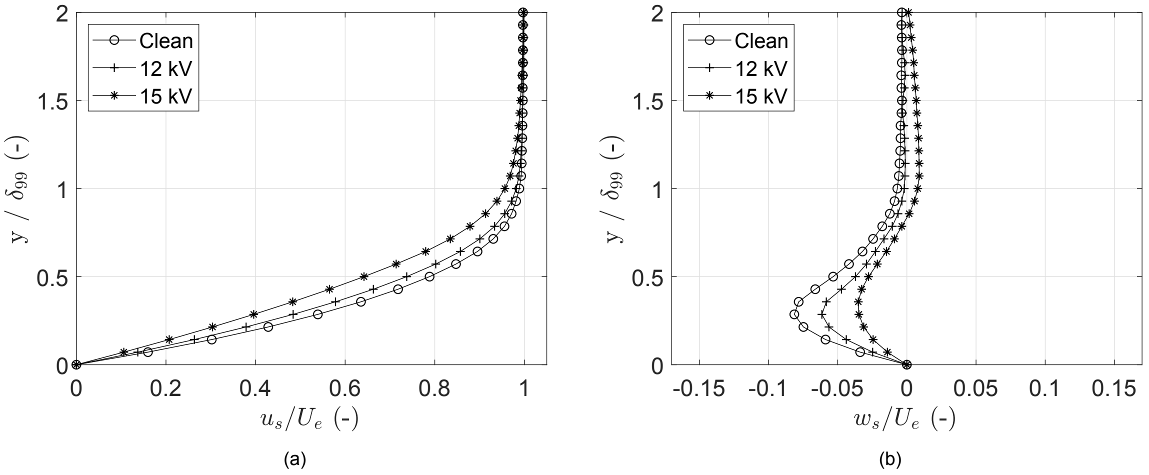

Figure 5.27: u_s (a) and w_s (b) velocity profiles along an inviscid streamline at x = -2.5 as a function of the applied voltage (5 kHz, Re ≈ 5.52 $\cdot 10^5$).

As the velocity profiles have been normalised with U_e, the relative shape and magnitude of the profiles remain comparable to the baseline case of 22 m/s. However, as expected, the plasma-induced velocity jet is now capable of affecting the boundary layer to a larger extent. In the case of an applied voltage of 15 kV, the decrease in u_s and w_s is significant. Interesting to note is the velocity deficit now extends further away from the wall, as the region of influence of the AC-DBD plasma actuator is increased. As the plasma actuator is inducing a velocity jet opposite the direction of the flow, perpendicular to the leading edge, the velocity close to the wall, at the location where the induced velocity is highest, is reduced. However, the flow still has to pass this 'blockage' and consequently the velocity profile is further affected in the wall-normal direction. This effect is therefore magnified for lower free-stream velocities. It should be noted that the boundary layer thickness itself also increases as the Reynolds number decreases.

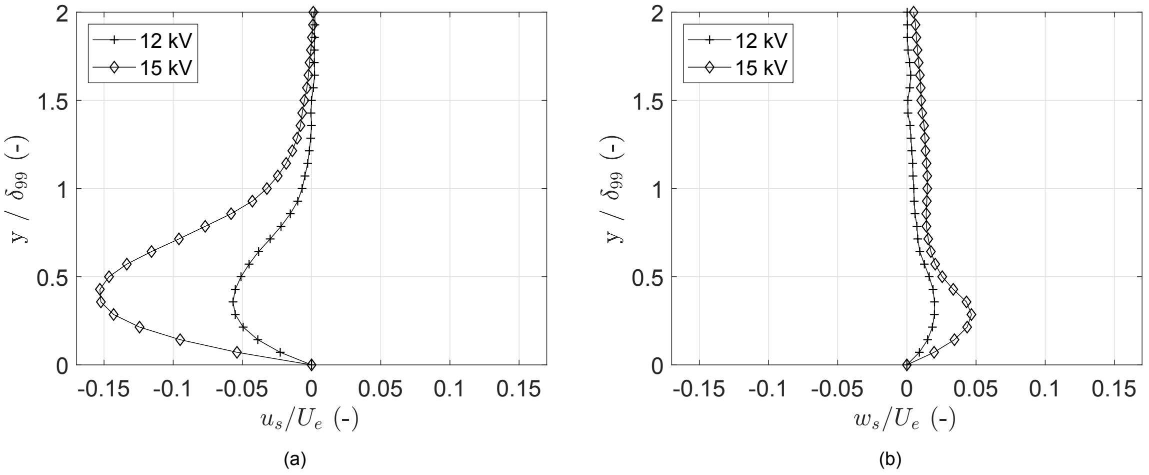

Figure 5.28: Difference with respect to the clean configuration of u_s (a) and w_s (b) along an inviscid streamline at x = -2.5 as a function of the applied voltage (5 kHz, Re ≈ 5.52 $\cdot 10^5$).

When considering the cross-flow component, it can be concluded that the relative magnitude of w_s is comparable to the results obtained from the case where the velocity is equal to 22 m/s. As expected, applying a voltage of 12 kV_{pp} reduces the cross-flow component accordingly. Further increasing the applied voltage to 15 kV_{pp} results in a drastic reduction of the cross-flow velocity, as the amplitude is nearly half when compared to the clean configuration. Furthermore, the more pronounced blockage effect results in a velocity deficit as far as 2 mm from the wall. The velocity profiles at the other chord locations are not presented here, however the previously observed trend persists; traversing in stream-wise direction results in a loss of flow control, such that the stream-wise and span-wise velocity profiles dissipate to their original shape and magnitude. For a lower free-stream velocity, the influence of the actuator is visible for a longer chord-wise distance.

5.4. Cross-Flow Instability Wind Tunnel Experiment Results

Following the preceding wind tunnel experiment that was dedicated to investigating the influence of the AC-DBD plasma actuator on the base flow, the results of the consecutive wind tunnel experiment are presented. As discussed in chapter 4, the PIV measurement plane is now oriented parallel to the leading edge of the wing rather than perpendicular, which allows for the monitoring of the morphology and development of the stationary cross-flow instability. The results obtained from 2D2C-PIV are primarily used in this analysis, although additionally infra-red images are employed to yield information on the state of the flow. The obtained results and outcome are discussed in this section.

5.4.1. Infra-red Thermography

As a qualitative means of studying the effect of the AC-DBD plasma actuator on the primary cross-flow instability, the non-intrusive measurement technique that is infra-red thermography is employed. IR thermography relies on the principle of heat transfer, where in this scenario the wing is actively heated by two halogen lamps and is subsequently cooled down by the flow through the mechanism of convection. The camera is able to acquire the IR radiation emitted by a body through designated sensors. The Reynolds analogy relates the convective heat flux to the velocity gradients, such that a turbulent boundary layer, which is characterised by its higher kinetic energy and wall shear stress, leads to increased values of surface heat transfer in comparison with a laminar boundary layer. The increase in flow displacement and heat transfer then leads to a reduction in surface temperature. The modulation of the surface temperature allows for the identification of laminar and turbulent regions and is therefore an excellent tool to track the displacement of the transition front. The stationary cross-flow vortices modify the base flow in such a way that strong velocity gradients appear, resulting in a span-wise alternating pattern of high and low velocity, which can be identified in the IR images.

As the wing model features a mild favourable pressure gradient, natural transition occurs far downstream and is not captured within the infra-red field of view. Nevertheless, as the IR thermography measurements primarily guide as an addition to the principal 2D2C-PIV measurements, it is sufficient to capture the domain which spans from the leading edge to approximately X/c_X = 0.35.

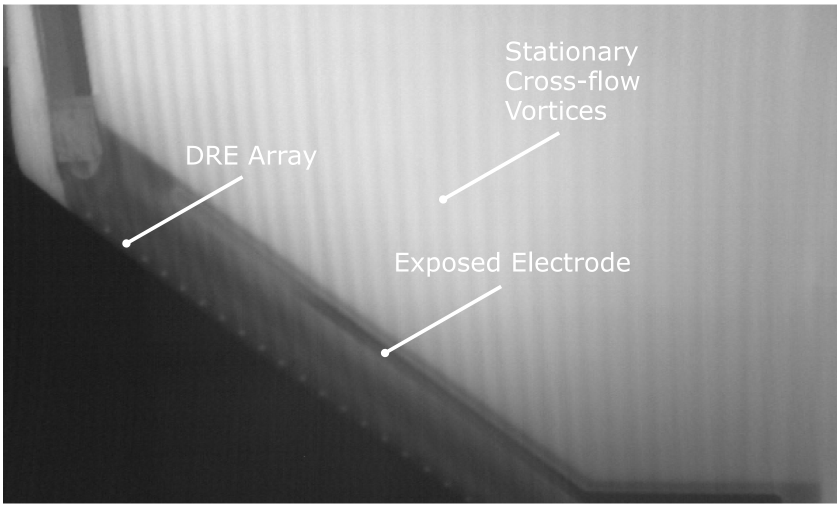

Figure 5.29: Infra-red image of the clean configuration (plasma inactive), clearly showing the stationary cross-flow vortices as a result of the forcing of the 8 mm mode by the 200 μm tall DREs. Temperature ranging from 24.5°C (black) to 29°C (white).

As presented in section 4.5, all measurements have been performed at a free-stream velocity of 22 m/s, or Re_X = 7.59 $\cdot 10^5$. The 100 (raw) IR images are averaged to improve the signal-to-noise ratio and to obtain a single, mean temperature field that is suitable for comparison. In order to observe the effect of the AC-DBD plasma actuator on the flow (or temperature) field, the mean temperature field corresponding to the clean configuration is subtracted from the cases involving the active plasma actuator. Although this method is prone to errors, as it relies on the position of the camera and the field of view to remain consistent throughout the measurements, it is assumed that these discrepancies are sufficiently small such that the general observations and conclusions remain valid. The IR image corresponding to a configuration with the AC-DBD plasma actuator inactive (clean configuration) and 200 μm tall DREs that force the most unstable wavelength of 8 mm is presented in figure 5.29.

Immediately noticeable is the brighter region that extends from slightly past the AC-DBD plasma actuator, corresponding to an increase in temperature with respect to the other elements in the image. As the placed sheets have been painted black, the absorptivity and emissivity is approaching 1, in contrast with the surfaces upstream that have not been painted. Congruently, the black discrete roughness elements can be observed close to the leading edge as bright(er) dots. The presence of the induced cross-flow vortices can be clearly observed from the alternating dark and light streaks, indicating a lower and higher temperature respectively. The darker streaks correspond to the region where the velocity is highest, which is on the downwelling side of the cross-flow vortex.

The effect of the AC-DBD plasma actuator operating at various carrier frequencies can be observed in figure 5.30. Here, the mean temperature field of the clean configuration is subtracted from the IR images corresponding to the different carrier frequencies.

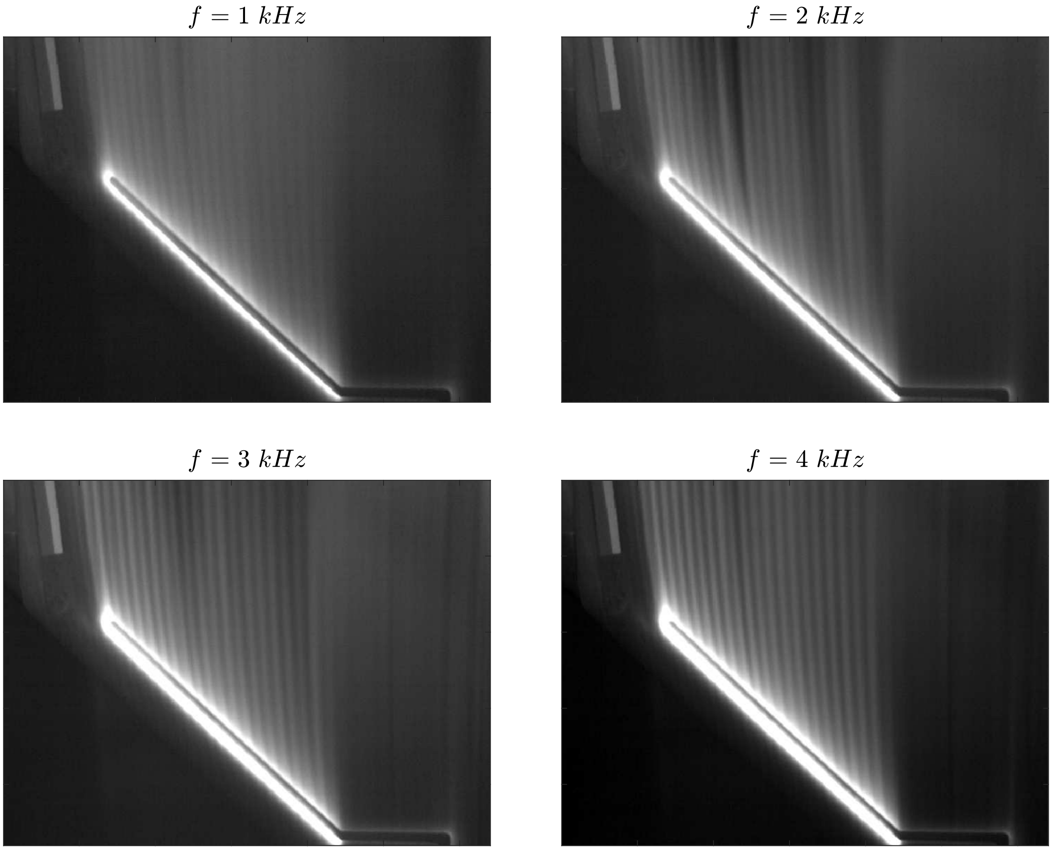

Figure 5.30: Infra-red images corresponding to various AC-DBD plasma actuator carrier frequencies (15 kV_{pp}), obtained by subtracting the clean configuration. Temperature ranging from 0°C (black) to 5°C (white).

In agreement with the mechanical characterisation, increasing the frequency results in a larger region of influence. In this case, the region of influence is characterised by the difference in temperature and as such, increasing the frequency causes the plasma to extend further upstream. More interestingly however, is how the flow field develops as a function of the carrier frequency. For a frequency of 1 kHz, the flow downstream of the actuator is brighter compared to the clean configuration as a result of the heat generated by the plasma. Several darker streaks are located downstream of the actuator, which are indicative of laminar-to-turbulent transition. These streaks, or turbulent wedges, are more prevalent in the case of a carrier frequency of 2 kHz. Turbulent wedges are typically formed in the presence of roughness elements of significant height with respect to the boundary layer. As no turbulent wedges are present when the plasma actuator is inactive, the turbulent wedges are a direct result of the actuation of the DBD actuator. Seemingly, the plasma formation is non-uniform along the width of the actuator, as local high intensity plasma discharges (arcs) are present near the exposed electrode. It is this non-uniformity in the plasma that is responsible for boundary layer transition and consequently the formation of turbulent wedges. Moreover, this non-uniformity is unsteady in time, as turbulent wedges are formed and disappear at various locations along the span. In order to verify this observation, the maximum temperature is located in an instantaneous infra-red image. As stronger plasma discharges are accompanied by a larger increase in temperature, determining the location of the highest temperature should correspond to the location of the strongest plasma discharge. As can be observed in figure 5.31, the maximum temperature (and therefore the strongest plasma discharge) in the infra-red image indeed corresponds to the location where the turbulent wedge is initiated. Increasing the frequency (and power consumption) improves the plasma uniformity such that the turbulent wedges are less prevalent, as can be seen in the case of a carrier frequency of 4 kHz. It should be noted that it is believed that the aging of the actuator might have also played a role in the formation of these unsteady non-uniform discharges, following the conclusions of the study by Aba'a Ndong et al. [1].

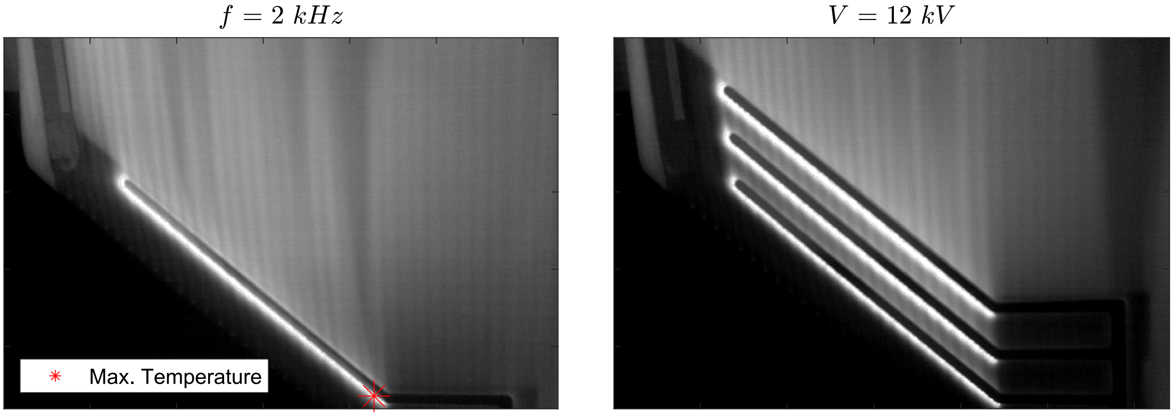

Figure 5.31: Instantaneous infra-red image including the location of the maximum temperature (left, 15 kV_{pp}) and the instantaneous temperature field in the case of three electrode pairs (right, 5 kHz). Temperature ranging from 25°C (black) to 33°C (white).

From these observations it can be concluded that for effective base-flow modification at higher voltages, using the current AC-DBD plasma actuator configuration, the actuator should be operated at sufficiently high carrier frequencies. This ensures a more uniform plasma front such that the formation of turbulent wedges is hindered. Conveniently, these higher frequencies are also desirable from a stability point of view. Operating at a high carrier frequency limits the interference or amplification of lower frequency travelling modes.

The right image in figure 5.31 shows an instantaneous temperature field in the case of three consecutive actuators operated at a voltage of 12 kV_{pp} and a carrier frequency of 5 kHz. Whereas no signs of transition were present for the lower applied voltages of 8 and 10 kV_{pp}, increasing the voltage up to 12 kV_{pp} results in transition downstream of the last electrode pair. In contrast with the single actuator, transition is more gradual and thus it is expected that a different physical mechanism is responsible. First of all, more sources of unsteadyness are introduced as more AC-DBD plasma actuators are present. These low frequency fluctuations are able to amplify already present instabilities and travelling waves, resulting in early transition. On the other hand, each time the flow passes an actuator, its velocity profiles are reduced and as a direct consequence its stability characteristics change. It should be noted that the actuators effectively obstruct the upstream flow close to the wall, inevitably increasing the boundary layer height. It is unsure which mechanism is responsible for the observed behaviour and further investigation is required. Nevertheless, there is a clear upper boundary for which base-flow modification is effective, analogous to transition triggered by excessive suction or blowing.

The effect of the AC-DBD plasma actuator operating at various applied voltages can be observed in figure 5.32. No turbulent wedges are observed, which is in favour of the presented hypothesis, which notes that the plasma front becomes more uniform as the frequency is increased. As expected, the effect on the flow field increases as the applied voltage is increased. Although not immediately noticeable, the cross-flow vortices and the corresponding alternating streaks of bright and dark regions have shifted outboard with respect to the clean configuration. Whereas this effect is not as evident in the case of an applied voltage of 12 kV_{pp}, the scenario where the applied voltage is equal to 15 kV_{pp} shows a significant shift. It is clear that the actuation of the AC-DBD plasma actuator has an influence on the local balance of the pressure and inertial forces close to the leading edge. Potentially, as the plasma actuator reduces the cross-flow component along an inviscid streamline, the axis of rotation along which the stationary cross-flow vortex is formed shifts accordingly. The cross-flow vortices then develop as usual from their 'new' shifted equilibrium position. As this effect is evident from both an increase in frequency and voltage, the shift in position of the CFVs is most likely caused by the reduction of the cross-flow component rather than a result of the introduced low frequency travelling waves.

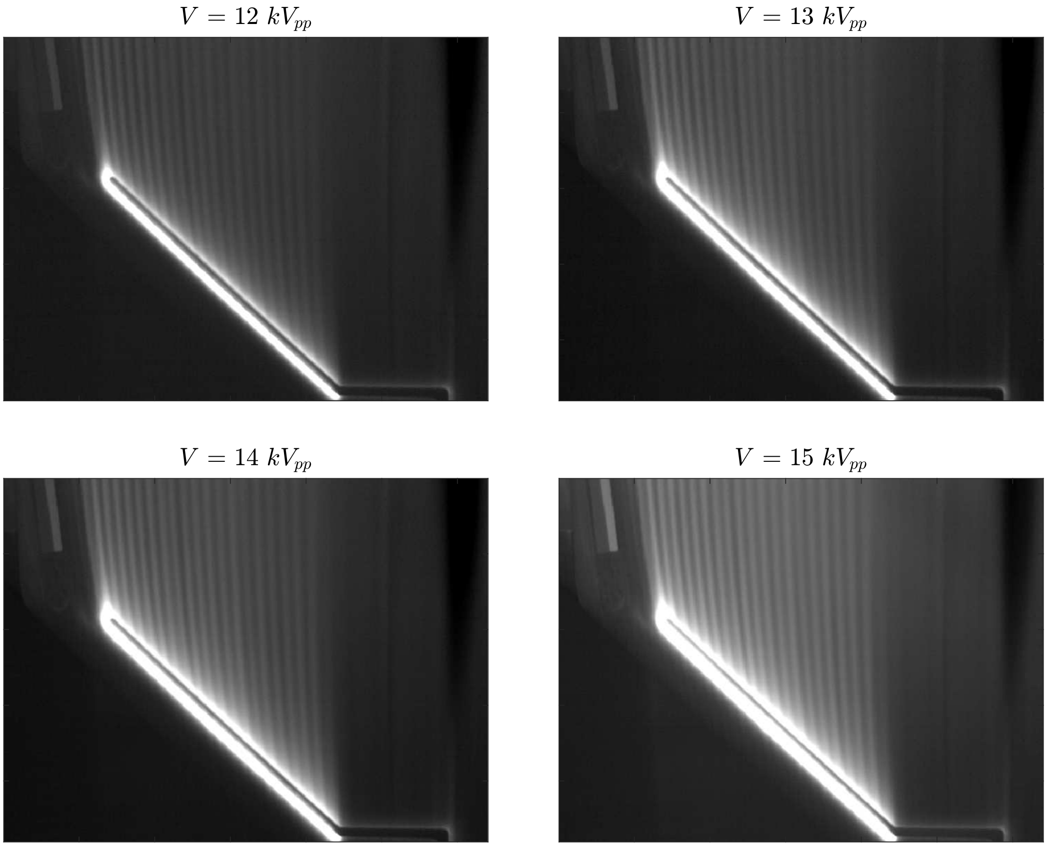

Figure 5.32: Infra-red images corresponding to various AC-DBD plasma actuator applied voltages (5 kHz), obtained by subtracting the clean configuration. Temperature ranging from 0°C (black) to 5°C (white).

5.4.2. Planar PIV

As presented in section 4.5, various combinations of DRE geometries and AC-DBD plasma actuator operating conditions have been tested. The baseline configuration features DREs that force the (critical) 8 mm mode and are 200 μm tall (L2). The other configurations feature a reduction in DRE height to 100 μm and a reduction and increase in spacing to 6 and 10 mm, respectively. As it is found the 6 and 10 mm spacing yield similar results as for the baseline configuration of 8 mm, which confirms the robustness of the AC-DBD plasma actuator operating according to the base-flow principle, only the latter will be discussed. Nevertheless, the influence of the DRE height and the placement of three consecutive actuators is briefly presented due to their slight differences with the baseline configuration. First, the stream-wise development of the cross-flow vortices is investigated for the clean configuration, after which the influence of the plasma actuator is quantified.

Raw Data Processing & Uncertainty Quantification

The particle images are processed in DaVis 10.1, where initially a shift-and-vibration correction is applied, after which the background noise is removed by subtracting a constant pixel amount. The images are then cross-correlated through a multi-pass vector calculation process with an initial window size of 48 × 48 pixels and a final window size of 12 × pixels with a 50% overlap. Finally, the uncertainty as well as the mean velocity field and standard deviation are computed.

The uncertainty is obtained in a similar matter as was done for the previous experiments. The uncertainty is obtained directly from DaVis 10.1, which calculates the statistical uncertainty using the formulas presented in chapter 3. A typical uncertainty field is shown in figure 5.33.

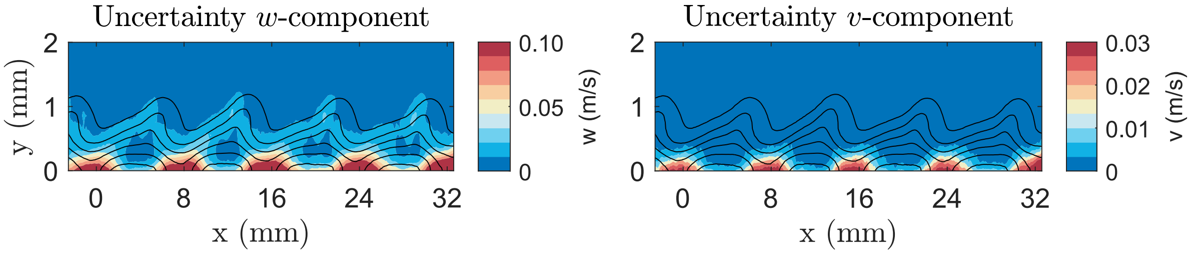

Figure 5.33: Uncertainty field for the clean configuration (8 mm spacing, L2 DRE) at a chord location of X/c_X = 0.20, of which the values are representative for the complete experiment.

It should be noted that the presented uncertainty is rather small in comparison with the free-stream and edge velocity; an uncertainty of 0.10 m/s in comparison to a free-stream of 22 m/s is approximately 0.45%, whereas the lower local edge velocity of approximately 15.6 m/s leads to an uncertainty of 0.64%. Although this low statistical uncertainty indicates a high confidence in the results, it should be noted that other (experimental) factors, such as the actuator life time, should still be taken into account in the analysis.

Stream-wise Development of Stationary Cross-Flow Instability

The mean total velocity contours for the clean configuration at several stream-wise chord locations are presented in figure 5.34. In this case, the total velocity is defined as the resultant velocity component in the measurement plane, such that $U = \sqrt{w^2 + v^2}$. The velocity is non-dimensionalised with respect to the local external velocity U_e, which is equal to the value of U at $y = \delta_{99}$. These are presented as seen from the camera location (downstream). The same procedure as described in section 5.3 is followed to determine the location of the wall, where 50 raw images are averaged and a line is fitted through the points of maximum intensity on the reflection at the wall. The domain is then rotated such that the wall is horizontal. The y-axis is shifted accordingly, such that $y = 0$ is located at the wall. For comparison, the location of the wall is further approximated by extrapolating the span-wise averaged w velocity profile to zero, which has shown to yield a similar result. For this reason, the former method is applied due its simplicity and robustness.

At $x/c = 0.10$, the span-wise modification of the boundary layer can already be observed. The stationary cross-flow instability manifests itself as a sequence of well-developed and strong cross-flow vortices that are spaced 8 mm apart. On the upwelling side of the vortex, low momentum flow is extracted from near the wall and transported up to regions higher in the boundary layer. On the downwelling side of the vortex, high velocity flow is ejected from higher regions in the boundary layer down towards the wall, causing large flow shears. As expected, the height of the boundary layer as well as the cross-flow vortices increase in stream-wise direction.

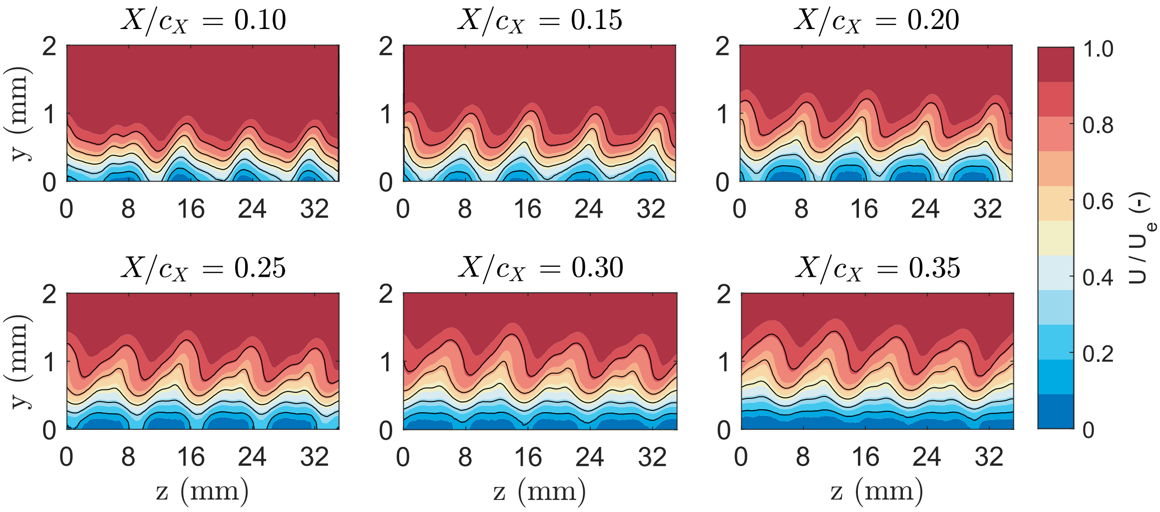

Figure 5.34: Mean total velocity U contours for the clean configuration (plasma inactive, DRE spacing 8 mm, 200 μm tall) at various chord locations. The velocity fields are presented from downstream.

In order to study the distribution of the various span-wise modes, a spatial Fourier decomposition is performed. At each y-location, the span-wise disturbance velocity signal is transformed to the (spatial) frequency domain, which allows for the reconstruction of the disturbance profiles for various wavelengths. The resulting power spectral densities as a function of the wavelength for the clean configuration at a chord location of 35% can be found in figure 5.35.

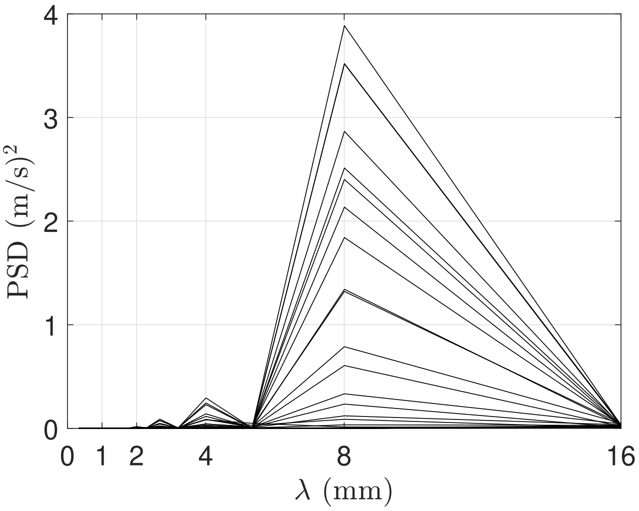

Figure 5.35: Dominant wavelengths as obtained from a domain spanning three cross-flow vortices at a chord location of x/c = 0.35 for the clean configuration, where the PSD is calculated by FFT(w_{rms}^2). Each line corresponds to a single y-location.

As expected, the most dominant wavelength is equivalent to the wavelength forced by the DREs, which is the 8 mm mode. The peaks at 4 mm and 2.67 mm are the second and third harmonic, respectively. Upstream chord locations reveal a similar trend, where the 8 mm mode is dominant and the harmonics are of lesser amplitude. Nevertheless, in agreement with LST, the lower wavelength harmonics grow faster and saturate earlier and can therefore have an effect on the development of the stationary cross-flow vortices, which must be considered in the following analysis. Aside from the mean flow distortion that is caused by the cross-flow vortices, the velocity fluctuations within the boundary layer are of equal interest. As can be observed in figure 5.36, the velocity fluctuations appear in distinct regions.

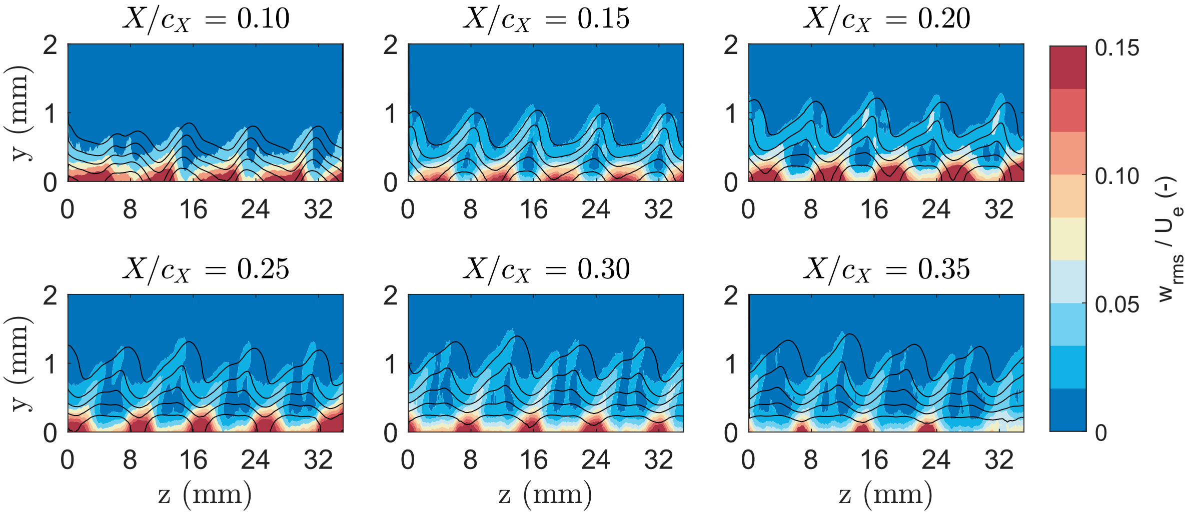

Figure 5.36: Mean span-wise standard deviation w_{rms} contours for the clean configuration (plasma inactive, DRE spacing 8 mm, 200 μm tall) at various chord locations. The velocity fields are presented from downstream.

Fluctuations very close to the wall are a result of travelling cross-flow modes. Although the low turbulence intensity of the wind tunnel and the use of discrete roughness elements ensure the dominance of the stationary cross-flow instabilities, the travelling waves cannot be avoided in an experimental framework. At x/c = 0.15 and further downstream, the mean flow distortion causes a particular topology of the velocity fluctuations. Large velocity fluctuations are present near the wall, in between consecutive vortices. These velocity fluctuations are a direct result of the downwelling motion of the vortex, causing large velocity gradients close to the wall. With respect to the stationary cross-flow vortices, three distinct velocity fluctuation types can be established. As described by Malik et al. [51], the type-I and type-II (or z and y) modes appear at the outer side of the upwelling low momentum flow and on top of the cross-flow vortex, respectively, whereas the type-III mode is a result of the interaction between the stationary cross-flow vortex and travelling cross-flow waves. As an example, each instability is well-defined in the standard deviation contour for x/c = 0.20.

Interestingly, one would expect the velocity fluctuations to increase in stream-wise direction until transition occurs, after which the fluctuating energy is redistributed and the strength of the coherent structures is dampened. However, in this case, the velocity fluctuations decrease beyond x/c = 0.20, with no evidence of transition.

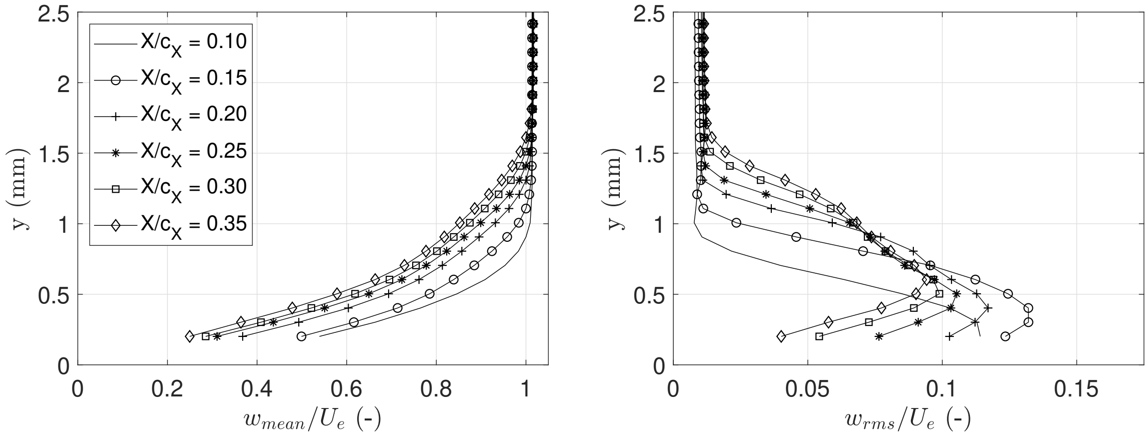

(a) (b)

Figure 5.37: Span-wise averaged velocity w_{mean} (a) and standard deviation w_{rms} (b), non-dimensionalised with the local external velocity U_e for several chord locations (plasma inactive).

To study this discrepancy, the span-wise average and standard deviation are computed for each y-location from the mean flow field at several chord locations. The resulting profiles are presented in figure 5.37. These are obtained by considering a span-wise domain that includes three full cross-flow vortices (24 mm) and are non-dimensionalised with the local external velocity U_e. The velocity profiles are resolved up to 0.2 mm from the wall. The modulation of the mean flow is evident, as the location of the boundary layer edge moves up in wall-normal direction and the velocity in the boundary layer decreases when traversing in stream-wise direction. The disturbance or mode shape profiles yield insight in how the cross-flow instability develops in stream-wise direction. The maximum amplitude increases from x/c = 0.10 to x/c = 0.20, but then decreases for subsequent chord stations. Interesting to note is the change in amplitude and shape for these chord locations. The second maximum in the disturbance profile, first seen for x/c = 0.20, is related to the size of the cross-flow vortex and the rolling over of the related lobe structure. Typically the presence of such a local maximum is an indication of the onset of the secondary instability modes, as described by Haynes & Reed [26], after which transition quickly follows.

To study the development of the cross-flow vortex in stream-wise direction, the amplitude is tracked according to two metrics; the maximum amplitude and the integral of the disturbance profile in wall-normal direction up to the boundary layer edge. The equations pertaining to each metric have been presented in chapter 3. In this analysis, both the w and v velocity components are considered. The result can be found in figure 5.38.

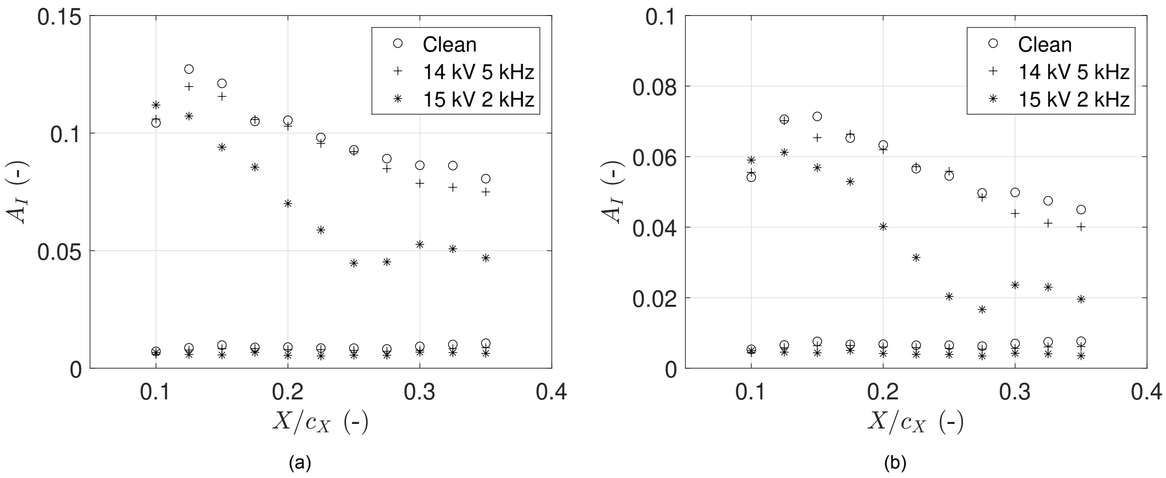

(a) (b)

Figure 5.38: Non-dimensional amplitudes computed from the maximum metric (a) and the integral metric (b) for both the w velocity component (upper values) and the v velocity component (lower values).

As expected, the obtained magnitude varies slightly between the two methods. Error bars are not shown here, considering the small uncertainty would result in error bars that are the size of the marker itself. Nevertheless, a distinct trend can be observed; the mean amplitude of the stationary cross-flow vortex decays after an initial growth up to x/c = 0.125. This is in contradiction with predictions from linear stability theory, which state that the cross-flow vortices grow in amplitude until a level of saturation is reached, after which secondary instabilities initiate the transition process. As the wing is a scale model of the leading-edge region of the ’66018M3J’ wing, as presented by Serpieri & Kotsonis [81], the metrics used here could be unrepresentative or invalid in the case of non-linear interactions within this region. The observed amplitude development and mode shape profiles are consistent with the results presented by Downs et al. [15] in their article on transient growth and transition induced by random distributed roughness. As discussed by Downs et al., the discrete roughness elements are responsible for a rivalry between the deformed steady flow, which rapidly relaxes towards the Blasius condition through the stabilising mechanism of the steady flow, and the growing instabilities of the distorted flow. Downstream of the roughness elements, they note a reduction in the maximum amplitude of the disturbance profile and a broadening of the profile in wall-normal direction, in agreement to what is observed in this experiment. Moreover, the disturbance energy (expressed as the integral of the disturbance velocity squared) initially grows, after which it decays in the downstream direction. This trend is once more similar to the observed downstream amplitude development of the cross-flow instability.

It should be noted that although the characteristics described by Downs et al. [15] fit the obtained results, it is not clear whether the DREs indeed cause a distortion of the flow resulting in this transient behaviour. If this were the case, it is expected that once the disturbances are relaxed by the free-stream, the stationary CFI commences to grow as predicted by LST. To confirm this hypothesis, measurements at more downstream chord stations are required for this DRE configuration (λ = 8 mm, L2). Additionally, other mechanisms could be responsible for the observed reduction in the stationary CFI amplitude. Although great caution has been taken to limit the roughness of the black paint layer, which is present from x/c = 0.125, the introduced roughness could have been of influence on the developing boundary layer through the receptivity process. Furthermore, as described by Kurz & Kloker [42] in their DNS study on the mechanisms of flow tripping by DREs in a swept-wing boundary layer, once the flow passes the discrete roughness elements, two vortex pairs are formed. The vortices with the same sense of rotation as the cross-flow persevere, whereas the other vortices are suppressed and merge slowly with the main vortex. Depending on the chord-wise extent for which these vortices are present, they are included in the calculations of the amplitude growth. It is clear that further analysis is required to fully understand the receptivity process and the CFI development over the swept wing for these DRE elements of 200 μm tall.

Nevertheless, the influence of the AC-DBD plasma actuator on the primary cross-flow instability can still be investigated. Figure 5.38 clearly shows a difference in amplitude for the clean configuration and the two cases where the plasma actuator is active. As first observed in the infra-red images, operating the DBD actuator at a carrier frequency of 2 kHz results in the formation of unsteady turbulent wedges. It can therefore be concluded that the drastic reduction in amplitude for the carrier frequency of 2 kHz is due to the presence of turbulent wedges and the associated dampening of the structures, rather than by actual suppression of the cross-flow component. Instead, the other case for which the plasma actuator is active (14 kV_{pp}, 5 kHz) shows a small reduction in the cross-flow amplitude for most chord locations. This small reduction in amplitude is confirmed by the disturbance profiles as presented in figure 5.39. When compared to the clean configuration (figure 5.37), the maximum amplitude at more downstream chord stations is reduced considerably. Interesting to note is that the second maximum, which indicates the characteristic lobe structure, is less dominant. This can be an indication that the growth rate is halted, as the formation of the lobe and its rolling motion is delayed in stream-wise direction. On the other hand, the disturbance profile is fuller, indicating lower velocities further away from the wall in comparison to the clean configuration. These lower velocities, which are most likely caused by a combination of the induced velocity and lower frequency modes of the actuator, could have an unfavourable effect on the further development of the cross-flow instability.

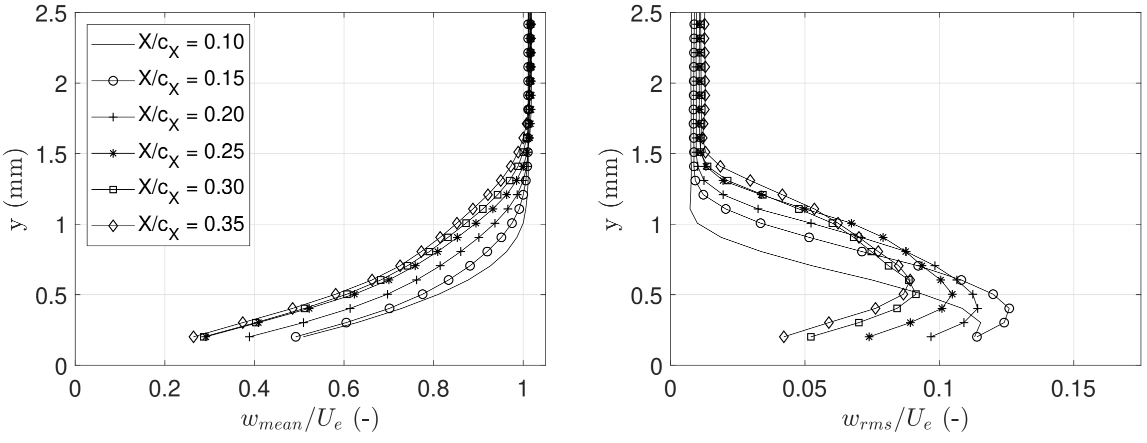

(a) (b)

Figure 5.39: Span-wise averaged velocity w_{mean} (a) and standard deviation w_{rms} (b), non-dimensionalised with the local external velocity U_e for several chord locations (14 kV_{pp}, 5 kHz).

Figure 5.40 visualises the influence of the plasma actuator operated at a voltage of 14 kV and a frequency of 5 kHz on the total velocity field U.

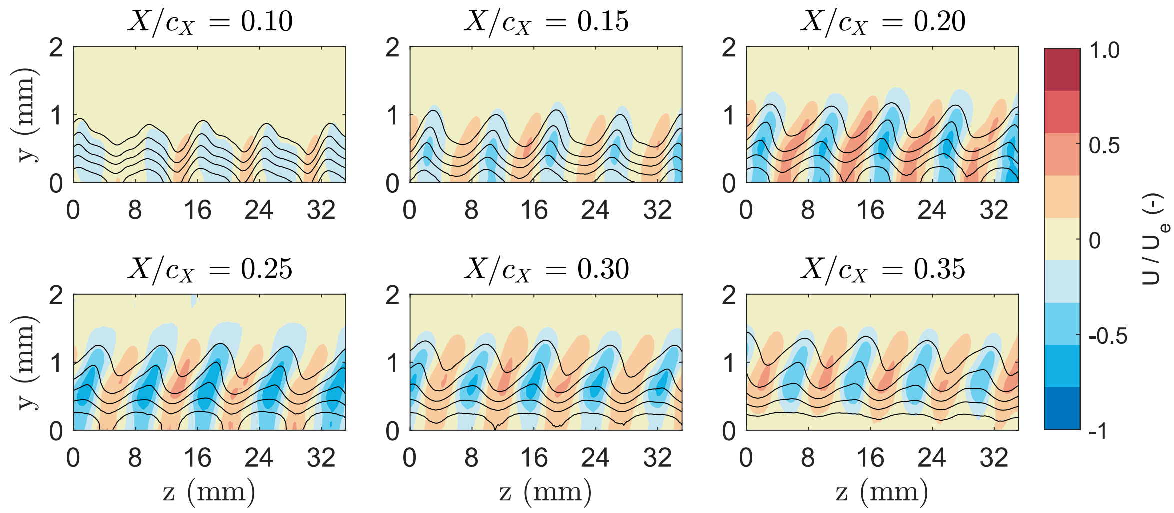

Figure 5.40: Total velocity U contours normalised with the mean local external velocity U_e (14 kV_{pp}, 5 kHz). The clean configuration is subtracted to show the difference. The mean velocity is visualised by the black iso-lines (5 levels from 0 to 1). The contours are presented from downstream.

The topology of the flow field is given by the black iso-lines of constant velocity. It is clear the induced body force results in a shift of the vortex structures, as the lower-velocity lobe has moved towards the right in the field of view. It should be noted that this shift is not a pure translation, as a pure vortex translation would result in blue and red regions of equal size, which is clearly not the case in figure 5.40. Instead, it is thought the shift is the result of a reduction in the cross-flow component, which yields a new equilibrium situation. In this new equilibrium situation, the vortices are shifted with respect to the clean configuration, and of lower amplitude due to the reduced cross-flow component. Considering the contours are presented as from downstream, the shift is actually in the same direction as the direction in which the cross-flow vortex is developing. As the cross-flow component is pointing to the inside of the wing, an outboard shift of these vortices indicates a direct reduction of the cross-flow component. The width of the red and blue regions pertaining to higher and lower velocities respectively remains similar when traversing in chord-wise direction, indicating that the 8 mm mode remains the dominant wavelength and the vortices develop similarly as observed in the clean configuration.

Effect of AC-DBD Plasma Actuator on Stationary Cross-Flow Instability

In addition to the presented measurements for a notable amount of chord stations, measurements have been conducted at an upstream (x/c = 0.15) and downstream (x/c = 0.275) chord location for several AC-DBD plasma actuator operating conditions to study the influence of the actuator on the primary cross-flow instability. The results for the configuration featuring critically spaced (λ = 8 mm) DREs with a height of 200 μm are presented here.

It has been shown that operating the AC-DBD plasma actuator at a carrier frequency of 2 kHz and a voltage of 15 kV_{pp} results in the presence of turbulent wedges along the span of the wing. Instead, operating the plasma actuator at a higher frequency, 5 kHz, and a slightly lower voltage (14 kV_{pp}), resulted in a (seemingly) genuine reduction of the cross-flow component and an associated reduction in CFV amplitude. To assess how the plasma actuator affects the cross-flow vortex amplitude for various operating conditions at the two aforementioned chord locations, the disturbance profiles are constructed and consequently the amplitudes are computed through the integral in wall-normal direction up to the boundary layer edge. To give an indication of the resulting flow field for each case, the velocity field pertaining to the clean configuration at x/c = 0.275 and several contours of the total velocity as a function of the carrier frequency are presented in figure 5.41.

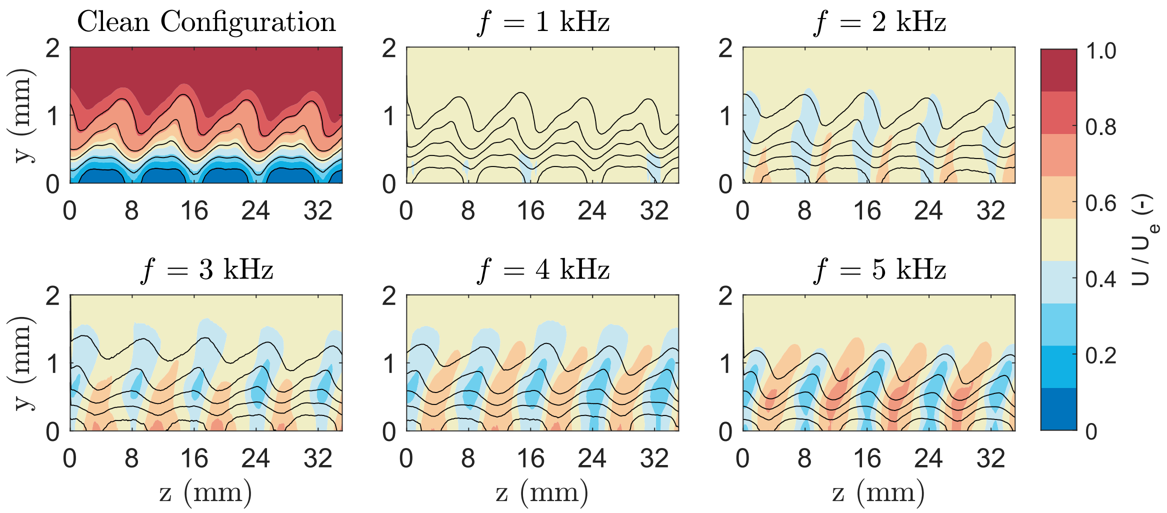

Figure 5.41: Total velocity U contours normalised with the mean local external velocity U_e (14 kV_{pp}, 5 kHz). The clean configuration is subtracted to show the difference. The mean velocity is visualised by the black iso-lines (5 levels from 0 to 1). The presented colorbar is associated with the clean configuration; the colorbar relevant to the other flow fields features the same colours and instead ranges from -1.0 to +1.0.

It should be noted that the case pertaining to a carrier frequency of 1 kHz has little effect on the cross-flow vortices. This is to be expected, considering the low induced body force and velocity as computed from the mechanical characterisation, as presented in section 5.2. Increasing the carrier frequency up to 2 or 3 kHz yields a shift of the structures, with an associated reduction in velocity near the wall. The reduction of velocity near the wall appears to be the result of the introduced travelling modes by the actuator. It is known that the lower carrier frequencies are capable of introducing unsteady turbulent wedges, which cloud the resulting mean velocity field. Further increasing the frequency to 4 kHz yields a greater shift and reduces the observed phenomena, whereas the frequency of 5 kHz shows limited signs altogether. The difference between the peaks and valleys of the relevant vortices has a direct influence on the CFV amplitude according to the presented metrics. It is clear this difference is reduced for most of the frequencies presented here. Furthermore, the regions colored in blue indicate a reduction in velocity, which is consistently of larger size and magnitude compared to the blue regions, resulting in a net span-wise velocity reduction. The CFV amplitudes computed according to the wall-normal integral can be found in figure 5.42.

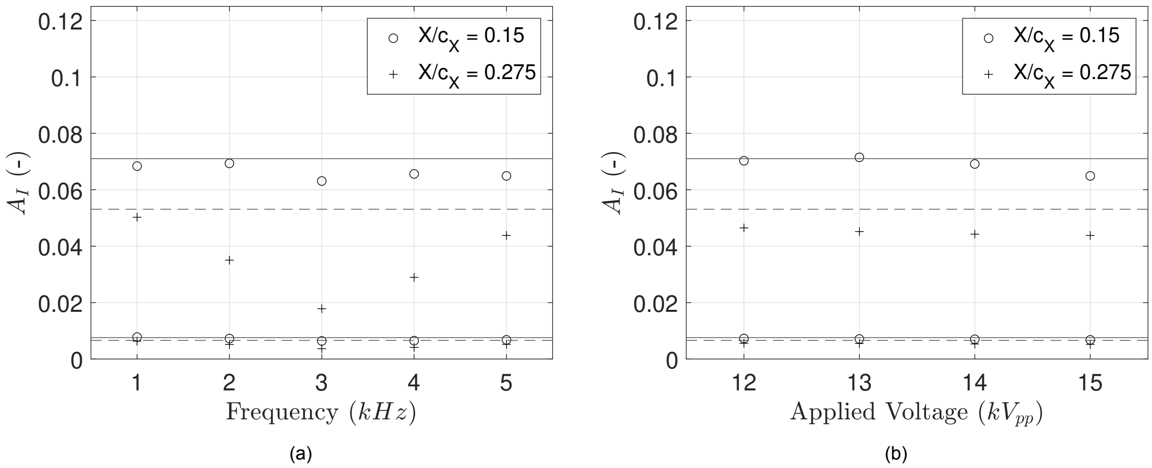

(a) (b)

Figure 5.42: Non-dimensional amplitudes computed from the integral metric for both the w (upper values) and the v velocity component (lower values) as a function of the carrier frequency (a) and the applied voltage (b), including the clean configuration at x/c = 0.15 (–) and x/c = 0.275 (- -).

The black line indicates the amplitude magnitude for the clean configuration at x/c = 0.15, whereas the dashed line represents the amplitude of the clean configuration at x/c = 0.275. In agreement with the contours presented in figure 5.41, the amplitude is consistently smaller than that computed for the clean configuration at x/c = 0.275. For the upstream chord location, nearly all cases show a slight reduction in the CFV amplitude, although the mechanism by which this reduction is achieved is not equal. As discussed, the lower frequencies have the potential to induce turbulent wedges and amplify travelling waves, which redistribute the fluctuating energy and dampen the coherent structures, as observed in figure 5.41 from the flattening of the cross-flow structures. In contrast, the case pertaining to a higher carrier frequency of 5 kHz reduces the amplitude of the stationary CFVs while not significantly affecting the topology. The applied voltage generally behaves in a more predictable manner, with an increase in voltage resulting in a decrease in CFV amplitude below the level of the clean configuration.

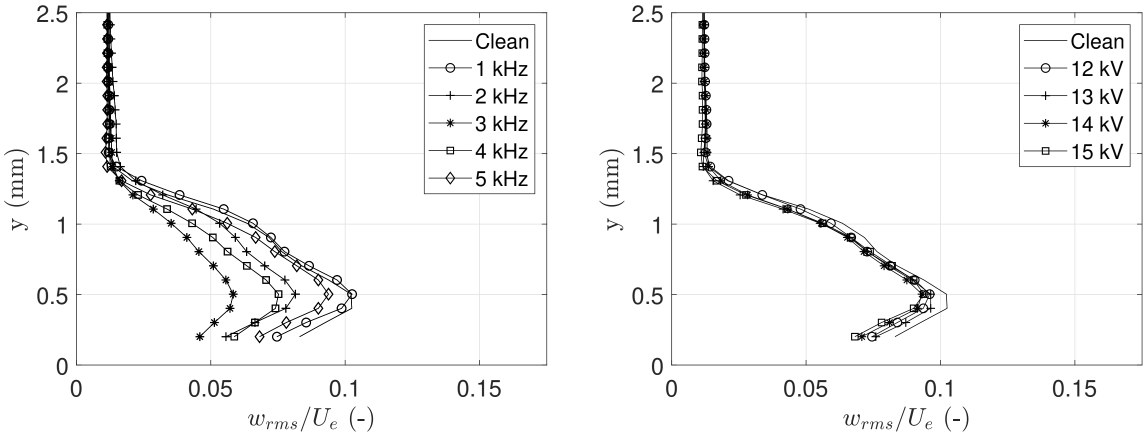

(a)

(b)

Figure 5.43: Span-wise averaged standard deviation w_{rms} for various carrier frequencies (15 kV_{pp}) (a) and voltages (5 kHz) (b) normalised with the local external velocity U_e for a chord location of x/c = 0.275.

Regressing to the disturbance profiles, as presented for the various carrier frequencies and voltages in figure 5.43, the influence of the AC-DBD plasma actuator and trend as observed in figure 5.42 is evident. Whereas the different frequencies result in a wide range of mode shapes, the profiles for the applied voltages instead are in close proximity to each other. This confirms that the performance of the DBD actuator and the associated uniformity of the plasma front is of significant influence on the development of the primary cross-flow instability.

Effect of Discrete Roughness Element Height

The influence of the AC-DBD plasma actuator on the primary CFI has been further investigated for the case of weaker stationary cross-flow vortices. Rather than using DREs of 200 μm tall, a single layer of black PVC foil of approximately 100 μm thick is used to cut the cylindrical elements. As the elements are less tall, the introduced perturbation is of smaller amplitude, such that there is a weaker initial modulation of the base-flow.

This is confirmed in figure 5.44, which presents the development of the stationary CFVs as a function of the stream-wise chord location. At x/c = 0.10, the effect of the DREs can already be observed from the weak modulation by the 8 mm mode in the vicinity of the wall. As the vortices grow in amplitude following linear stability theory, a stronger modulation of the base flow is present from approximately x/c = 0.25.

This modulation can be directly observed from the span-wise averaged velocity profiles and to a greater degree from the disturbance profiles as presented in figure 5.45. As expected, the mean velocity reduces as a function of the stream-wise chord station. Furthermore, the maximum non-dimensional amplitude of w_{rms} is approximately half of the amplitude computed for the DREs of the type L2. There is no evidence of a secondary maximum in the disturbance profiles, indicating the formation of the lobe

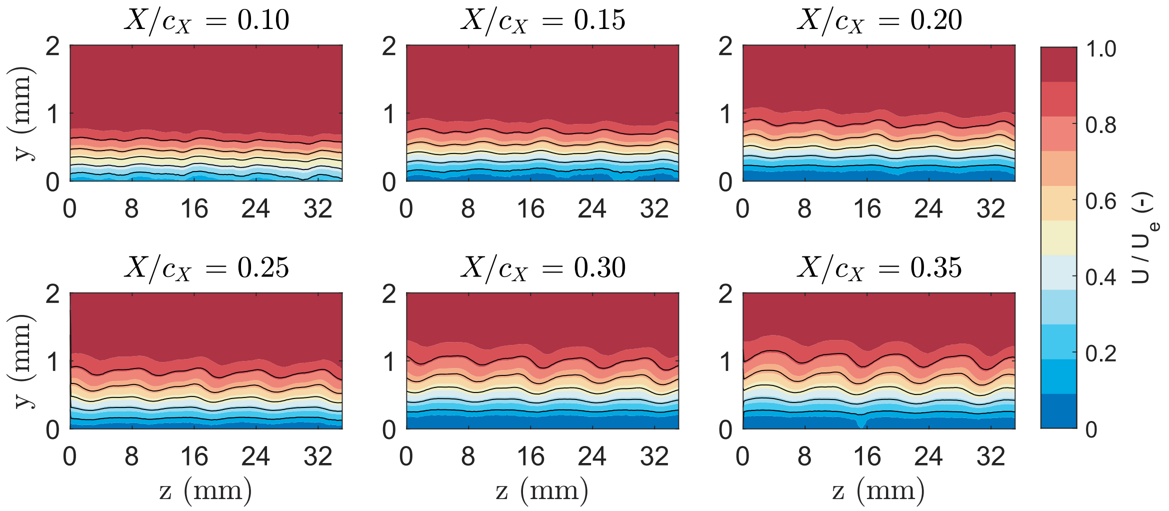

Figure 5.44: Mean total velocity U contours for the clean configuration (plasma inactive, DRE spacing 8 mm, 100 μm tall) at various chord locations. The velocity fields are presented from downstream.

structure and the onset of any secondary instabilities has not occurred yet at the most downstream measured chord station. Interestingly, the maximum amplitude of w_{rms} increases consistently in agreement with LST and in contrast with the disturbances profiles for the clean configuration featuring taller DREs of 200 μm height. This is a further indication that the vortices formed near the DREs in the scenario of the taller DREs condition the flow in such a way that the development of the stationary CFVs cannot be predicted by linear stability theory, considering the assumption of small perturbations does not apply here.

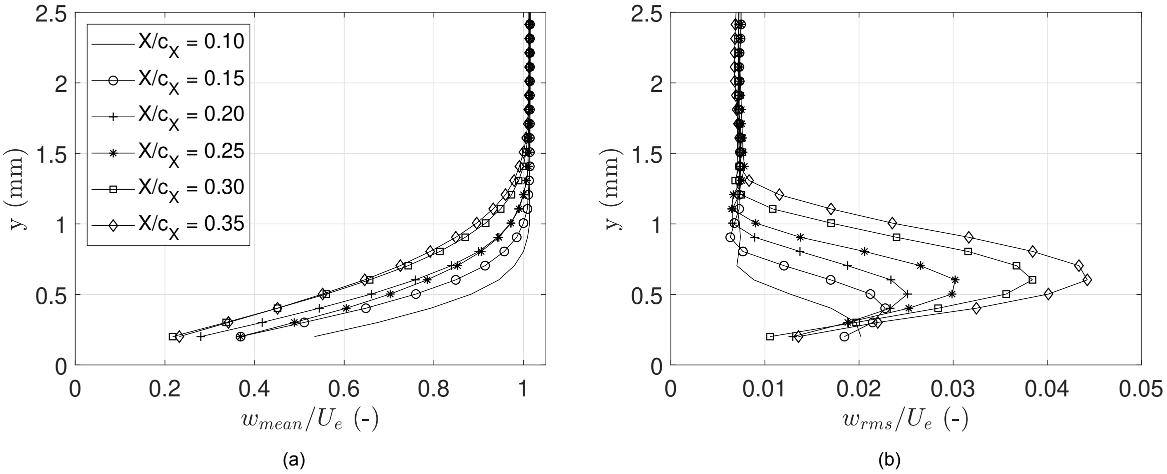

(a)

(b)

Figure 5.45: Span-wise averaged velocity w_{mean} (a) and standard deviation w_{rms} (b) normalised with the local external velocity U_e for several chord locations in case of the clean configuration.

For the sake of brevity, the results indicating the performance of the AC-DBD plasma actuator are not presented here, as the general trend is in agreement with the earlier presented observations. Outliers not considered, the actuation of the AC-DBD plasma actuator results in a reduction in the disturbance profiles and amplitudes as a function of the voltage and frequency.

Effect of Number of AC-DBD Plasma Actuators

The last configuration that has been tested during the experiment and that will be discussed here is the configuration of three consecutive actuators. Although the power consumption is nearly threefold, as presented in section 5.1, the area over which the AC-DBD actuators operate is significantly larger.

Ideally this yields a larger region over which the cross-flow component is reduced, hindering the growth of the primary cross-flow instability for a longer chord-wise duration. Nevertheless, as the streamlines over the swept wing are nearly parallel to the free-stream at more downstream chord locations, and thus the cross-flow component is in the direction perpendicular to the free-stream, the actuators become less effective as they are oriented parallel to the leading edge.

For convenience, the mean total velocity contours pertaining to the clean configuration is again visualised in figure 5.46.

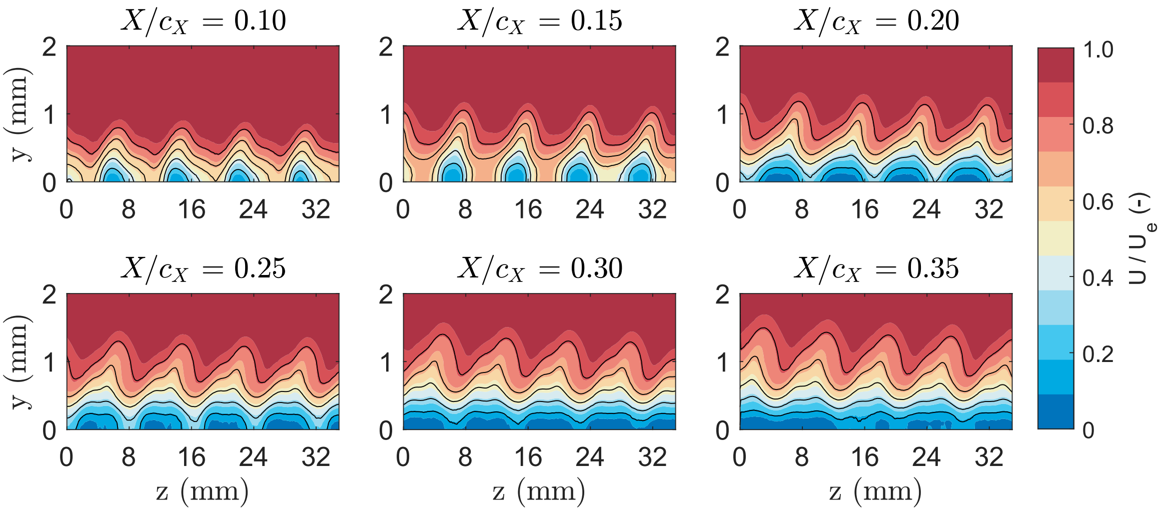

Figure 5.46: Mean total velocity U contours for the clean configuration (plasma inactive, DRE spacing 8 mm, 200 μm tall) at various chord locations. The velocity fields are presented from downstream.

The velocity contours show a strong similarity with figure 5.34, indicating a good repeatability even after replacing the AC-DBD plasma actuator on the model. From the cross-flow amplitude metrics, a consistent trend is observed where initially the amplitude increases and starts to decrease beyond x/c = 0.15, similarly to what has been previously observed.

When the AC-DBD plasma actuator is operated at an applied voltage of 8 kV_{pp} and a carrier frequency of 5 kHz, the effect on the cross-flow instability is insignificant. This is to be expected considering the low power consumption and low induced velocity as concluded from the electrical and mechanical characterisation. Increasing the applied voltage to 10 kV_{pp} yields disturbance profiles featuring slightly lower amplitudes, in agreement with the previous observations for a single AC-DBD plasma actuator. Further increasing the applied voltage to 12 kV_{pp} leads to an interesting scenario, as also observed from the infra-red images. The difference in flow field for the case of an applied voltage of 12 kV_{pp} and a carrier frequency of 5 kHz with respect to the clean configuration is visualised in figure 5.47.

At the first chord station, x/c = 0.10, a slight shift in position of the structures is visible. As the array of three consecutive electrode pairs range from approximately 6% of the chord to 17%, the largest effect is visible in this region. Seemingly, up to x/c = 0.20, the shape of the cross-flow vortices has changed as the peaks of the vortices reach higher and the valleys in between the peaks are wider in comparison with the clean configuration shown in figure 5.46. Nevertheless, the forced mode remains visible as the vortices are spaced 8 mm apart. Beyond the chord location of x/c = 0.20, the vortices develop rapidly as the valleys become less deep and ultimately much of the initial structure has disappeared at x/c = 0.35, judging from the black contour lines.

The mean span-wise standard deviation w_{rms} for the case where the AC-DBD plasma actuator is active (12 kV_{pp}, 5 kHz) is shown in figure 5.48 for the various chord locations. It is clear that, when comparing to figure 5.36, the standard deviation is rather high near the wall and the cross-flow vortices feature higher velocity gradients. As three AC-DBD plasma actuators are present that each introduce

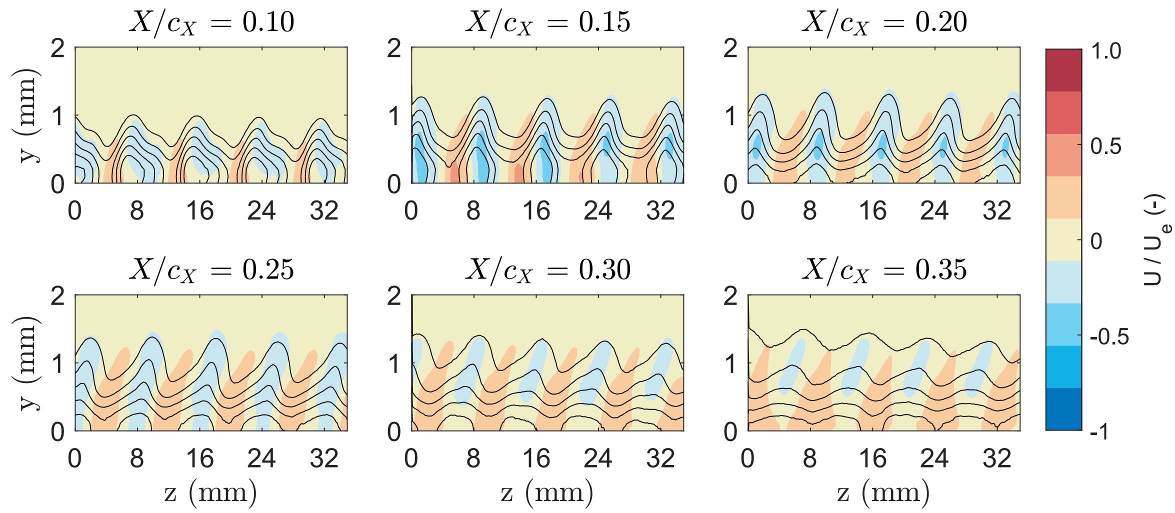

Figure 5.47: Total velocity U contours normalised with the mean local external velocity U_e (12 kV_{pp}, 5 kHz). The clean configuration is subtracted to show the difference. The mean velocity is visualised by the black iso-lines (5 levels from 0 to 1). The contours are presented from downstream.

(unsteady) disturbances, it is expected that the standard deviation is higher near the wall, particularly in between the vortices. Beyond the chord location of x/c = 0.20, which is the first chord station past the plasma actuator array, the velocity gradients are rather strong. The vortices lose their distinct shape and structure and break down shortly after.

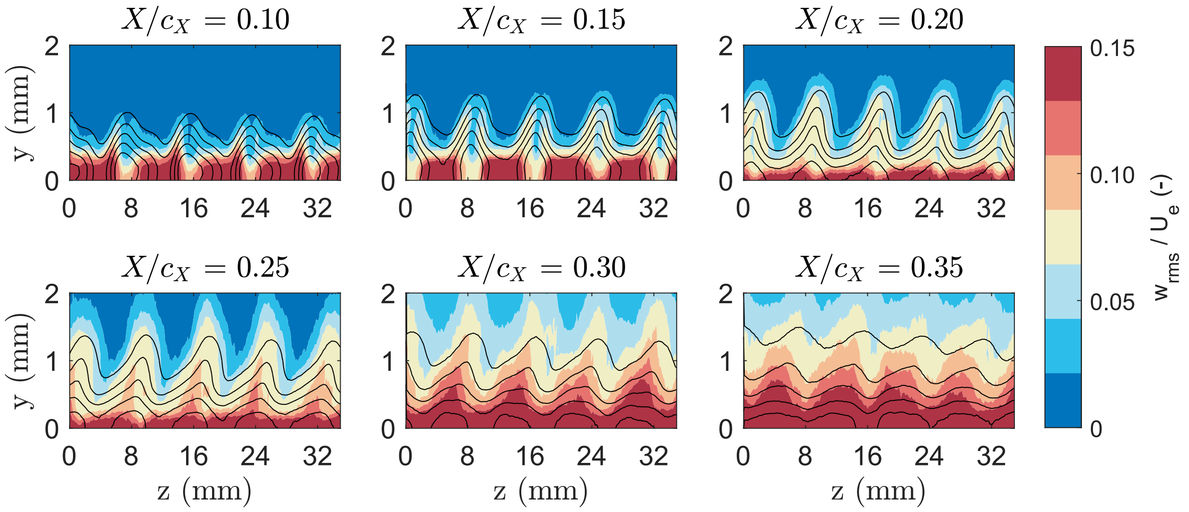

Figure 5.48: Mean span-wise standard deviation w_{rms} contours in the case of plasma active (3 actuators, 12 kV_{pp}, 5 kHz) at various chord locations. The velocity fields are presented from downstream.

The associated disturbance profiles for the clean configuration and the case where the plasma actuator is active are shown in figure 5.49. In agreement with figure 5.47, the disturbance profile pertaining to the active AC-DBD plasma actuator is similar to the clean configuration, although the boundary layer thickness as well as the maximum amplitude are slightly larger up to x/c = 0.15. The first significant change is visible from x/c = 0.20, as the w_{rms} profile corresponding to the active actuator is significantly different to that of the clean configuration. There is no distinct secondary maximum and the profile is fuller. It is clear that the cross-flow vortices no longer develop according to the linear stability theory beyond this chord station, as the velocity gradients close to the wall increase and the structures break down.

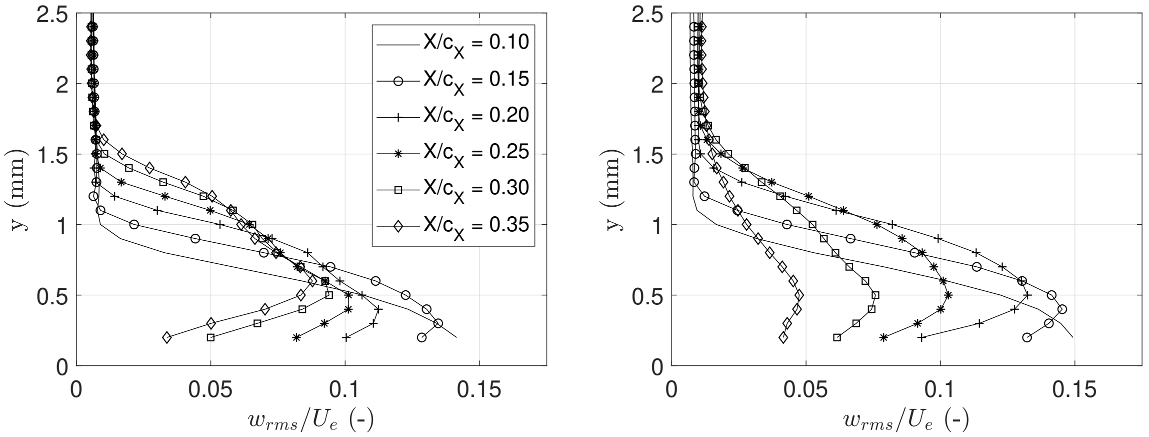

(a)

(b)

Figure 5.49: Span-wise averaged standard deviation w_{rms} for the clean configuration (a) and for the case where the three AC-DBD plasma actuators are active (12 kV_{pp}, 5 kHz), non-dimensionalised with the local external velocity U_e for several chord locations.

It can be concluded that, as expected, there is an upper limit in terms of cross-flow instability control through base-flow modification using AC-DBD plasma actuators. Whereas no early transition was observed for even the largest combination of voltage and frequency for a single AC-DBD plasma actuator, early transition occurred for three consecutive actuators at an applied voltage of 12 kV_{pp}. Further investigation is required to determine the exact cause for this early transition, although several possible explanations have already been proposed.

6

Conclusion & Recommendations

With the aviation industry being one of the fastest growing sources of greenhouse gas emissions, there is an urgency for a more sustainable aviation sector. One avenue that could lead to a significant reduction in skin friction drag and consequently fuel consumption (and cost) is that of laminar-to-turbulent boundary layer transition delay. As concluded from a review on the current state of the art, the dominating mechanism that is responsible for transition over swept wings, which are prevalent on modern aircraft, is the cross-flow instability. In this research, a flow control device in the form of an AC-DBD plasma actuator was employed to assess to possibility of controlling or suppressing this cross-flow instability as present on a swept wing through base-flow modification.

The plasma actuator has seen a rise of interest due to its capability of directional control, the relatively low power consumption and the fact it contains no moving parts. Experimental proof of cross-flow instability control by base-flow modification through plasma actuators was first presented by Yadala et al. [95] in 2018. Although this study has shown that plasma-based base-flow modification can lead to a delay in laminar-to-turbulent transition, the physical mechanism is responsible has not yet been experimentally investigated. It is for this reason that the following research objective was formulated:

To assess how an AC-DBD plasma actuator, with the objective of base-flow modification, affects the cross-flow instability in relation to cross-flow induced transition over a swept wing.

An electrical and mechanical characterisation were performed for various AC-DBD plasma actuator configurations to assess their power consumption and performance. In agreement with the results presented by, amongst others, Corke et al. [11], increasing the voltage resulted in an increase in power consumption according to a power law with a coefficient in between 5/2 and 7/2. It was found that increasing the number of consecutive plasma actuators and decreasing the spacing between these electrodes resulted in a higher power consumption. Furthermore, reducing the dielectric thickness led to a higher power consumption for the same operating condition in comparison with thicker dielectric sheets. Through time-resolved 2D2C-PIV measurements in quiescent conditions, it was observed that increasing the voltage and frequency led to higher induced velocities and body forces, although a stronger response was observed from increasing the voltage. A spectral analysis revealed that most of the power of the signal is distributed over the fundamental frequency and its harmonics. Nevertheless, strong velocity fluctuations were also observed in the lower frequency band, which is in agreement with the observations by Yadala et al. [95] and Serpieri [84]. These lower frequency fluctuations have the ability to directly or indirectly trigger travelling cross-flow waves, which are capable of causing early transition.

A wind tunnel experiment was conducted in the anechoic vertical tunnel at the Delft University of Technology to assess the influence of the AC-DBD plasma actuator on the boundary layer in the vicinity of the actuator. A swept wing model specifically designed for cross-flow and receptivity studies was fitted with a single AC-DBD plasma actuator. Stereoscopic PIV was employed to measure all three velocity components simultaneously over the swept wing in the region of the AC-DBD plasma actuator. It was found that the AC-DBD plasma actuator is capable of inducing a velocity jet against the incoming flow, such that both tangential and perpendicular velocity component along a streamline are reduced for a variety of operating conditions. As such, the AC-DBD plasma actuator fulfils its purpose of directly reducing the cross-flow component. Interestingly, an increase in the cross-flow component was observed for the operating conditions of 1 and 2 kHz at an applied voltage of 15 kV_{pp}. As the velocity was reduced from 22 m/s (Re_X = 7.59 $\cdot$ 10^5) up to 16 m/s (Re_X = 5.51 $\cdot$ 10^5), the influence of the actuator on the flow was magnified and thus from this experiment it can be concluded that, as the Reynolds number decreases, the authority of the AC-DBD plasma actuator increases.

A second wind tunnel experiment was conducted in order to assess the influence of the AC-DBD plasma actuator on the development of the primary cross-flow instability. From LST, the most critical wavelength was found to be 8 mm. Discrete roughness elements of various heights and spacings were applied to the leading edge of the wing to force the desired wavelength. Infra-red thermography was employed to support the 2D2C-PIV measurements. From the IR images, a clear modulation of the base flow could be observed in the case where the AC-DBD plasma actuator was inactive and DREs with a height of 200 μm were forcing the critical wavelength. Once the actuator was activated, turbulent wedges appeared in the case of an applied voltage of 15 kV_{pp} and carrier frequencies up to 3 kHz, as a result of local high-intensity plasma discharges. It is believed these arcs are correlated with the aging of the actuator.

Through a spatial Fourier analysis on the 2D2C-PIV mean velocity fields, it was found that the stationary cross-flow vortices were spaced 8 mm apart, confirming the ability of the DREs to force this wavelength. Surprisingly, the maximum amplitude and wall-normal integral as computed from the mode shape profiles showed a decrease in the stream-wise direction, in contrast with predictions from LST. This reduction in amplitude was not found in the case of 100 μm DREs, indicating that certainly the taller DREs are directly responsible for the decrease in stationary CFV amplitude as a function of the chord location. Although the observed development of the disturbance profiles is in line with the observations by Downs et al. [15] regarding transient growth, it is unclear whether this mechanism is occurring or whether or factors are responsible for the observed behaviour. Nevertheless, it is found that the actuation of the AC-DBD plasma actuator results in a decrease of the cross-flow vortex amplitudes for various cases. In agreement with the obtained IR images, lower carrier frequencies up to 3 or 4 kHz resulted in the formation of turbulent wedges. Due to the dampening of the structures, low CFV amplitudes were obtained. Instead, operating the actuator at a voltage of 15 kV_{pp} and a higher carrier frequency of 5 kHz yielded a slight reduction in cross-flow amplitude at each chord location. Interestingly, the CFVs also shifted location, which is believed to be a direct consequence of the reduction in the cross-flow component. Employing three consecutive actuators yielded a similar result for an applied voltage of 8 and 10 kV_{pp}, whereas further increasing the voltage to 12 kV_{pp} led to early transition.

Although the presented results provide an adequate overview of the influence of the AC-DBD plasma actuator on the cross-flow instability, several uncertainties have appeared throughout the research. First of all, an increase in the cross-flow component was observed when the actuator was operated at a carrier frequency of 1 and 2 kHz. A repeat of the experiment could provide an answer to whether this result is physical. Secondly, the observed development for the stationary cross-flow vortices induced by 200 μm tall discrete roughness elements was in contrast with the growth as predicted from LST. It is thought that this discrepancy is a direct result of the height of the elements, so it is recommended that future experiments preferably employ roughness elements of slightly lower amplitude. Lastly, three consecutive actuators were seen to cause early transition on the swept wing when operated at 12 kV_{pp}. Although several possible explanations have been presented, it is unsure which mechanism, if any, is dominating.

To further understand the influence of the AC-DBD plasma actuator on the cross-flow instability within the scope of the performed experiments, other theoretical and numerical models should be consulted. The altered boundary layer velocity profiles caused by the AC-DBD actuator can be used as an input for the Orr-Sommerfeld equation to evaluate the change in stability characteristics. By directly using the obtained body force field from the mechanical characterisation as an input for numerical/CFD models, the observations in the wind tunnel can be compared to these simulations, although it must be noted that the unsteady component of the actuator should be taken into account. Further sensitivity studies involving the AC-DBD plasma actuator location and geometry can then be performed in a relatively straight forward manner, for which the results can be validated in the wind tunnel.

To assess whether the used geometric configurations as well as carrier frequency and voltage combinations yield a transition delay, a similar configuration can be placed on the 66018-M3J wing. Although this would be similar to the experiment performed by Yadala et al. [95], these experiments at a higher Reynolds number and on a larger scale involving planar PIV or stereoscopic PIV wherever possible should provide further insight in the base-flow modification capability of AC-DBD plasma actuators and how the cross-flow vortices are affected further downstream. During this research, the aging and degradation of the AC-DBD plasma actuator due to the high applied voltage and frequency proved to be a hindrance in several occasions. Ideally, a thicker dielectric material is employed to limit the degradation of the actuator. If a thicker dielectric is used such that the lifetime of the actuator is significantly high, hot wire anemometry can be employed to track the development of the stationary cross-flow vortices as well as the spectral content. The cases where the actuator is active can then be compared to case where the actuator is inactive to assess the effect of the actuator on the frequency spectrum and the velocity gradients pertaining to the three typical modes. Ideally, this extends the knowledge on the influence of the AC-DBD plasma actuator on the cross-flow instability.

Bibliography

[1] A. C. Aba'a Ndong, N. Zouzou, N. Benard, and E. Moreau. Effect of dielectric aging on the behavior of a surface nanosecond pulsed dielectric barrier discharge. *IEEE Transactions on Dielectrics and Electrical Insulation*, 20(5):1554–1560, 2013.

[2] G. Alonso, A. Benito, L. Lonza, and M. Kousoulidou. Investigations on the distribution of air transport traffic and CO2 emissions within the European Union. *Journal of Air Transport Management*, 36:85–93, 2014.

[3] D. E. Ashpis, M. C. Laun, and E. L. Griebeler. Progress toward accurate measurements of Dielectric Barrier Discharge Plasma Actuator Power. *AIAA Journal*, 55(7):1–15, 2017.

[4] P. G. Baines, S. J. Majumdar, and H. Mitsuderait. The mechanics of the Tollmien-Schlichting wave. *J. Fluid Mech.*, 312:107–124, 1996.

[5] N. Benard and E. Moreau. Electrical and mechanical characteristics of surface AC dielectric barrier discharge plasma actuators applied to airflow control. *Exp. Fluids*, 55:1–43, 2014.

[6] N. Benard, A. Debien, and E. Moreau. Time-dependent volume force produced by a non-thermal plasma actuator from experimental velocity field. *Journal of Physics D: Applied Physics*, 46(24), 2013.

[7] H. Bippes. Instability Features Appearing on Swept Wing Configurations. *Laminar-Turbulent Transition Book*, pages 419–430, 1990.

[8] H. Bippes. Basic experiments on transition in three-dimensional boundary layers dominated by crossflow instability. *Progress in Aerospace Sciences*, 35:363–412, 1999.

[9] H. Bippes, M. Wiegel, and F. Bertolotti. Experiments on the Control of Crossflow Instability with the Aid of Suction Through Perforated Walls. *IUTAM Symp. Mech. of Passive and Active Flow Control*, 53:165–170, 1999.

[10] V. G. Chernoray, A. V. Dovgal, V. V. Kozlov, and L. Löfdahl. Experiments on secondary instability of streamwise vortices in a swept-wing boundary layer. *J. Fluid Mech.*, 534:295–325, 2005.

[11] T. C. Corke, C. L. Enloe, and S. P. Wilkinson. Dielectric barrier discharge plasma actuators for flow control. *Annu. Rev. of Fluid Mech.*, 42:505–529, 2010.

[12] H. Deyhle and H. Bippes. Disturbance growth in an unstable three-dimensional boundary layer and its dependence on environmental conditions. *J. Fluid Mech.*, 316:73–113, 1996.

[13] H. Do, W. Kim, M. A. Capelli, and M. G. Mungal. Cross-talk in multiple dielectric barrier discharge actuators. *Appl. Phys. Lett.*, 92, 2008.

[14] R. S. Downs and E. B. White. Free-stream turbulence and the development of cross-flow disturbances. *J. Fluid Mech.*, 735:347–380, 2013.

[15] R. S. Downs, E. B. White, and N. A. Denissen. Transient Growth and Transition Induced by Random Distributed Roughness. *AIAA Journal*, 46(2), 2008.

[16] P. C. Dörr and M. J. Kloker. Stabilisation of a three-dimensional boundary layer by base-flow manipulation using plasma actuators. *Journal of Physics D: Applied Physics*, 48, 2015.

[17] P. C. Dörr and M. J. Kloker. Transition Control in a Three-dimensional Boundary-layer Flow Using Plasma Actuators. *Procedia IUTAM*, 14:469–478, 2015.

[18] P. C. Dörr and M. J. Kloker. Crossflow transition control by upstream flow deformation using plasma actuators. *Journal of Applied Physics*, 121(6), 2017.

[19] C. L. Enloe, T. E. McLaughlin, R. D. VanDyken, K. D. Kachner, E. J. Jumper, T. C. Corke, M. Post, and O. Haddad. Mechanisms and Responses of a Single Dielectric Barrier Plasma Actuator: Geometric Effects. *AIAA Journal*, 42(3):595–604, 2004.

[20] R. Erfani, H. Zare-Behtash, C. Hale, and K. Kontis. Development of DBD plasma actuators: The double encapsulated electrode. *Acta Astronautica*, 109:132–143, 2015.

[21] T. M. Fischer and U. Dallmann. Primary and secondary stability analysis of a three-dimensional boundary-layer flow. *Phys. of Fluids A*, 3(10):2378–2391, 1991.

[22] T. Friederich and M. J. Kloker. Control of the secondary cross-flow instability using localized suction. *J. Fluid Mech.*, 706:470–495, 2012.

[23] P. Hall and M. R. Malik. On the instability of a three-dimensional attachment-line boundary layer: weakly nonlinear theory and a numerical approach. *J. Fluid Mech.*, 163:257–282, 1986.

[24] P. Hall and S. Seddouguiz. On the onset of three-dimensionality and time-dependence in Görtler vortices. *J. Fluid Mech.*, 204:405–420, 1989.

[25] P. Hall, M. R. Malik, and D. I. A. Poll. On the stability of an infinite swept attachment line boundary layer. *Proc. R. Soc. Lond. A*, 395:229–245, 1984.

[26] T. S. Haynes and H. L. Reed. Simulation of swept-wing vortices using nonlinear parabolized stability equations. *J. Fluid Mech.*, 405:325–349, 2000.

[27] K. D. Hinsch. Three-dimensional particle velocimetry. *Measurement Science and Technology*, 6 (6):742–753, 1995.

[28] A. R. Hoskinson, N. Hershkowitz, and D. E. Ashpis. Force measurements of single and double barrier DBD plasma actuators in quiescent air. *Journal of Physics D: Applied Physics*, 41, 2008.

[29] S. M. Hosseini, D. Tempelmann, A. Hanifi, and D. S. Henningson. Stabilization of a swept-wing boundary layer by distributed roughness elements. *J. Fluid Mech.*, 718, 2013.

[30] M. Högberg and D. S. Henningson. Secondary instability of cross-flow vortices in Falkner-Skan-Cooke boundary layers. *J. Fluid Mech.*, 368:339–357, 1998.

[31] E. Janke and P. Balakumar. Theoretical and Computational Fluid Dynamics On the Secondary Instability of Three-Dimensional Boundary Layers. *Theoret. Comput. Fluid Dyn.*, 14:167–194, 2000.

[32] R. D. Joslin. Aircraft Laminar Flow Control. *Annu. Rev. Fluid Mech.*, 30:1–29, 1998.

[33] T. N. Jukes, K-S Choi, T. Segawa, and H. Yoshida. Jet flow induced by a surface plasma actuator. *Proc. IMechE Part I: Journal of Systems and Control Engineering*, 222(5):347–356, 2008.

[34] Y. S. Kachanov. Physical Mechanisms of Laminar Boundary-Layer Transition. *Annu. Rev. Fluid Mech*, 26:411–82, 1994.

[35] Y. S. Kachanov. Three-dimensional receptivity of boundary layers. *Eur. J. Mech. B-Fluids*, 19: 723–744, 2000.

[36] M. Kawakami, Y. Kohama, and M. Okutsu. Stability Characteristics of Stationary Crossflow Vortices in Three-Dimensional Boundary Layer. *37th Aerospace Sciences Meeting and Exhibit*, 1998.

[37] W. Koch. On the spatio-temporal stability of primary and secondary crossflow vortices in a three-dimensional boundary layer. *J. Fluid Mech.*, 456:85–111, 2002.

[38] Y. Kohama, W. S. Saric, and J. A. Hoos. A high frequency secondary instability of crossflow vortices that leads to transition. *In Proc. Royal Aero. Soc. Conf. on Boundary-Layer Transition and Control*, 1991.

[39] M. Kotsonis. Diagnostics for characterisation of plasma actuators. *Meas. Sci. Technol.*, 26(9), 2015.

[40] M. Kotsonis, S. Ghaemi, L. Veldhuis, and F. Scarano. Measurement of the body force field of plasma actuators. *J. Phys. D: Applied Physics*, 44(4), 2011.

[41] H. B. E. Kurz and M. J. Kloker. Receptivity of a swept-wing boundary layer to micron-sized discrete roughness elements. *J. Fluid Mech.*, 755:62–82, 2014.

[42] H. B. E. Kurz and M. J. Kloker. Mechanisms of flow tripping by discrete roughness elements in a swept-wing boundary layer. *J. Fluid Mech.*, 796:158–194, 2016.

[43] F. Li and M. R. Malik. Fundamental and subharmonic secondary instabilities of Görtler vortices. *J. Fluid Mech.*, 297:77–100, 1995.

[44] A. V. Likhanskii, M. N. Shneider, S. O. MacHeret, and R. B. Miles. Modeling of dielectric barrier discharge plasma actuator in air. *Journal of Applied Physics*, 103(5), 2008.

[45] Z. Liu, Y. Zheng, L. Jia, J. Jiao, and Q. Zhang. Stereoscopic PIV studies on the swirling flow structure in a gas cyclone. *Chemical Engineering Science*, 61(13):4252 – 4261, 2006.

[46] J. Lohse, H. P. Barth, and W. Nitsche. Active control of crossflow-induced transition by means of in-line pneumatic actuator orifices. *Exp. Fluids*, 57(8), 2016.

[47] L. Léger, E. Moreau, and G. Touchard. Control of Low Velocity Airflow along a Flat Plate with a DC Electrical Discharge. *Industry Applications Conference 2001 IEEE, Thirty-Sixth IAS Annual Meeting*, 3:1536–1543, 2001.

[48] L. M. Mack. Transition prediction and linear stability theory. *AGARD Laminar-Turbulent Transition 22 P*, 1977.

[49] L. M. Mack. Boundary-Layer Linear Stability Theory. *AGARD Report 709*, 1984.

[50] M. R. Malik, F. Li, and C.-L. Chang. Crossflow disturbances in three-dimensional boundary layers: nonlinear development, wave interaction and secondary instability. *J. Fluid Mech.*, 268:1–36, 1994.

[51] M. R. Malik, F. Li, M. M. Choudhari, and C.-L. Chang. Secondary instability of crossflow vortices and swept-wing boundary-layer transition. *J. Fluid Mech.*, 399:85–115, 1999.

[52] R. Messing and M. J. Kloker. Investigation of suction for laminar flow control of three-dimensional boundary layers. *J. Fluid Mech.*, 658:117–147, 2010.

[53] T. Michelis. *Boundary Layer Separation: Diagnostics and Control*. TU Delft, 2017.

[54] V. I. Mistry, G. J. Page, and J. J. McGuirk. Simulation of Receptivity and Induced Transition from Discrete Roughness Elements. *Flow, Turbulence and Combustion*, 95(2-3):301–334, 2015.

[55] M. V. Morkovin, E. Reshotko, and T. Herbert. Transition in open flow systems—a reassessment. *Bull. Am. Phys. Soc.*, 1994.

[56] B. Müller and H. Bippes. Experimental study of instability modes in a three-dimensional boundary layer. *Proc. AGARD Symp. on Fluid Dyn. of Three-Dim. Turb. Shear Flows and Trans.*, 438:1–15, 1988.

[57] K. Peng and M. Kotsonis. Cross-flow instabilities under plasma actuation: Design, commissioning and preliminary results of a new experimental facility. *AIAA Scitech 2021 Forum*, 1194, 2021.

[58] D. I. A. Poll. Some observations of the transition process on the windward face of a long yawed cylinder. *J. Fluid Mech.*, 150:32–356, 1985.

[59] J. Pons, E. Moreau, and G. Touchard. Asymmetric surface dielectric barrier discharge in air at atmospheric pressure: Electrical properties and induced airflow characteristics. *Journal of Physics D: Applied Physics*, 38(19):3635–3642, 2005.

[60] L. Prandtl. über Flüssigkeitsbewegung bei sehr kleiner Reibung. *Verhandl □, Intern. Math. Kongr. Heidelberg*, 2:484–491, 1904.

[61] R. H. Radeztsky, M. S. Reibert, and W. S. Saric. Effect of isolated micron-sized roughness on transition in swept-wing flows. *AIAA Journal*, 37(11):1370–1377, 1999.

[62] M. Raffel, C. E. Willert, F. Scarano, C. J. Kähler, S. T. Wereley, and J. Komperhans. *Particle Image Velocimetry: A Practical Guide*. Springer, 2013.

[63] H. L. Reed and W. S. Saric. Stability of Three-Dimensional Boundary Layers. *Ann. Rev. Fluid Mech.*, 21:235–84, 1989.

[64] M. S. Reibert, W. S. Saric, R. B. Carrillo, and K. L. Chapman. Experiments in nonlinear saturation of stationary crossflow vortices in a swept-wing boundary layer. *34th Aerospace Sciences Meeting and Exhibit*, 1996.

[65] D. P. Rizzetta and M. R. Visbal. Plasma-based control of excrescence-generated transition on a swept wing. *8th AIAA Flow Control Conference*, 2016.

[66] D. V. Roupassov, A. A. Nikipelov, M. M. Nudnova, and A. Y. Starikovskii. Flow separation control by plasma actuator with nanosecond pulse periodic discharge. *46th AIAA Aerospace Sciences Meeting and Exhibit*, 2008.

[67] D. V. Roupassov, A. A. Nikipelov, M. M. Nudnova, and A. Y. Starikovskii. Role of the electric waveform supplying a dielectric barrier discharge plasma actuator. *Applied Physics Letters*, 100 (19), 2012.

[68] W. S. Saric. Görtler Vortices. *Annu. Rev. Fluid Mech.*, 26:379–409, 1994.

[69] W. S. Saric and H. L. Reed. Supersonic Laminar Flow Control on Swept Wings Using Distributed Roughness. *40th AIAA Aerospace Sciences Meeting & Exhibit*, 2002.

[70] W. S. Saric, R. B. Carrillo, and M. S. Reibert. Leading-Edge Roughness as a Transition Control Mechanism. *36th AIAA Aerospace Sciences Meeting and Exhibit*, 1998.

[71] W. S. Saric, H. L. Reed, and E. J. Kerschen. Boundary-layer Receptivity to Freestream Disturbances. *Annu. Rev. Fluid Mech.*, 34:291–319, 2002.

[72] W. S. Saric, H. L. Reed, and E. B. White. Stability and transition of three-dimensional boundary layers. *Annu. Rev. Fluid Mech.*, 35:413–440, 2003.

[73] F. Scarano. Iterative image deformation methods in PIV. *Measurement Science and Technology*, 13(1), 2002.

[74] H. Schlichting and K. Gersten. *Boundary-Layer Theory*. Springer, 2016.

[75] L. U. Schrader, L. Brandt, and D. S. Henningson. Receptivity mechanisms in three-dimensional boundary-layer flows. *J. Fluid Mech.*, 618:209–241, 2009.

[76] L. U. Schrader, L. Brandt, and T. A. Zaki. Receptivity, instability and breakdown of Görtler flow. *J. Fluid Mech.*, 682:362–396, 2011.

[77] C. Y. Schuele, T. C. Corke, and E. Matlis. Control of stationary cross-flow modes in a Mach 3.5 boundary layer using patterned passive and active roughness. *J. Fluid Mech.*, 718:5–38, 2013.

[78] A. Sciacchitano. Uncertainty quantification in particle image velocimetry. *Meas. Sci. Technol.*, 30: 1–31, 2019.

[79] A. Sciacchitano and B. Wieneke. Piv uncertainty propagation. *Meas. Sci. Technol.*, 27:1–16, 2016.

[80] J. Serpieri. *Cross-Flow Instability: Flow diagnostics and control of swept wing boundary layers*. TU Delft, 2018.

[81] J. Serpieri and M. Kotsonis. Design of a swept wing wind tunnel model for study of crossflow instability. *AIAA Applied Aerodynamics Conference*, 33, 2015.

[82] J. Serpieri and M. Kotsonis. Three-dimensional organisation of primary and secondary crossflow instability. *J. Fluid Mech.*, 799:200–245, 2016.

[83] J. Serpieri and M. Kotsonis. Conditioning of unsteady cross-flow instability modes using dielectric barrier discharge plasma actuators. *Experimental Thermal and Fluid Science*, 93:305–318, 2018.

[84] J. Serpieri, S. Yadala, and M. Kotsonis. Conditioning of cross-flow instability modes using dielectric barrier discharge plasma actuators. *J. Fluid Mech.*, 833:164–205, 2017.

[85] A. M. O. Smith and N. Gamberoni. Transition, pressure gradient and stability theory. *Technical Report ES-26388, Douglas Aircraft Company*, 1956.

[86] D. Tempelmann, L. U. Schrader, A. Hanifi, L. Brandt, and D. S. Henningson. Swept wing boundary-layer receptivity to localized surface roughness. *J.Fluid Mech.*, 711:516–544, 2012.

[87] F. O. Thomas, T. C. Corke, M. Iqbal, A. Kozlov, and D. Schatzman. Optimization of dielectric barrier discharge plasma actuators for active aerodynamic flow control. *AIAA Journal*, 47(9):2169–2178, 2009.

[88] J. L. Van Ingen. A suggested semi-empirical method for the calculation of the boundary layer transition region. *VTH-74, Delft University of Technology, Delft, The Netherlands*, 1956.

[89] J. L. Van Ingen. The e^N method for transition prediction; Historical review of work at TU Delft. *38th Fluid Dynamics Conference and Exhibit, Seattle, Washington*, 2008.

[90] P. Wassermann and M. J. Kloker. Mechanisms and passive control of crossflow-vortex-induced transition in a three-dimensional boundary layer. *J. Fluid Mech.*, 456:49–84, 2002.

[91] P. D. Welch. The Use of Fast Fourier Transform for the Estimation of Power Spectra: A Method Based on Time Averaging Over Short, Modified Periodograms. *IEEE Transactions on Audio and Electroacoustics*, 15(2), 1967.

[92] E. B. White and W. S. Saric. Application of Variable Leading-Edge Roughness for Transition Control on Swept Wings. *38th Aerospace Sciences Meeting and Exhibit*, 2000.

[93] E. B. White and W. S. Saric. Secondary instability of crossflow vortices. *J. Fluid Mech.*, 525: 275–308, 2005.

[94] J. B. Wilke. Aerodynamic flow-control with dielectric barrier discharge plasma actuators. *DLR e.V. - Forschungsberichte*, 19, 2009.

[95] S. Yadala, M. T. Hehner, J. Serpieri, N. Benard, P. C. Dörr, M. J. Kloker, and M. Kotsonis. Experimental control of swept-wing transition through base-flow modification by plasma actuators. *J. Fluid Mech.*, 844:R2 1–11, 2018.

[96] S. Yadala, M. T. Hehner, J. Serpieri, N. Benard, and M. Kotsonis. Swept-wing transition control using DBD plasma actuators. *2018 Flow Control Conference*, 2018.